Metal-Organic Frameworks by Molecular Layer Deposition

Kristian Blindheim Lausund

Dissertation for the degree of Philosophiae Doctor

Department of Chemistry
Faculty of Mathematics and Natural Sciences
University of Oslo

2018

Series of dissertations submitted to the
Faculty of Mathematics and Natural Sciences, University of Oslo
No. 2082

ISSN 1501-7710

Cover: Hanne Baadsgaard Utigard.
Print production: Reprosentralen, University of Oslo.

Preface

This thesis is submitted in partial fulfilment of the requirements for the degree of Philosophiae Doctor at the Department of Chemistry, Faculty of Mathematics and Natural Sciences, University of Oslo. The work was carried out at the research group for Nanostructures and Functional Materials (NAFUMA) in the period between August 2014 and October 2018, and is a part of the strategic research initiative Diatech@UiO.

First, I would like to express my most sincere gratitude to my supervisors. In particular my main supervisor Professor Ola Nilsen who, through his patient guidance and generous support and encouragement, has taught me so much. My other supervisors Professor Elsa Lundanes, Professor Carl Henrik Gørbitz, and Associate Professor Steven Wilson also have my sincere gratitude for their encouragement, support and genuine interest in my work. I sincerely doubt that any PhD student could be more satisfied with, or impressed by his or her team of supervisors.

I would also like to thank my colleagues in NAFUMA and the rest of the Department of Chemistry for their scientific and technical support. Special thanks go to Leva Momtazi for FTIR work; Øystein Slagtern Fjellvåg for GIXRD and XRR support; Veljko Petrovic for his bachelor thesis work, which is included in **Paper II**; Per-Anders Hansen for help with spectroscopic ellipsometry and the photo luminescence measurements for **Paper III**; and Malin Solheim Olsen for tests of antibacterial effects for **Paper III**.

To my colleagues in Diatech@UiO, I would also like to say thank you for our interesting discussions and for teaching me about your respective fields. This unique environment, which brings together scientists from pharmacy, physics and various branches of chemistry, has become a valuable forum where asking the “stupid questions” and learning from each other is encouraged, something I really appreciate.

My colleagues in NAFUMA, Diatech@UiO and the rest of the Department of Chemistry also deserve thanks for creating a nice working environment throughout these four years. Although there are many who deserve my gratitude, a special thank-you goes to my office mate Oleksii Ivashenko for his friendship and frequent reminders of Wednesday waffles.

I would also like to thank all of my friends. Most of all for your friendship, but also for pretending to be interested in my field of research. A Thursday evening with some of you at Skedsmokorset, or a spontaneous hangout event, can really transform my day or even my week, and is much appreciated.

Finally, I would like to thank my parents and the rest of my family for your love and support. I am proud to have such a wonderful family as you, and I am grateful for every one of you and everything you have done for me. Thank you!

Abstract

Organic-inorganic hybrid materials have been prepared as thin films by molecular layer deposition (MLD) for over a decade. However, it has proven challenging to synthesize porous films or crystalline metal-organic frameworks (MOFs) through this technique, and only a few examples of such synthesis exist in the literature. MOF thin films are desirable for a large range of applications spanning from sensor materials to separation techniques or even drug delivery, but so far, they have required solvent-based synthesis such as solvothermal synthesis. Using an all-gas-phase approach, however, opens for easier implementation in applications such as microelectronics with delicate parts that are not compatible with solvothermal synthesis.

In this work, a new synthesis method for MOF thin films, including the exceptionally stable structure UiO-66 and a few related Zr-based structures, is presented. These structures have been formed by depositing organic-inorganic hybrid films by MLD using $ZrCl_4$ as a precursor along with five different organic precursors. These organic precursors consist of various aromatic structures with two carboxylic acid groups, one in either end of the molecule. The films were subsequently crystallized to form the various MOF structures by heat treatment in acetic acid vapor. The developed technique is the first solvent-free synthesis method of thin films of these Zr-based MOF structures and should open for future applications of such materials where the extraordinary porosity of MOFs is utilized.

During the MLD synthesis, a modulation step was included by adding an acetic acid pulse after the organic precursors. Characterizations of the films by techniques such as FTIR[a], XRD[b] and SEM[c], show that this acetic acid modulation guides the organic precursors in forming a stronger, bidentate coordination to the metal atoms. This is one of the main findings in this thesis since it can provide a better understanding of the reaction kinetics in formation of such films and be applied for control of stoichiometry during growth.

The films were amorphous as-deposited, while still being porous. Such porosity for amorphous films is not common and makes these hybrid films interesting candidates for sensor materials or membranes, particularly for applications where pinhole-free films are required. Preliminary tests show luminescent and antibacterial properties, forming a basis for future research and development.

This thesis is mostly based the work included in three papers, one article on synthesis of UiO-66 thin films (**Paper I**), one article on synthesis of UiO-66-NH_2 (**Paper II**), and a manuscript describing synthesis of films with two larger organic molecules (**Paper III**).

---

[a] Fourier transform infrared spectroscopy
[b] X-ray diffraction
[c] Scanning electron microscopy

List of papers

Paper I:

All-gas-phase synthesis of UiO-66 through modulated atomic layer deposition

K. B. Lausund and O. Nilsen, *Nature Communications*, 2016, **7**, 13578.

Paper II:

All-gas-phase synthesis of amino-functionalized UiO-66 thin films

K. B. Lausund, V. Petrovic and O. Nilsen, *Dalton Transactions*, 2017, **46**, 16983-16992

Paper III:

MOF thin films with bi-aromatic linkers by molecular layer deposition

K. B. Lausund, M. S. Olsen, P.-A. Hansen, H. Valen, O. Nilsen, submitted manuscript.

Glossary

1,3,5-BTC	-	1,3,5-Benzenetricarboxylate
1,4-BDC	-	1,4-Benzenedicarboxylate
2-amino-1,4-BDC	-	2-Amino-1,4-benzenedicarboxylate
AFM	-	Atomic force microscopy
ALD	-	Atomic layer deposition
BP-4,4’-DC	-	Biphenyl-4,4’-dicarboxylate
BPy-5,5’-DC	-	Bipyridine-5,5’-dicarbocylate
CFU	-	Colony forming units
CVD	-	Chemical vapor deposition
DEZ	-	Diethylzinc ($Zn(C_2H_5)_2$)
DMF	-	Dimethylformamide
DUT	-	Dresden University of Technology
EDX	-	Energy dispersive X-ray spectroscopy
EP	-	Ellipsometric porosimetry
FTIR	-	Fourier transform infrared spectroscopy
HKUST	-	Hong Kong University of Science and Technology
IRMOF	-	Isoreticular metal-organic framework
MEMS	-	Microelectromechanical systems
MIL	-	Matérial Institut Lavoisier
MLD	-	Molecular layer deposition
MOF	-	Metal-organic framework
MOSFET	-	Metal-oxide-semiconductor field-effect transistor
PET	-	Poly ethylene terephthalate
QCM	-	Quartz crystal microbalance
SAM	-	Self-assembled monolayer
SE	-	Spectroscopic ellipsometry
SEM	-	Scanning electron microscopy

TGA	-	Thermogravimetric analysis
thd	-	2,2,6,6-Tetramethyl-3,5-heptanedione
TMA	-	Trimethylaluminum ($Al(CH_3)_3$)
TTIP	-	Titanium tetraisopropoxide ($Ti(OCH(CH_3)_2)_4$)
UiO	-	Universitetet i Oslo / University of Oslo
XRD	-	X-ray diffraction
XRF	-	X-ray fluorescence
XRR	-	X-ray reflectivity
ZIF	-	Zeolitic imidazolate framework

Table of contents

1. Introduction

Materials technology shapes and forms almost every aspect of our daily lives. Materials are now designed with a specific shape, structure or property in mind, forming the technologies that we depend upon. From the small bits and pieces in our cell phone batteries and anti-reflective thin film coatings on glasses or camera lenses; up to bridges, buildings and other infrastructure that connect our world. It would be impossible to achieve such functionalities without research into materials properties. Even the medical technologies that daily save lives in our hospitals would be far behind its present state if materials scientists did not develop antibacterial surface coatings, shape memory alloys, bioactive materials, membranes for separations, *et cetera*. If we attempt to look into future technological solutions to today's problems, we can see that at least half of the 17 sustainable development goals presented by the United Nations in 2015[1] would benefit strongly from further development within materials science. Two examples are "Goal 6: Clean water and sanitation" and "Goal 7: Affordable and clean energy". It is hard to imagine how they can be reached without materials technology solutions.

Within the field of materials technology, the goal is to tailor-design materials with a very particular set of properties suitable for applications. This is often approached by the aid of nanotechnology, either to tune the properties or through new types of synthesis methods. The desired properties depend on the application, and span over electrical properties such as conductivity, magnetic properties, mechanical properties, nanostructured features and many others.

The desired materials properties in this thesis include well-defined pore sizes in the low nanometer to angstrom range, incorporated into a thin-film structure. Such thin-films should then be possible to deposit onto surfaces or a porous supports so as to create porous membranes that could be used for separations of blood sample components inside capillary tubes. Smaller solvent molecules such as water would pass through the pores whereas larger biomolecules like peptides, proteins, or other potential disease biomarkers would be retained. In this manner, the concentration of the biomolecules would be increased in a controlled way, hopefully to the point where they would crystallize into one or a few specimens suitable for investigation by X-ray diffraction (XRD). This methodology would reduce the amount of material required for structure determination by at least two orders of magnitude (to ~10 ng) and allow identification of biomolecules present in very low concentrations in a blood sample. There is consequently a potential to obtain better, more precise and more useful information about the health status of the patient.

In addition to the suggested application above, there are several other potential uses for microporous thin-films. Applications that require separation, for instance desalination of seawater[2], are perhaps the most obvious candidates, but the microporous films could potentially also be excellent sensor materials due to their large internal surface areas or they could be used as low-κ dielectrics.[3]

The desired pore size in the nanometer range is already present in a class of materials known as metal-organic frameworks (MOFs). MOFs are made from inorganic nodes bound to each other by organic molecules referred to as linkers, forming a crystal structure where the pores are a part of the structure. This makes the pore size very well-defined, and makes these materials suitable for a number of applications.

Since MOFs combine organic and inorganic chemistry, they also have interesting properties that are not directly linked to their porosity, such as luminescence[4] and antibacterial effects[5]. This opens for exploration of even more applications. Most current synthesis methods for MOFs yield powders that in themselves could be very useful, however, it has been suggested[3] that several other applications can be realized if thin-films are formed. MOFs will be further described in chapter 2.

1.2 Aim of Study

Due in part to the traditional synthesis paths for MOFs where powders are formed, it is difficult to utilize their full potential. Our aim was therefore to expand the possibilities of formation of MOF materials to also include thin film deposition by all-gas-phase techniques. Our focus has been on synthesis of the relatively complex and exceptionally stable MOF structure known as UiO-66 (UiO = Universitetet i Oslo), and its related structures. A few examples exist in the literature of thin film synthesis of MOFs, and these will be discussed further in chapters 2.2.4 and 3.1. However, very few of these examples show film synthesis through gas-phase techniques, and none of the gas-phase techniques have been used to make the complex MOF structures that we have focused on.

In our group, the method of choice for thin film synthesis is atomic layer deposition (ALD), combined in recent years with molecular layer deposition (MLD). These techniques have a number of advantages over other thin film techniques such as extraordinary thickness control and the ability to coat three-dimensional substrates evenly. ALD and MLD will be described further in chapter 3.

Thin films of MOF materials synthesized by MLD have the potential to realize many of the applications mentioned above. The overall aim of this study was therefore to enable MLD synthesis of thin films of UiO-66 and related structures, and to investigate some possible applications for these films such as membranes for separation, sensor materials, and antibacterial coatings.

2. Metal-Organic Frameworks

Metal-organic frameworks (MOFs) form a class of porous materials built up by inorganic nodes consisting of either individual metal atoms or a clusters of metal atoms, linked together by organic linker molecules to form a three dimensional network. Due to their incredible porosity, which is higher than that of zeolites, MOFs have a large array of potential applications[6]. Already proven examples include gas storage[7-9], catalysis[6, 10, 11], separation[2, 12], drug delivery[13], handling and destruction of toxins[14, 15], and degradation of chemical warfare agents[16, 17].

MOF synthesis emerged from the field of coordination chemistry, where coordination polymers have been investigated for several decades. MOFs, which are also known as porous coordination polymers, were first synthesized in the beginning of the 1990s[18, 19], albeit the name "MOF" first gained popularity in 1995[20]. In the early days of MOF synthesis, one of the main issues was the stability of the structures, especially with regards to removal of the solvents or guest molecules in the pores of the structure. This problem was overcome in 1999 when Yaghi et al.[21] were able to synthesize MOF-5 with Zn-based clusters linked together by 1,4-benzenedicarboxylate (1,4-BDC). MOF-5 retained its porosity, i.e. underwent no structural collapse, upon complete removal of solvent molecules from the pores. The same year, Chui et al.[22] synthesized a Cu-based MOF with 1,3,5-benzenetricarboxylate (1,3,5-BTC) as the linker molecule. This MOF is known as HKUST-1 (HKUST = Hong Kong University of Science and Technology), and is along with MOF-5 one of the most studied MOF structures.

Over the course of the next two decades up until today, MOF materials have been extensively studied. This has led to the discovery of many interesting structures, including some that are remarkably stable such as MIL-100[23], MIL-101[24], ZIF-8[25], and UiO-66[26], the latter is of particular relevance for this thesis (MIL = Matérial Institut Lavoisier and ZIF = Zeolitic imidazolate framework). UiO-66 was first developed at the University of Oslo, as described in the paper by Cavka et al.[26] in 2008, and formed the basis for the UiO-series of MOFs that have Zr-based clusters and various organic linkers (1,4-BDC for standard UiO-66)[27]. A selection of the MOF structures mentioned above are shown in Figure 1.

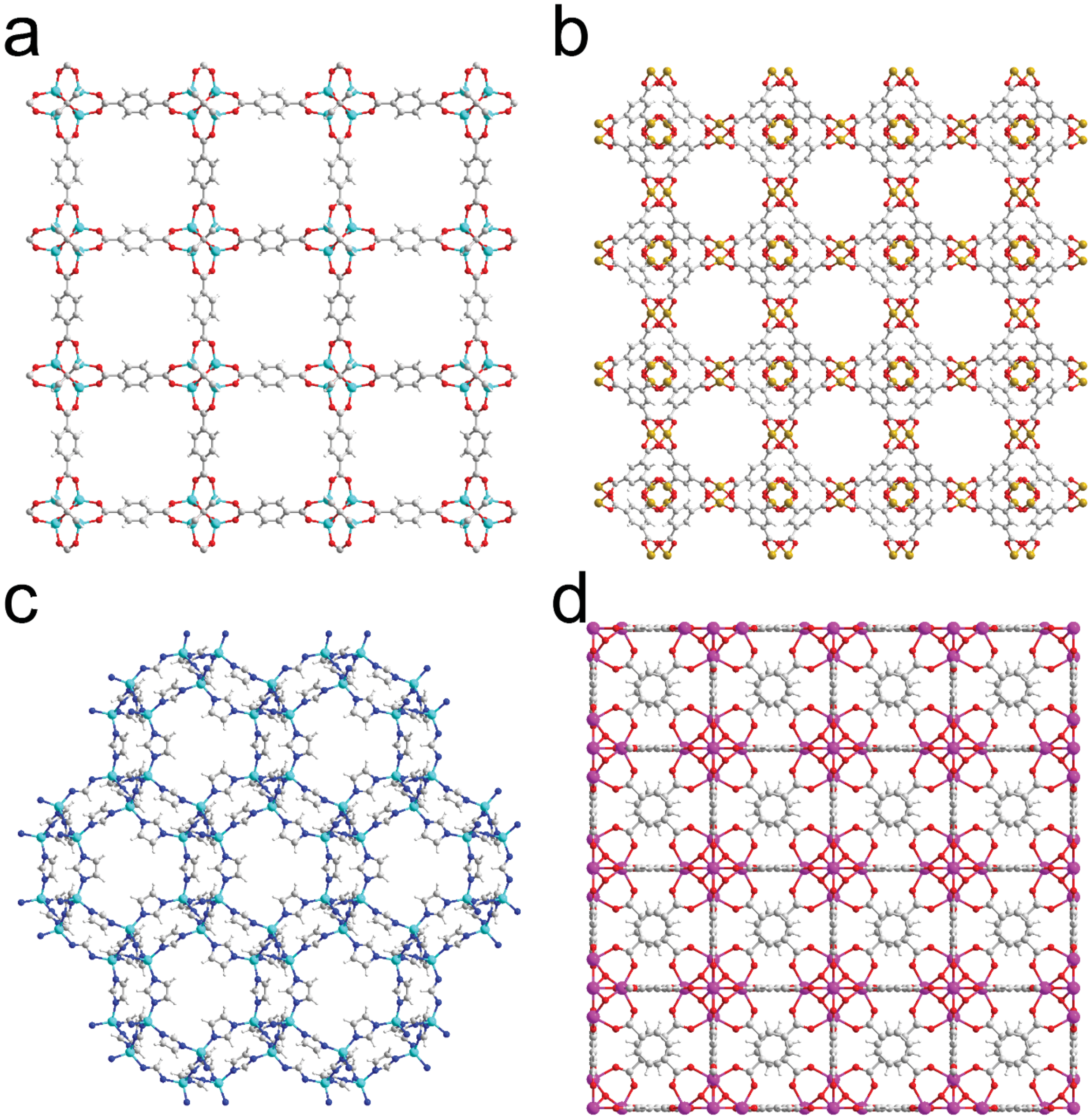

Figure 1: Crystal structures of (a) MOF-5, (b) HKUST-1, (c) ZIF-8, and (d) UiO-66, based on CIF-files from Lock et al.[28], Yakovenko et al.[29], Karagiaridi et al.[30], and Øien et al.[31], respectively. MOF-5, HKUST-1, and UiO-66 are all viewed along the [100]-axis, and ZIF-8 is viewed along the [111]-axis. Atom colors: H = white, C = gray, N = blue, O = red, Cu = brown, Zn = turquoise, and Zr = magenta.

2.1 MOF Structures

As mentioned above, an inorganic node can contain one or more metal atoms. One example of a MOF where the nodes are single metal atom is ZIF-8[25], Figure 2 a. This is a Zn-based MOF where every Zn atom is bound to four imidazolate rings, forming a crystalline network with a cubic structure. The complexity of the nodes increases slightly when going to MOF-2[32] and HKUST-1[22], which are Zn- and Cu-based MOFs where the node consist of two metal atoms that are bridged together by four carboxylate ligands forming a paddlewheel structure, Figure 2 b. In the case of MOF-2 the ligands are 1,4-BDC, and as mentioned above, the ligands in HKUST-1 are 1,3,5-BTC.

The node of MOF-5 is a cluster of four Zn atoms that are all tetrahedrally coordinated to oxygen where one oxygen atom is the central atom of the cluster. The remaining three oxygen atoms belong to three carboxylate groups in linkers that are bridging between the current Zn atom and its three neighboring Zn atoms, Figure 2 c. For UiO-66, the cluster forming the inorganic node is even more complex. This cluster consists of six Zr atoms that are all coordinated to eight oxygen atoms, four of which belong to four different carboxylate linkers that bridge between two Zr atoms. The remaining oxygen atoms are found in the cluster itself where they are bridging three of the Zr atoms, Figure 2 d. This is just a small selection of the inorganic clusters that are found in MOF structures. A more extensive overview is given in the review article by Furukawa et al.[33] and its supporting information. The beauty and complexity of some of these clusters is quite impressive, and they are well worth a look.

Even though the wide selection of inorganic nodes in itself gives rise to a substantial number of MOF structures, the variations rendered possible by choosing different linker molecules is even more extraordinary. In fact, the possibility to chemically functionalize the linkers has often been used as an argument for why MOFs could be more tunable for different applications than other microporous materials such as zeolites[21, 22]. By varying the linker molecules, it is possible to change the size and shape of the pores or add catalytic centers in structural cavities[34]. Changing the linkers can also alter other properties of a MOF such as their luminescence[4].

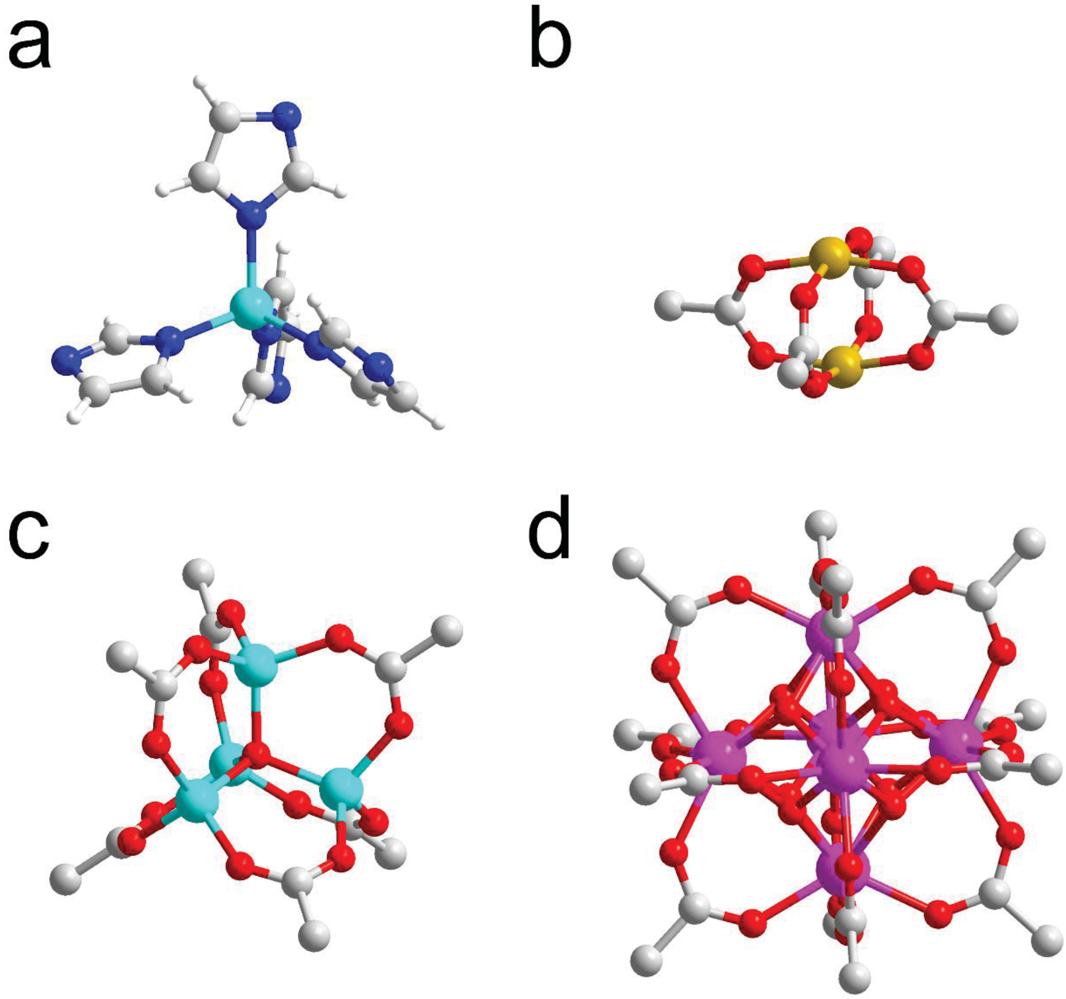

Figure 2: The inorganic nodes of (a) ZIF-8 (with linkers), (b) HKUST-1, (c) MOF-5, and (d) UiO-66, based on the same CIF-files as Figure 1. Atom colors: H = white, C = gray, N = blue, O = red, Cu = brown, Zn = turquoise, and Zr = magenta.

One expression that has been used to describe the formation of MOFs is *reticular synthesis*, where reticular means "having the form of a net". From this, the word "isoreticular" has been defined, meaning "based on the same net"[35]. Isoreticular structures can thus be synthesized by choosing one MOF structure and change the linker to one that fits into the same net. This has led to an extreme number of different MOF structures due to the enormous repertoire of possible linkers. In 2013, Furukawa et al.[33] reported that the number of MOF structures was higher than 20 000.

In general, linkers for MOF synthesis are relatively rigid organic molecules with two or more functional groups that bind to the inorganic nodes. The binding sites are typically carboxylate groups or amines, but could also be hydroxyl groups or more rarely S- or P-containing groups such as sulfonates[36] and phosphonates[37]. The linkers typically get their rigidity from aromatic ring structures and/or double and triple bonds. They can vary a lot in size, from the shortest linkers such as oxalic acid in the range of a few Angstroms to the longest that can be around 5 nm, such as the linker in IRMOF-74-XI (IR = isoreticular) made by Deng et al.[38]. This linker is a chain of eleven phenylene rings with carboxylate and hydroxyl groups on both ends, and with methyl and hexyl groups attached to the rings. Due to the long linkers, IRMOF-74-XI has a 98 Å large pore aperture. In addition to size, shape and number of binding sites to the inorganic nodes, the linkers can be modified by attaching functional groups. These groups can for instance be hydroxyl groups, halides, amino-groups or nitro-groups. More advanced functionalizations include complexes with metal atoms such as Ir[39], Pt[34] or Ru[40]. A selection of linkers are shown in Figure 3. Other linkers used in MOF structures can be found in the review by Furukawa et al.[33].

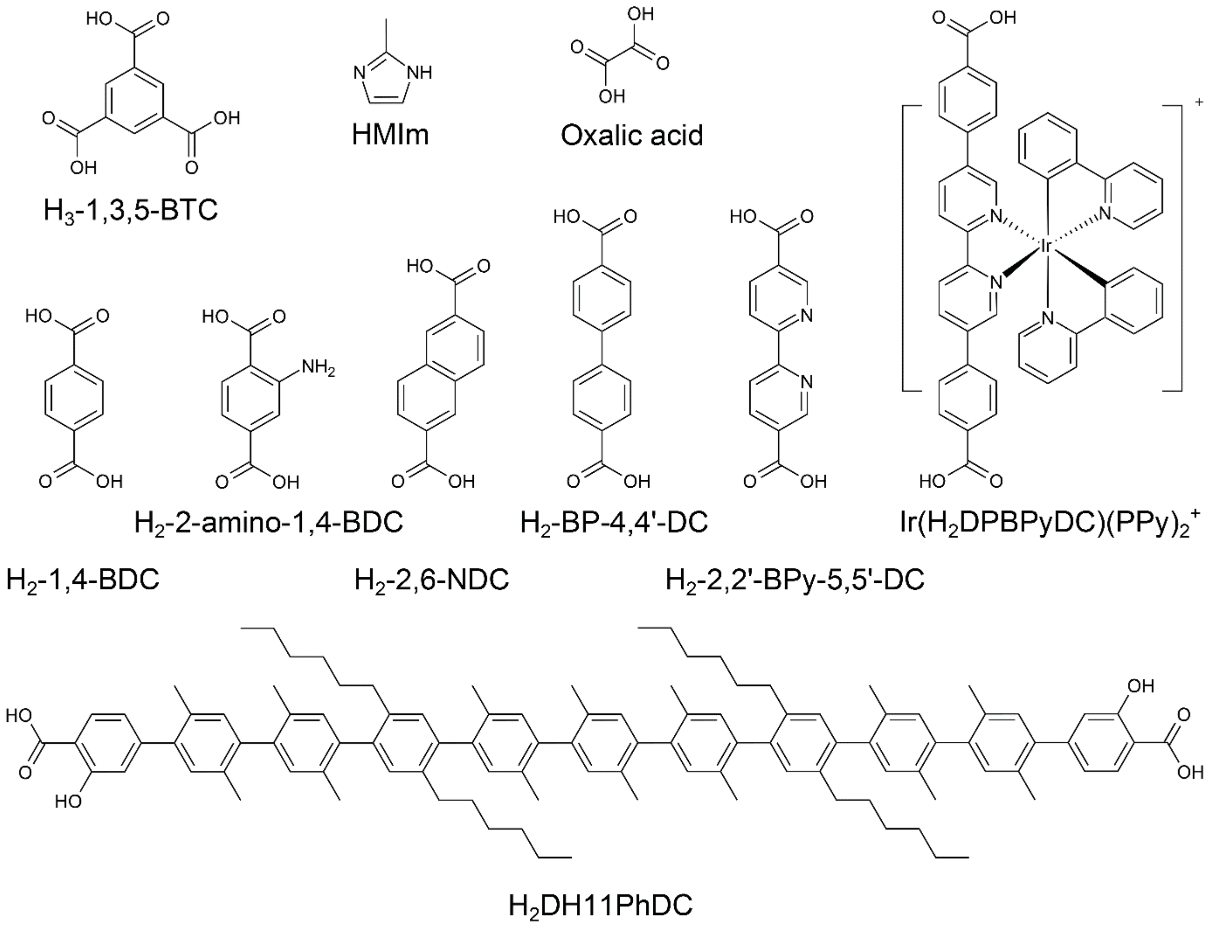

Figure 3: The protonated form of a selection of MOF linkers. 1,3,5-BTC = 1,3,5-benzenetricarboxylate; MIm = 2-methylimidazolate; 1,4-BDC = 1,4-benzenedicarboxylate; 2-amino-1,4-BDC = 2-amino-1,4-benzenedicarboxylate; 2,6-NDC = 2,6-naphthalenedicarboxylate; BP-4,4'-DC = 1,1'-biphenyl-4,4'-dicarboxylate; 2,2'-BPy-5,5'-DC = 2,2'-bipyridine-5,5'-dicarboxylate; DPBPyDC = diphenyl bipyridine dicarboxylate*; PPy = 2-phenyl pyridine; and DH11PhDC = dihydroxy 11 phenylene dicarboxylate*. *These names are not correct systematic names, but practical descriptions of otherwise too complex molecules, that have been taken from the review by Furukawa et al.[33].

2.2 MOF Synthesis

Due to the multidisciplinary nature of the MOF field when in its infancy, where scientists from various fields were attempting to achieve MOF synthesis, multiple approaches led to several synthesis techniques that are still used today. This has enabled a larger variety of MOF structures than what would have been possible with fewer approaches, since different techniques can give different structures even when the reactants are the same[27]. Different synthesis methods also enables control of the morphology of the product, which can be crucial for certain properties such as diffusion of guest molecules into the porous network and, by extension, catalytic activity[27]. Most traditional MOF synthesis techniques involve heating mixtures of precursors in a solvent. However, some solvent-free processes are available, and some synthetic procedures take place at room temperature. Most MOF syntheses yield powders as the final product, but a few techniques for thin-film synthesis are also available. Until recently, no processes for solvent-free formation of MOF thin-films were reported. Since the approaches to MOF synthesis vary quite a lot, this chapter will not cover all techniques, but an emphasis has been placed on the thin-film techniques. For a more complete overview, the review article by Stock et al.[27] is recommended.

2.2.1 Reaction Temperatures and Heating Methods

MOFs are normally synthesized at temperatures ranging from room temperature[41, 42] to above 200 °C[23, 43], in either open containers or sealed autoclaves. Normally, conventional electrical heating is used, but heating by microwave irradiation or by ultrasound is also possible. The heating method can affect the outcome of the synthesis due to differences in temperature profile *et cetera*, causing different conditions for nucleation and growth[44-46]. Bauer and Stock[47] have demonstrated the importance of temperature control in MOF synthesis. They varied the temperature between 17.0 and 99.9 °C while also varying the pH, resulting in the formation of six different phases of cadmium phosphonate.

2.2.2 Solvothermal Synthesis

Solvothermal synthesis of MOFs (referred to as hydrothermal synthesis when the solvent is water) is a quite common approach. A few different definitions of solvothermal synthesis are used, but the one given by Rabenau[48] defines it as syntheses in sealed autoclaves at temperatures above the boiling point of the solvent, causing elevated pressures. This approach comes from the background of zeolite synthesis, where solvothermal conditions are important[27]. Some MOFs that have been made by this technique are HKUST-1[49], UiO-66[26], MIL-100[23], and MIL-101[24].

2.2.3 Mechanochemical Synthesis

As mentioned above, heating is the most common way of introducing the energy required for the formation of MOFs. However, other methods such as mechanochemical synthesis are also used. Mechanochemical synthesis can be performed in several ways, such as with a pestle and mortar[50], ball milling[51-53] and by screw extruders[54]. Several of these techniques can be applied to make HKUST-1[52-55] but also other important frameworks, such as ZIF-8[54]. Mechanochemistry has opened the possibility of solvent-free synthesis of MOFs[51, 52, 54], however, the synthesis can also be liquid-assisted[56, 57]. Other advantages of mechanochemical synthesis include its high speed and the possibilities for scaled-up production.

2.2.4 Synthesis Techniques for MOF Thin-Films

A few different techniques for synthesis of MOF thin-films have been reported. Almost all of these are wet chemistry-based. Only recently, a few examples of gas phase depositions have been included, which will be covered in the chapter on ALD/MLD. The most common techniques are direct growth[58-63], layer-by-layer deposition[64-68], chemical solution deposition[69-71], seeded growth[59, 71-76], and electrochemical deposition[77, 78]. A review article covering MOF thin-films is written by Bétard and Fischer[79].

In the direct growth method, substrates for film deposition are submerged into a solution that could otherwise be used to synthesize powder, and treated in a similar manner. This is normally done under solvothermal conditions[58, 59, 62, 63], but not always[61]. The substrates can typically affect the film growth, and functionalized substrates, such as self-assembled monolayers (SAMs) on gold, may be needed[61, 62]. Some alternative approaches, such as contra-diffusion of two solutions from either side of a membrane[60], can also be classified as direct growth of MOF thin-films.

Layer-by-layer deposition (also known as liquid-phase epitaxy[67, 80]) can be described as the liquid phase equivalent of ALD, and typically requires a SAM-functionalized substrate[80] for the formation of MOFs. The substrates are dipped in a solution of the metal precursor, followed by a rinse in a neat solvent before they are dipped in linker solution and rinsed again. These steps are repeated in a cyclic manner to form the MOF thin-film.

Chemical solution deposition often relies on a dispersion of premade MOF nano-crystals, but a solution of precursors may also be used. The colloidal dispersion of particles are made through conventional synthesis methods such as solvothermal synthesis[69] and is subsequently deposited onto a substrate by for instance dip coating[69, 70] or spin coating[71].

Seeded growth is a technique where a higher quality film is made in a similar way as direct growth, but here, the substrate has a layer of seeding crystals deposited by other techniques. The seeding crystals guide the growth and eliminate the problem of nucleation. Seeding can take place by direct growth[75, 76], layer-by-layer deposition[74], spin coating[71], dip coating[72, 73], or rubbing[59].

Electrochemical deposition of MOF thin-films has also been done. This is a technique where the metal atoms forming the nodes in the MOF (for instance Cu or Zr) initially are found in metallic electrodes. The metal atoms are electrochemically oxidized and released into the solution were they can react with dissolved linker molecules forming a MOF film. Some examples of this approach include the HKUST-1 thin films made by Ameloot et al.[77] and the UiO-66 thin films[78] made by researchers from the same group. Ameloot and coworkers have also developed several other techniques for synthesizing MOF thin films with a focus on patterning of the films[81-83].

"Thin-films" that are made by the above-mentioned methods are not necessarily very thin. They can in some cases be as thick as 200-300 μm[59], but are normally in the range of 1-50 μm[58, 60, 61, 69, 71, 72]. In some cases, thinner films can be made, such as with the layer-by-layer method[66] or by dip coating[70] where the thinnest films can be approximately 40 nm.

3. Atomic Layer Deposition

Atomic layer deposition (ALD) is a technique that is very well suited for depositing thin, conformal films even on three-dimensional substrates. ALD has been used for many applications including electroluminescent displays, metal-oxide-semiconductor field-effect transistors (MOSFET), solar energy, microelectromechanical systems (MEMS), and more[84]. The technique was first described in the 1950s, -60s and -70s in Russia by Professor V. B. Aleskovskii and his student S. I. Kol'tsov under the name molecular layering[85], and was properly formalized in a 1975 patent by Suntola and Antson[86], who named it "atomic layer epitaxy". Later, the name was modified to "atomic layer deposition", which is now wildly used.

ALD is a technique that relies on gas to surface reactions of two (or more) gaseous precursors on a substrate. The process is normally carried out under vacuum, but in some cases also at ambient pressure[87, 88]. It is a cyclic process where each cycle consists of four (or more) steps:

1. **Pulsing the first precursor.** The first of (at least) two precursors is pulsed into the reaction chamber, where it reacts with and saturates the surface.
2. **Purge.** The pulse is followed by a purge step where the flow of an inert gas (typically N_2 or Ar) removes any excess precursor and the by-products from the reaction.
3. **Pulsing the second precursor.** The second precursor is pulsed into the reaction chamber where it reacts to saturation with the first precursor, which is adsorbed on the surface.
4. **Purge.** A new inert gas purge removes the second precursor and the by-products.

These four steps are shown in Figure 4 where the ALD growth of Al_2O_3 with trimethylaluminum (TMA) and water as precursors, is used as an example. The cycle is repeated until the desired film thickness is reached. The purge steps between the pulses prevent the precursors from meeting in the gas phase and ensures that the reaction only takes place on the surface of the substrates in a controlled way. The self-limiting growth during the pulses is achieved by ensuring that the precursors do not decompose or react with themselves, and enables only up to one monolayer of each precursor to be added with every pulse. It should be noted that some ALD reactors use a spatial separation of the precursors instead of the more common time separation that is described above and in Figure 4. In those reactors, a substrate is moved between zones containing the different precursors, that are created by alternating nozzles with precursors and inert gas all separated by exhausts to prevent mixing[87].

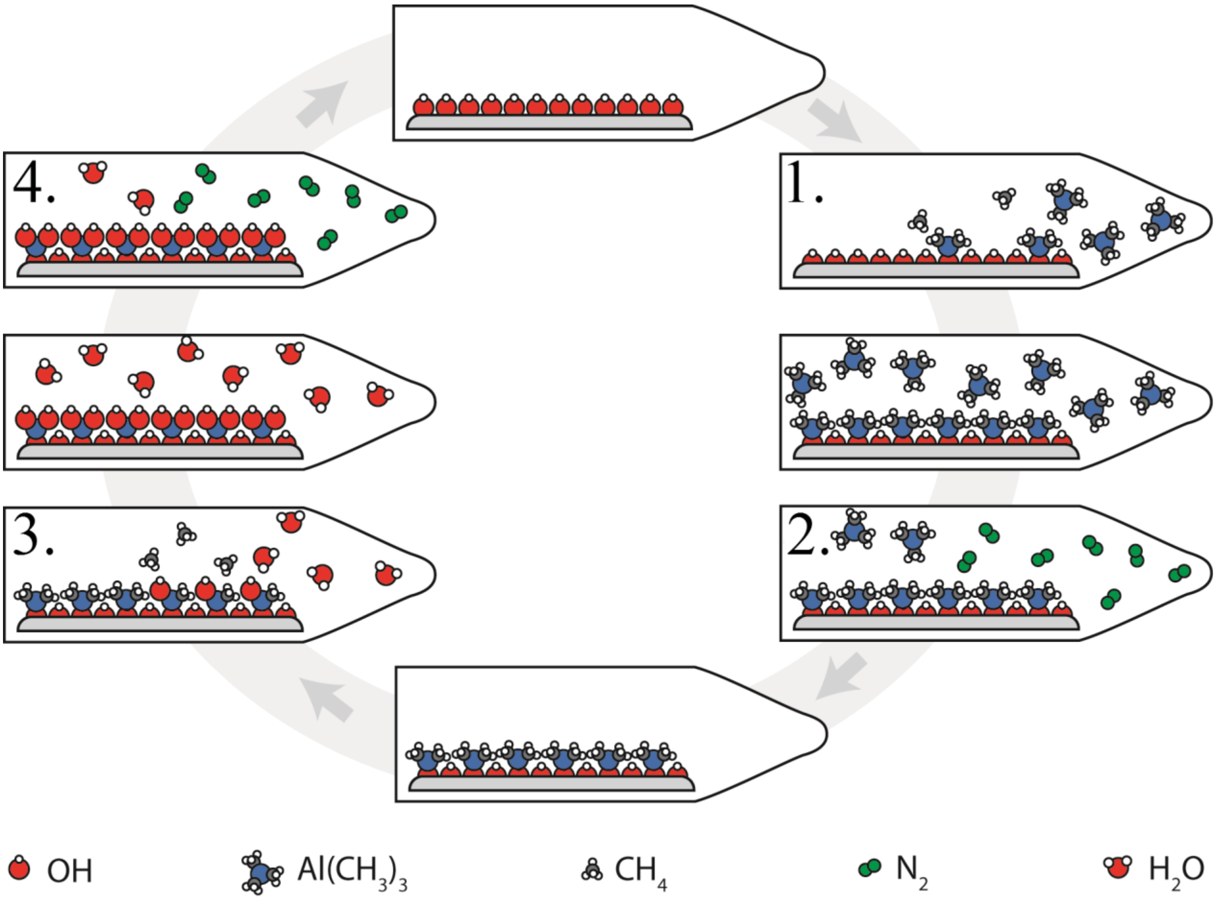

Figure 4: A sketch of ALD growth of Al_2O_3 with TMA and water as precursors. Adapted from the master thesis of Ingrid Vee[89].

The precursors that are used in ALD need to have a sufficiently high vapor pressure or a sufficiently low sublimation temperature so that it is possible to get them into the gas phase within the temperature ranges that can be used in ALD, i.e. without thermal decomposition occurring. Cation precursors are typically either metal-organic compounds such as TMA[90], diethylzinc (DEZ)[91], and titanium tetraisopropoxide (TTIP)[90]; or metal halides such as $TiCl_4$[90, 92, 93], $ZrCl_4$[90, 94], and $AlCl_3$[90, 95]. These are then combined with for instance water[90], ozone[96, 97], ammonia[98] or other compounds to form oxides, nitrides or other classes of materials. Available precursors exist for a majority of the elements in the periodic table, and it is possible to make various classes of materials such as oxides[90], nitrides[98, 99], fluorides[100, 101], sulfides[102], and metals[103, 104], to name a few. In addition to these, a class of organic-inorganic hybrid materials can be prepared by allowing metal precursors to react with organic molecules. This method is often called MLD, and is further described in the next section. A quite extensive review on ALD was published by Miikkulainen et al.[84] in 2013.

Several parameters can be adjusted in order to obtain controlled growth. One of these is the reaction temperature, which can affect the growth rate in different ways. A too low temperature can in some cases lead to condensation of the precursors on the substrate and consequently to a too high growth rate. In other systems, however, a too low reaction temperature can lead to a too low growth rate due to an incomplete reaction between the precursors and the surface. On the other hand, if the reaction temperature is too high, there is a risk of either decomposition or desorption of the precursors leading to either too high or too low growth rate, respectively. If the growth rate is unaffected by the temperature within a certain temperature range, this range is referred to as the ALD-window. Systems with well-defined ALD-windows are less affected by temperature gradients in the reaction chamber, and controlled growth on large substrates can be easier.

In addition to the reaction temperature, pulse- and purge-lengths are important parameters to tune in order to obtain controlled growth. A too short pulse will always give a too low growth rate, and a too long pulse may give a too high growth rate if the growth is not completely self-limiting. The effect of the purge-length depends on whether the adsorption of the precursor is reversible (physisorption) or irreversible (chemisorption). If it is partly reversible, a too short purge may give a too high growth rate due to some physisorption of the precursor. If the adsorption is fully reversible, a too long purge will give no growth at all. Figure 5 shows proper pulse and a purge lengths for an ideal system with no physisorption and self-limiting growth, and a system with some physisorption of the precursor. These are compared to a case where the pulse is too short and a case with some physisorption, and a too short purge.

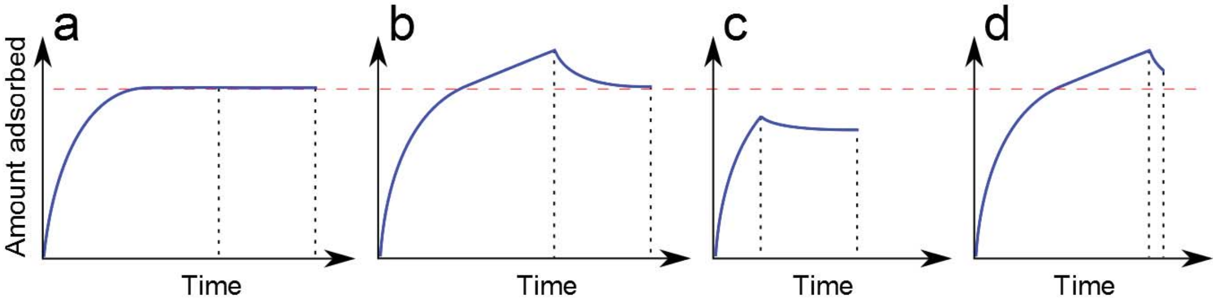

Figure 5: (a) A system with irreversible, saturated growth (only chemisorption). (b) A system with some physisorption of the precursor with proper pulse- and purge-lengths. (c) And (d) the effects of a too short pulse and purge respectively, in the same system as (b). The black, dotted lines indicate the ends of pulse- or purge-sequences, and the red dashed line indicates the adsorbed amount of one chemisorbed monolayer.

The main advantages of ALD include a very good thickness control, and therefore highly conformal films. In addition, ALD gives conformal films on irregular substrates such as substrates with trenches, porous substrates or other three-dimensional substrates. This is possible since the technique relies on gaseous precursors that will react with any available surface. When these advantages of ALD are combined with the possibility to make a wide range of different materials, it becomes evident that ALD is a very useful technique for a wide range of applications, some of which are mentioned in to beginning of this chapter. However, ALD has some drawbacks, such as being a very slow process. A typical growth rate with ALD can be 1 Å per cycle. Making a 100 nm thick film requires 1000 cycles, which, depending on the length of the cycle, can take up to several hours. In addition to the actual deposition time, comes the time needed for heating and cooling of the reactor, and the time spent on reaching vacuum before the deposition, and reaching ambient pressure after the deposition. The cost of some of the precursors used can also be rather high.

3.1 Molecular Layer Deposition and Hybrid Materials

Molecular layer deposition (MLD) is closely related to ALD, differing only by the fact that the films are built by larger molecular units with every deposition cycle. The term MLD was first applied for deposition of purely organic polymer films by Yoshimura et al.[105] in 1991. Using this technique, polymers such as polyimides[106, 107], polyamides[108-110] (including nylon 66[109]), polyurea[111], and poly ethylene terephthalate (PET)[112] have, among others, been synthesized as thin films. The review articles by Meng et al.[113] and Leskelä et al.[114] cover this development in more detail.

One disadvantage with this approach to deposition of organic polymer films is that it is quite time consuming. Rather long pulses are required to achieve saturation and an ALD-type growth[114], probably due to the relatively low vapor pressure of the organic precursors used for these processes and their slow reaction kinetics. The growth rate per cycle, however, is higher than conventional ALD systems. This is because the size of the organic monomers are much larger than that of the single atoms deposited with every pulse in a traditional ALD deposition.

By allowing the organic monomers used in MLD synthesis to react with metal precursors from traditional ALD such as TMA, DEZ, $TiCl_4$ or others, the reaction kinetics become significantly faster. In such manner, organic-inorganic hybrid materials are made, a class of materials that combine the functionalities of inorganic and organic materials and are similar to the MOFs described in chapter 2.

This combination of the MLD approach for polymers and the traditional ALD of inorganic materials to form hybrid materials, was first described in a patent submitted in 2004 by Nilsen et al.[115]. Technically, the method is most accurately described as a combination of MLD and ALD since the metal precursor pulses add one atomic layer to the film and the organic precursor pulses add one molecular layer to the film. However, since MLD and ALD in principle are the same technique only varying in type of precursors, both names have been used for hybrid film growth described in the literature. In this thesis, the term MLD will be used.

Since these hybrid materials combine properties from both organic and inorganic materials, they are interesting for a wide range of different applications. Some hybrid films have been observed to have semiconducting properties[116], others have been made as transparent conductors[117] or as organic-based magnetic materials[118], while some have been proposed as battery materials[119]. Since hybrid materials are related to MOFs, a range of applications that utilize the porosity of MOFs could also be possible. These include membranes, sensor materials and low-κ dielectrics, as envisioned by Allendorf et al.[3]

Some of the first hybrid materials that were deposited by MLD were the results of reactions between metal precursors and diols. The product from these reactions form a materials class that is known as "metalcones", and a number of subclasses are known, including alucones[120-123], zincones[123, 124], and titanicones[119, 123]. These "metalcone"-films tend to be air sensitive[120, 121], which is likely due to a low coordination of the metal atoms. More stable films can be made when the hydroxyl groups in the organic precursors are substituted with carboxylic acid groups. The carboxylate groups give a more complete coordination since they also can contribute with their carbonyls as coordinating groups, i.e. twice the number of oxygen atoms as for hydroxyl groups. For Al as bonding element, this results in six coordinating oxygen atoms and most probably an octahedral environment, which stabilizes the film. Typically, dicarboxylic acids have been used[125, 126] but also tri-, or tetracarboxylic acids are possible precursors[127].

Another challenge that has been observed in MLD is that both functional groups in a bi-functional organic molecule can react with the surface. This blocks binding sites for other precursor molecules and leaves no remaining functional groups for the next pulse of reactants. Such double reactions typically occur if the organic precursor has a flexible carbon chain as its backbone and lead to a drop of the growth rate after a few cycles[119]. One way to overcome this is to use more rigid, organic molecules with double bonds in the carbon chains or aromatic ring structures[125, 127].

As mentioned in chapter 2.1, such rigid organic molecules are also used as linkers in MOFs, which means that MLD with these organic precursors can give MOF thin films. This has been demonstrated by Salmi et al. who have made thin films of MOF-5[128] and IRMOF-8[129]. These films were amorphous as deposited, but could be crystallized to the abovementioned MOF structures by exposure to moist air and a subsequent autoclave treatment in dimethylformamide (DMF). Other examples of synthesis of crystalline MOF films by MLD include the copper(II)terephthalate[130] and iron terephthalate[131] films made by Karppinen and coworkers, and the work presented in this thesis[132, 133]. In these cases, the MOF films were made by all-gas-phase techniques. The copper(II)terephthalate and iron terephthalate films were crystalline as-deposited, and in the work presented in this thesis, a gas-phase crystallization step was developed. Karppinen and coworkers have also deposited several other coordination polymers based on s-block metals[134-136]. These have had a tendency to be crystalline as deposited for certain temperatures, but they have not been reported to be porous.

Another approach for making MOFs by ALD was demonstrated by Stassen et al.[137] who deposited ZnO thin films by conventional ALD, and subsequently allowed these films to react with a vapor of the organic linker molecules to form ZIF-8.

In the works mentioned above, the porosity of the MOF films was demonstrated in various ways. Stassen et al.[137] used krypton physisorption for their ZIF-8 films, while Ahvenniemi and Karppinen[130] see an indication of porosity in their copper(II)terephthalate films from the density measured by X-ray reflectivity (XRR). These two studies are the first examples of porous thin films made by all-gas-phase techniques. However, Salmi et al. achieved porosity in their MOF-5[128] and IRMOF-8[129] films after solvothermal treatment. This was demonstrated for the MOF-5 films by a change in the refractive index when the films were loaded with isopropanol. For the IRMOF-8 films, the porosity was demonstrated by an ability to load the films with Pd by using a vapor of $Pd(thd)_2$ (thd = 2,2,6,6-tetramethyl-3,5-heptanedione). Also in the work presented in this thesis, a porosity is seen in the films as will be described in chapter 5.4.

4. Characterization Methods

Characterization is a vital part of materials research, both as an aid to understand the chemistry and to explore the properties and structure of the newly formed materials. This chapter focuses on the different characterization methods used throughout this project to provide the reader with a sufficient understanding of their working principles. In addition, a short reasoning for the choice of techniques, and why they were useful for this work, is given. The techniques will not be described in detail; for each method, the reader will be referred to more comprehensive literature in the fields.

4.1 Spectroscopic Ellipsometry

Spectroscopic ellipsometry (SE) is a technique highly suitable for measuring the thickness and refractive index of thin films. It relies on the fact that the reflectance of a polarized beam of light is different for light where the electrical field oscillations are polarized perpendicular (s, from German "senkrecht") compared to parallel (p) to the plane of incidence, which is defined as the plane in which the incoming and reflected beams travel, Figure 6. The incoming light is linearly polarized with components in both the s and p direction. The light that reflects off the film and the substrate becomes elliptically polarized. The ellipsometer measures the ratio between the complex amplitudes of the s and p components after the reflection (R_s and R_p). This ratio can be written as:

$$\rho = \frac{R_s}{R_p} = \tan\psi e^{i\Delta} \tag{1}$$

where ψ is ratio between the absolute values of R_s and R_p, and Δ is the phase shift between the s and the p components of the reflected light. The two parameters ψ and Δ indirectly contain information about the optical properties of the material on the surface that reflected the light. This information can be extracted by using the Fresnel equation. When the reflected light from both the film and the substrate are taken into consideration, it is also possible to determine the thickness of the film, which is found by fitting the data to a known function such as the Cauchy function:

$$n(\lambda) = n_0 + \frac{n_1}{\lambda^2} + \frac{n_2}{\lambda^4} \tag{2}$$

where $n(\lambda)$ is the refractive index as a function of the wavelength, and n_0, n_1, and n_2 are fitting parameters. When $n(\lambda)$ is known, the thickness of the film can be determined. Theeten and Aspnes[138] describe ellipsometry in more detail for further information.

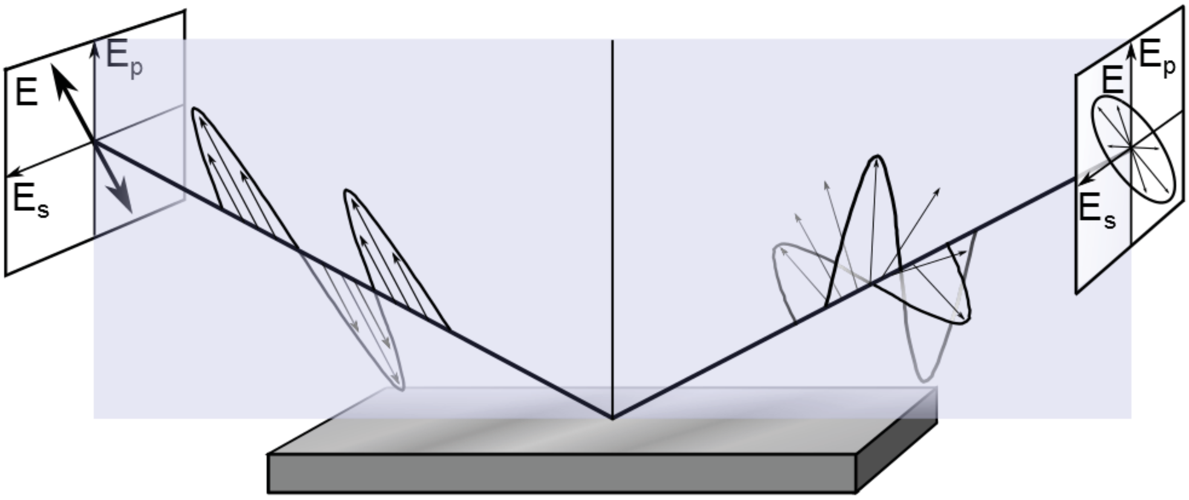

Figure 6: A sketch of the working principle of SE where linearly polarized light comes in from the left and elliptically polarized light reflects off the sample. The plane of incidence is marked as translucent blue.

In the present work, the thickness and refractive index of most films were found by SE. The films were for the most part considered to be transparent to the wavelengths that were used and analyzed using the Cauchy model. However, the absorbance of part of the blue light of films in **Paper II** was taken into account by creating a general oscillator model with a Gaussian absorption at around 3.7 eV or 335 nm for that purpose.

4.2 Quartz Crystal Microbalance

A powerful tool for investigating the growth of an ALD system *in situ* is quartz crystal microbalance (QCM). This technique was first described by Sauerbrey[139], and uses the piezoelectric properties of a quartz crystal. An alternating electric field is applied to the crystal to induce oscillations around its resonant frequency. The frequency of the oscillations is affected by the overall mass of the crystal, and is sensitive enough to detect a fraction of an atomic layer. This sensitivity is exploited in detection of variations in mass during ALD or MLD pulses.

In situ QCM has been used to determine the required pulse- and purge-lengths for self-limiting ALD-type growth for every system in the work presented in this thesis. This was performed by defining a standard sequence of pulse- and purge-lengths, and measuring the growth rate while varying each parameter individually. In addition, QCM was used to investigate the porosity of the films by measuring the mass increase due to absorption of water during a water pulse in the ALD reactor, in films that were deposited on QCM crystals. This was compared to the corresponding mass increase on uncoated crystals for reference.

4.3 Fourier Transform Infrared Spectroscopy

The different vibrational modes in in a molecule have unique energies depending on the type of bonds and functional groups affected. The modes of vibration can be stretching (change in bond lengths), bending (change in bond angles), or combinations of these such as twisting, rocking, symmetric stretch, and asymmetric stretch, Figure 7. The energies associated with these vibrational modes correspond to the infrared part of the electromagnetic spectrum. In Fourier transform infrared spectroscopy (FTIR), light is either reflected off or transmitted through a sample. Certain wavelengths that correspond to one of the vibrational modes in the sample will then be absorbed, which leads to a spectrum with absorption peaks containing information about the bonds that are present in the sample.

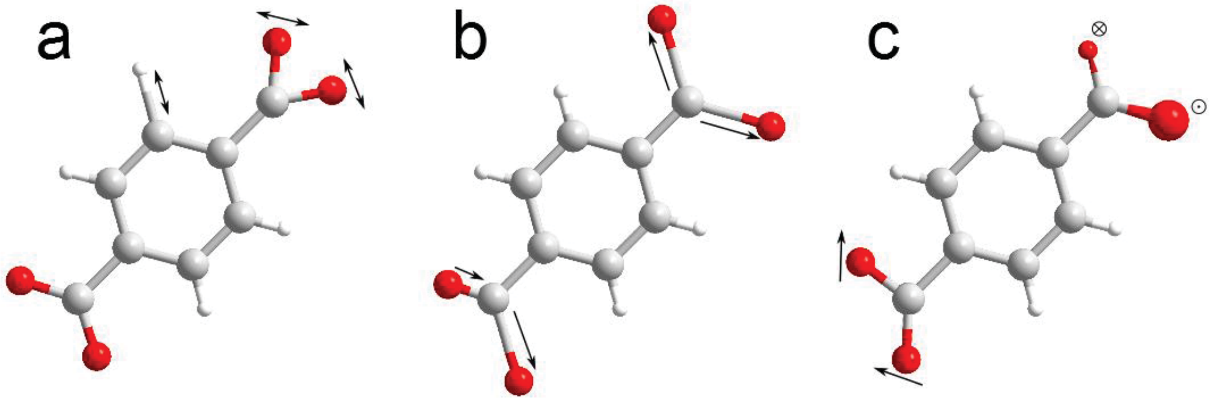

Figure 7: Some examples of vibration modes in a 1,4-BDC linker from a MOF structure. (a) Stretching of a C-H bond, and bending in the carboxylate group. (b) Asymmetric (bottom left) and symmetric (top right) stretch in the carboxylate group. (c) Rocking (bottom left) and twisting (top right) of the carboxylate group.

In FTIR, data are acquired by sending a beam of broad-band light through a beam splitter, which directs part of the light towards a fixed mirror, and the rest of the light towards a moving mirror. After reflection off these mirrors, parts of the light are recombined by the beam splitter, and directed towards the sample. Due to the different optical path lengths of the light, constructive and destructive interference will allow only some wavelengths to reach the sample. By changing the position of the movable mirror to alter the optical path length of the light, the wavelengths that reach the sample can be varied. After an interaction with the sample (either reflection or transmission), the beam finally reaches the detector. The raw data can then be converted to a spectrum by Fourier transformation. More information on FTIR is found in the book by Griffiths and De Haseth[140].

In this work, FTIR has mostly been used to investigate the bonding mechanism of the carboxylate group to the Zr atoms in the films. In addition to that, it has been used to verify that the amino group still is present, and unreacted in the case where 2-amino-1,4-BDC was used.

4.4 X-ray Diffraction

X-ray diffraction (XRD) is a suitable technique for determining the crystal structure of a material. It utilizes elastic scattering between incoming X-ray photons and electrons in the atoms. Photons that are scattered by two atoms in neighboring crystal planes will interfere with each other. This interference will be constructive when the angle of the incoming beam (θ) is right. Bragg's law gives the relationship between the plane separation distance (d), the angle (θ), and the wavelength (λ) of the radiation:

$$n\lambda = 2d\sin\theta \tag{3}$$

where n is a positive integer number called the order of the reflection. By scanning over different angles and measuring the intensity of the reflected beam, a diffractogram is obtained, which can be used to determine the crystal structure of the material. XRD can be done with several different geometrical setups. One of the most common scan types is a θ-2θ-scan where the X-ray source is stationary and aimed at the sample, the sample rotates with the angle θ, and the detector moves by the angle 2θ. Another option is grazing incidence X-ray diffraction (GIXRD) where the X-ray source and the sample are both fixed with a small angle (α) between the incoming beam and the surface of the sample, and the detector scans over a larger range. The advantage of GIXRD for thin film samples is that the small incoming angle causes the X-ray beam to have a longer interaction path through the film, increasing the intensity of the reflections coming from the thin film material. For more information about XRD specifically for thin film analysis, the book by Birkholz[141]is recommended.

The GIXRD setup was most frequently used during this investigation. It was used to study the crystallinity of thin film samples that had been treated in varying manners.

4.5 X-ray Reflectivity

X-ray reflectivity (XRR) is performed in a similar way to XRD with the θ-2θ configuration, however at much lower angles than XRD measurements. By starting close to 0°, total reflectance of the X-ray beam occurs up to a point when a so called critical-angle is reached. This angle is material dependent and related to its density. After a further increase of the angle of the incoming beam, oscillations of the reflected intensity known as Kiessig fringes or oscillations, are observed. The Kiessig fringes are formed due to constructive interference between the reflected beam from the surface of the film, and the refracted beam from the film-substrate interface. The distance between the peaks of the Kiessig fringes can be used to determine the thickness of the film in the same way as the distance between crystal planes are found in XRD. The roughness of the film and the substrate can also be determined by XRR, and are related to the dampening of the amplitude in the Kiessig oscillations. For more information about XRR, see the books by Birkholz[141], and Daillant and Gibaud[142].

XRR has here been used to determine the density and thickness of a selection of films deposited with the standard pulse- and purge-lengths used in the QCM experiments. From this information a conversion factor for the QCM results could be calculated in order to convert a change in frequency of the oscillations in the crystal to a change in mass of the film deposited on the crystal.

4.6 Scanning Electron Microscopy

A scanning electron microscope (SEM) uses interactions between an electron beam and the sample surface to generate high-resolution images of the samples and collect other information[143]. The electrons come from a filament and are accelerated towards the sample by an applied voltage, for SEM normally in the range of 1-30 kV. The electrons are guided and focused by magnetic lenses that are also used to scan the beam over the sample. Electrons can experience either elastic or inelastic scattering upon interaction with the sample surface. The scattered electrons from every point the beam scans over are counted by a detector in order to form an image. Two important imaging modes are back scattered electron imaging and secondary electron imaging based on the elastic and the inelastic scattering, respectively. These two modes give complementary information, the former gives contrast based on the average atomic mass of the elements in different areas in the image, and the latter gives contrast due to topographic features. In addition to the scattering of electrons, characteristic element-specific X-ray photons are emitted from the atoms in the sample. This enables mapping or quantification of the chemical composition through a technique called energy dispersive X-ray spectroscopy (EDX, also known as EDS). More about SEM with a focus on the early history of the technique can be found in a paper by McMullan[144].

The SEM images in this thesis were collected using the secondary electron imaging mode, and were useful for investigating differences in sample topography before and after certain treatments such as the autoclave-treatment that crystallized the films.

4.7 Other Techniques

A selection of other techniques have also been used, though more sparsely. These are listed below with a short description of their working principles and why they were used. References to further literature on these techniques are also provided.

4.7.1 Atomic Force Microscopy

An atomic force microscope (AFM) was used in **Paper I** to further investigate the topography of the crystalline UiO-66 sample. The technique uses a cantilever with a sharp tip to scan the surface. Data can be collected in a few different ways such as contact mode or non-contact mode. In contact mode, a laser beam is reflected off the backside of the cantilever to a segmented photoelectric detector. When the cantilever is deflected by topographical features on the sample, the reflected laser beam shifts between the segments of the photodetector and forms a feedback loop to the z-scale position of the sample to form a three-dimensional image of the surface of the sample. In non-contact mode, however, the cantilever is set to oscillate above the sample. The frequency of the oscillation is affected by forces between the sample and the tip on the cantilever, and the observed frequency variations are used to reconstruct an image of the sample surface. Non-contact mode was used for imaging the UiO-66 samples since contact mode is likely to damage the sample while scanning. A further description of AFM is given by Hunger et al.[145].

4.7.2 Contact Angle Measurements

Contact angle measurements were used in **Paper II** to investigate the difference in hydrophilicity between films containing 1,4-BDC and films containing 2-amino-1,4-BDC. When a drop of a liquid is placed on the surface of a solid, surface tension and external forces such as gravity determine its shape so that the total surface free energy (between the solid and gas, solid and liquid, and liquid and gas) is minimized. The angle between the solid-liquid interface and the tangent of the droplet surface curvature in the contact point then becomes a measure of the surface free energy. If the liquid is water, the contact angle gives a measure of the hydrophilicity of the surface. More information on contact angle measurements is found in the book chapter by Yuan and Lee[146].

4.7.3 X-ray Fluorescence

X-ray fluorescence (XRF) was used to determine the amount of chlorine in a selection of the samples. It is a technique where X-rays are used to excite core electrons in the atoms of a sample out to vacuum level. When another electron in a higher energy state relaxes to the now vacant energy level, fluorescence in the form of X-rays are emitted. The energy of the emitted X-rays are characteristic for the different elements. For more information on XRF, the reader is referred to the handbook by Beckhoff et al.[147].

4.7.4 Thermogravimetric Analysis

Thermogravimetric analysis (TGA) has been used in this work to determine the temperature for sublimation for some possible precursors. In TGA measurements, a small amount of a material is heated in a crucible while very accurately measuring its weight, which decreases when the material is dried (loss of water), vaporized, or is decomposed to form gaseous products. More information on TGA is found in the review by Coats and Redfern[148].

5. Results and Discussion

In this chapter, the most important results from the supporting papers will be presented, discussed, and put in context with each other and with relevant literature.

At the start of this project in 2014, the reported cases of thin film growth of MOFs by MLD were almost nonexistent. One contribution from 2013 by Salmi et al.[128] demonstrated that MOF synthesis by MLD was possible by post-processing films to form the MOF-5 structure by exposing the as-deposited films to moist air and subsequently treating them in an autoclave with DMF. Salmi et al. also used a similar method to make IRMOF-8[129] in 2014.

The first all-gas-phase process for making MOF-thin films was presented in 2015 by Ahvenniemi and Karppinen[130], who were able to make thin films of copper(II)terephthalate, a material with the MOF-2 type structure. Their films were crystalline as-deposited, and did not need any post deposition treatment. Less than a month later, Stassen et al. published an article where they demonstrate a method for making MOF thin films by depositing a precursor layer of ZnO[137]. When this film is exposed to a vapor of the linker molecules 2-methylimidazole at 100 °C it reacts to form the MOF ZIF-8. A challenge with most MOF materials is their limited thermal and environmental stability. Our focus from the beginning was therefore on UiO-66 and related structures based on similar zirconium clusters. UiO-66 is known for its good chemical and thermal stabilities[149] and is therefore a natural choice for applications where exposure to water is expected. The synthesis of UiO-66 thin films is presented in **Paper I**[132], and was performed by combining $ZrCl_4$ with 1,4-benzenedicarboxylic acid (H_2-1,4-BDC) as precursors in an MLD process, followed by a crystallization step that will be described in chapter 5.3.

The subsequent works in this thesis describe similar syntheses where other linkers than 1,4-BDC were used. The organic precursor from **Paper I** was substituted with one of the following precursors: 2-amino-1,4-benzenedicarboxylic acid (H_2-2-amino-1,4-BDC), 2,6-naphthalenedicarboxylic acid (H_2-2,6-NDC), biphenyl-4,4'-dicarboxylic acid (H_2-BP-4,4'-DC), or bipyridine-5,5'-dicarboxylic acid (H_2-BPy-5,5'-DC), Figure 8.

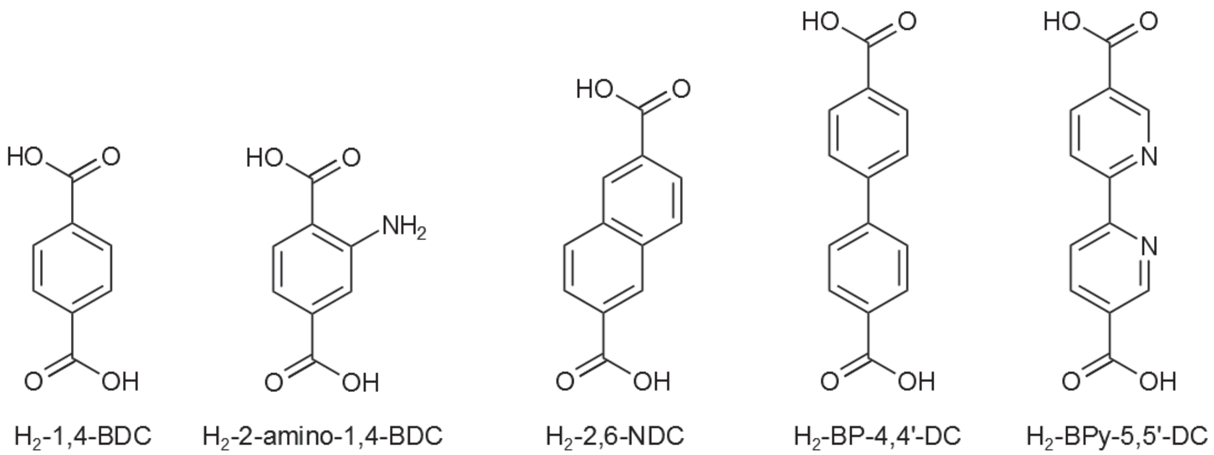

Figure 8: The organic precursors that have been used in this work and their abbreviations.

The motivation for using these linkers was the desire to synthesize MOFs with different chemical properties or larger pore sizes than UiO-66. This led to **Paper II**[133] and **Paper III** where several MOF phases were synthesized, including a structure related to UiO-66-NH_2, UiO-67, and a few unknown phases. Enabling MOF thin-films with various pore sizes could be useful, since certain applications such as membranes for size dependent separation of molecules, may strongly depend on a very exact pore size. A change in chemistry in a MOF linker can also result in new properties, for instance catalytic activity, which is seen in the UiO-66-NH_2 structure[11]. In the case of the UiO-67-bpy MOF structure (UiO-67 where some of the linkers are substituted with the BPy-5,5'-DC linker), the chemical change compared to regular UiO-67 can open for further post-synthetic functionalization of the MOF[150].

From the FTIR analyses and contact angle measurements in **Paper II**, we have found that chemically functionalized MOFs with amino groups on the linkers were made. We have also obtain indirect proof of an increase in pore size when longer linkers were used (discussed in chapter 5.4).

5.1 MLD Growth Dynamics

All of the deposition systems, which are combinations of $ZrCl_4$ and one of the organic precursors from Figure 8, were investigated with *in situ* QCM. This gave insight into the growth dynamics and determination of the optimal pulse and purge lengths for each system. In addition, the growth rate of the deposition systems at various temperatures was determined using SE analysis of the as deposited films on Si substrates.

In this chapter, the QCM and SE measurements will be discussed to shed light on the growth rate and growth dynamics, and how they are affected by temperature or the size, shape and chemistry of the linkers. The difference in growth dynamics was also supported by FTIR spectroscopy, which revealed a presence of various binding modes between Zr atoms and the linker molecules.

The as-deposited films from all deposition systems were flat and amorphous with growth rates that spanned from ca. 2 to 12 Å per cycle depending on temperature and length of linker. In general, the growth rate was large compared to conventional ALD systems, and similar to the growth rate of other organic-inorganic hybrid materials[127] made in an MLD manner.

At a reaction temperature of 290 °C, the growth rate of the Zr-1,4-BDC system was 5.8 Å per cycle. This is slightly less than the length of one linker (roughly 7 Å[38]) plus one Zr atom. This indicates that the growth of these films either was less than one monolayer with every cycle or that the orientation of the linker molecules was not perpendicular to the substrate surface, or a combination of the two. FTIR spectra of these films supported that a combination of tilted orientation and growth by less than one monolayer per cycle was the case. The spectra (displayed in chapter 5.2 and **Paper I**) show that the coordination between Zr atoms and linker molecules was a combination of monodentate and bidentate, which gives two different orientations of the linker molecules while crystalline UiO-66 only has bridging coordination. Such mixture of orientations indicates that the surface coverage of the linker was less than 100 % since the differently oriented linkers will come in conflict with each other leading to blockage of some binding sites on the surface. This mix of orientations also means that at least some of the linkers do not grow perpendicular to the surface.

The growth rate of the amino-functionalized films deposited with the same reaction temperature as above was ca. 10 Å per cycle, which is significantly higher than that of the Zr-1,4-BDC system. FTIR spectra of these films (see **Paper II**) showed that 2-amino-1,4-BDC only had a bidentate coordination to Zr, leading to only one orientation mode of the linkers to the substrate surface. This gives a more complete surface coverage than a combination of two different orientations, and leads to the observed high growth rate. One possible reason for the lack of monodentate coordination in this system is that this coordination was prevented by steric hindrance. The bulky amino group on a linker with bidentate coordination to Zr could prevent its neighboring linkers from forming a monodentate coordination to Zr as illustrated in Figure 9. It should be mentioned that a growth rate of 10 Å per cycle is slightly higher than what we would expect with one linker (roughly 7 Å[38]) plus one Zr atom per cycle. This could indicate that there is a component of chemical vapor deposition (CVD) growth in this system, possibly due to reservoir effects from the porosity of the films. A growth rate of 10 Å per cycle is still less than the theoretically highest possible growth rate for a UiO-66 structure, which would be 14.7 Å per cycle if the orientation of the growth is in the [111] direction. However, we do not expect that the clusters of the MOF structure form in the ALD reactor, so an assumption of growth of one linker and one Zr atom with every cycle is perhaps more precise.

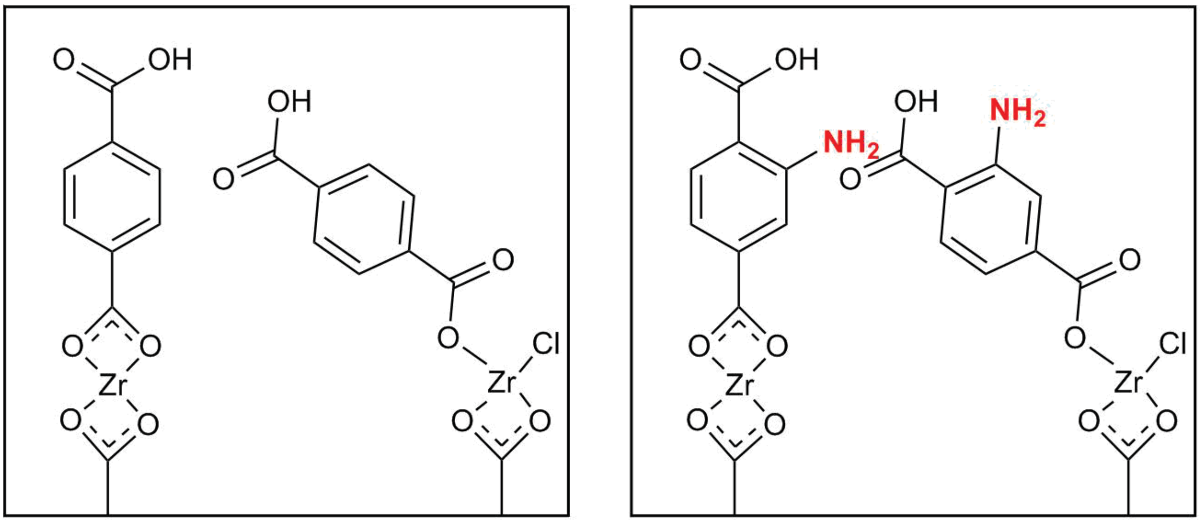

Figure 9: An illustration of the steric hindrance preventing amino-functionalized linker from forming a monodentate coordination to Zr (right) compared to the same situation for the non-functionalized linker (left), adapted from Paper II.

By comparing the growth rate of the Zr-1,4-BDC system to the systems where the linker was either 2,6-NDC or BP-4,4'-DC, we observed that the growth increased with increasing linker length. As mentioned above, the growth rate of Zr-1,4-BDC was 5.8 Å per cycle at 290 °C, whereas for Zr-2,6-NDC and Zr-BP-4,4'-DC the growth rates were 7.7 and 11.5 Å per cycle, respectively.

The difference in growth rate per cycle of these three systems is comparable to the difference in length between the shortest and the two longer linkers as calculated from the C-C bond lengths in aromatics, and between aromatics[151]. The calculated length difference between 1,4-BDC and 2,6-NDC is 2.1 Å[d], and between 1,4-BDC and BP-4,4'-DC, the difference is 4.3 Å[e], Figure 10. The observed differences in growth rate were 1.9 and 5.7 Å per cycle, respectively, which is not too far from the calculated length difference, especially if we consider a probable difference in the growth dynamic between the three systems.

---

[d] $1.397\ \text{Å} \times (1 + \cos(60) = 2.0955\ \text{Å}$

[e] $1.397\ \text{Å} \times (1 + \cos(60)) + 1.492\ \text{Å} = 4.2860\ \text{Å}$

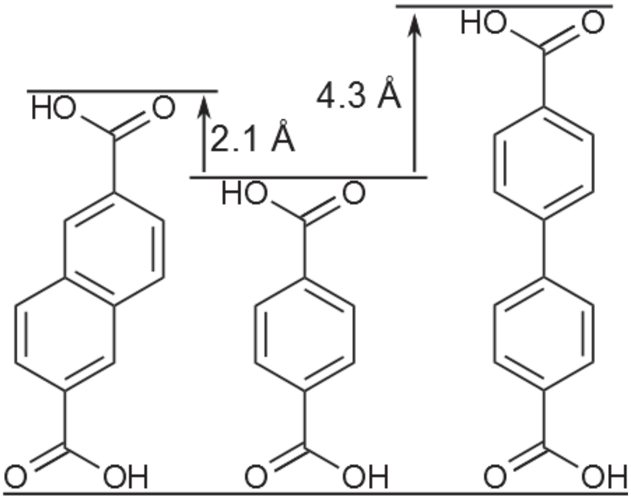

Figure 10: An illustration of the calculated difference in length between the H_2-1,4-BDC molecule (middle) and the longer H_2-2,6-NDC (left) and H_2-BP-4,4'-DC (right) molecules.

The growth rate of the films generally decreased with increasing temperature, Figure 11. This is in agreement with previously observed behavior for many hybrid films[125-127], and may be due to partial desorption or decomposition of the precursors at higher temperatures. The sudden increase in the refractive index of the Zr-1,4-BDC films, and the decrease in luminescence from the Zr-2,6-NDC films at higher deposition temperatures, both indicate that decompositions may have occurred. The only system that seems to have an ALD-window, is the Zr-2,6-NDC system where the growth rate was relatively stable at around 8 Å per cycle between 290 and 340 °C.

The difference in growth rate between the systems can also be seen from the QCM measurements, which give a better insight into the growth dynamics. Figure 12 shows the mass increase as a function of time for the Zr-1,4-BDC system, deposited at 265 °C. From this figure, we can see that the deposition has an ALD-type growth with stepwise, saturated mass increases with every pulse, and almost no mass loss during the purges.

A similar graph is seen for the system with 2-amino-1,4-BDC in Figure 13, although with a larger mass increase with every cycle. The mass increase was larger in the amino-functionalized system mostly because the growth rate was higher for that system, as discussed above, but it is in part also an effect of added mass of the amino group.

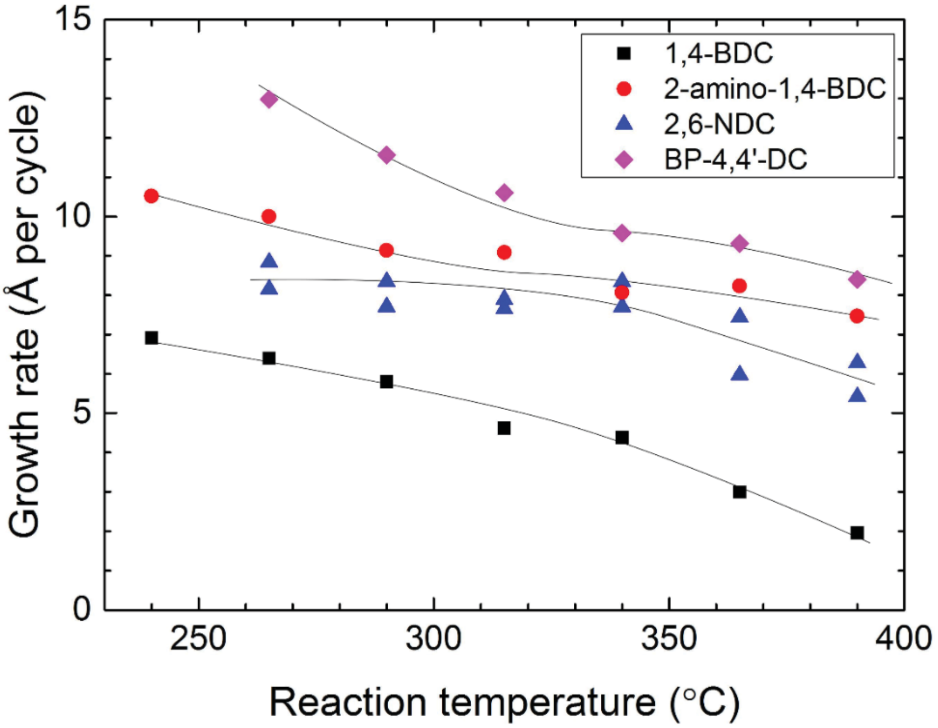

Figure 11: Growth rates as functions of temperature for all tested systems (except Zr-BPy-5,5'-DC). The Zr-2,6-NDC series was repeated two times.

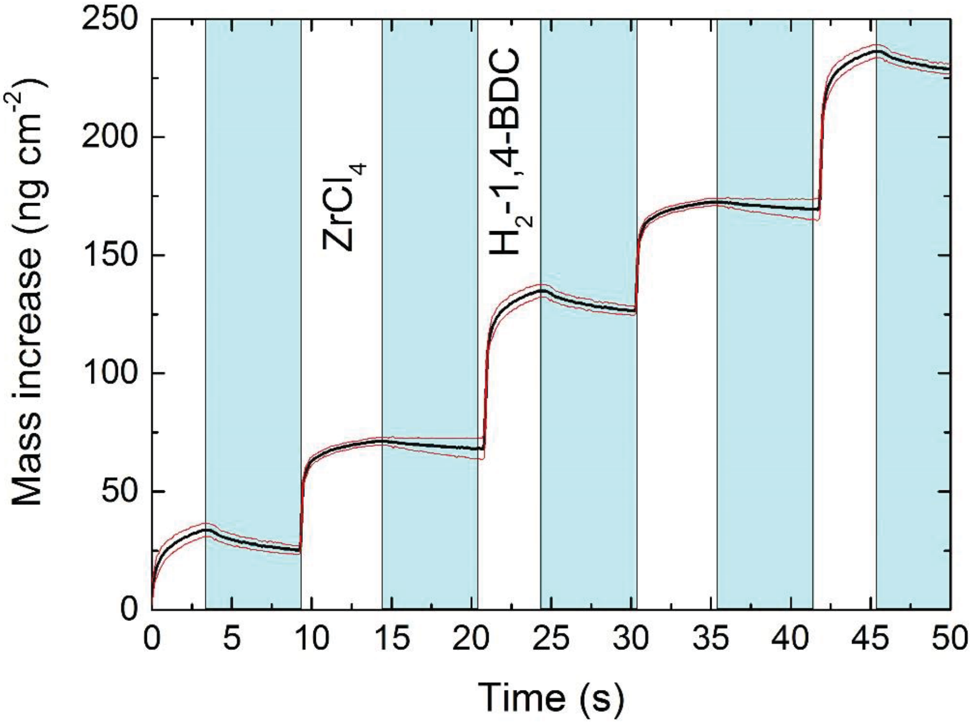

Figure 12: The mass increase as a function of time measured by QCM for the system where $ZrCl_4$ and H_2-1,4-BDC were used as precursors. The blue fields indicate purges, and the red lines show the standard deviation of the measurements (n=16). Adapted from Paper I.

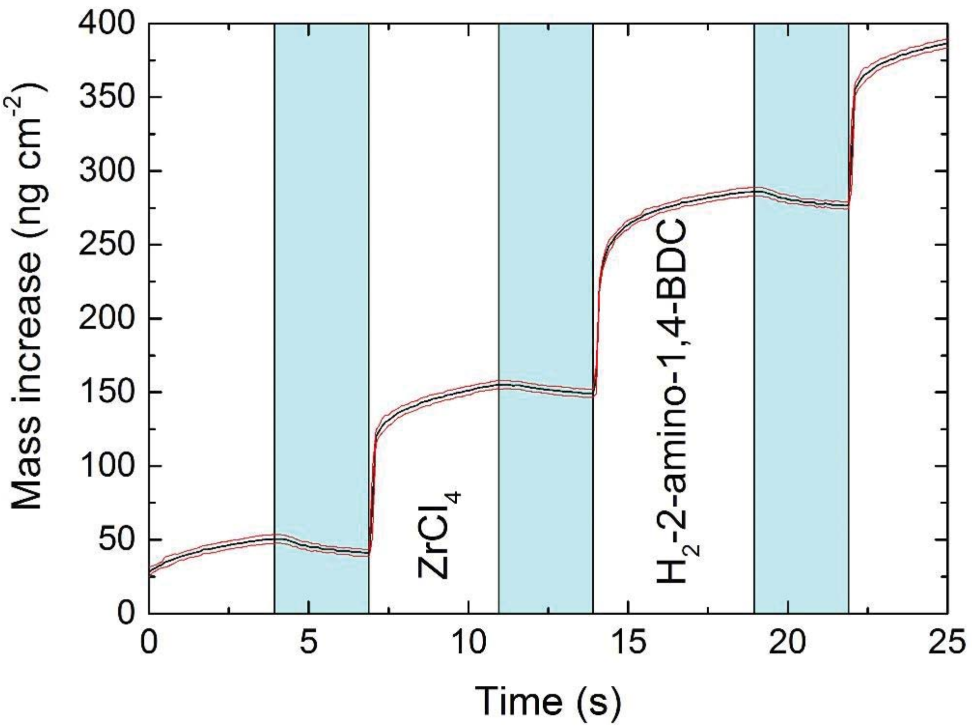

Figure 13: The mass increase as a function of time measured by QCM for the Zr-2-amino-1,4-BDC system. The blue fields indicate purges, and the red lines show the standard deviation of the measurements (n=16). Adapted from Paper II.

For the two systems above, QCM showed that saturation of both precursors occurred within 2-4 seconds. This was not the case for the Zr-2,6-NDC and Zr-BP-4,4'-DC systems, which required 20-second long pulses of the organic acids in order to reach saturation, and obtain an ALD-type growth, Figure 14.

One explanation for this slow saturation is that the vapor pressures of the larger organic acids are lower (the precursor temperatures for H_2-1,4-BDC, H_2-2,6-NDC, and H_2-BP-4,4'-DC were 220, 225, and 250 °C respectively). Another explanation is that the 2,6-NDC and BP-4,4'-DC linkers are bulkier than the 1,4-BDC linker, which causes reaction sites to be partially blocked, slowing down the reaction kinetics.

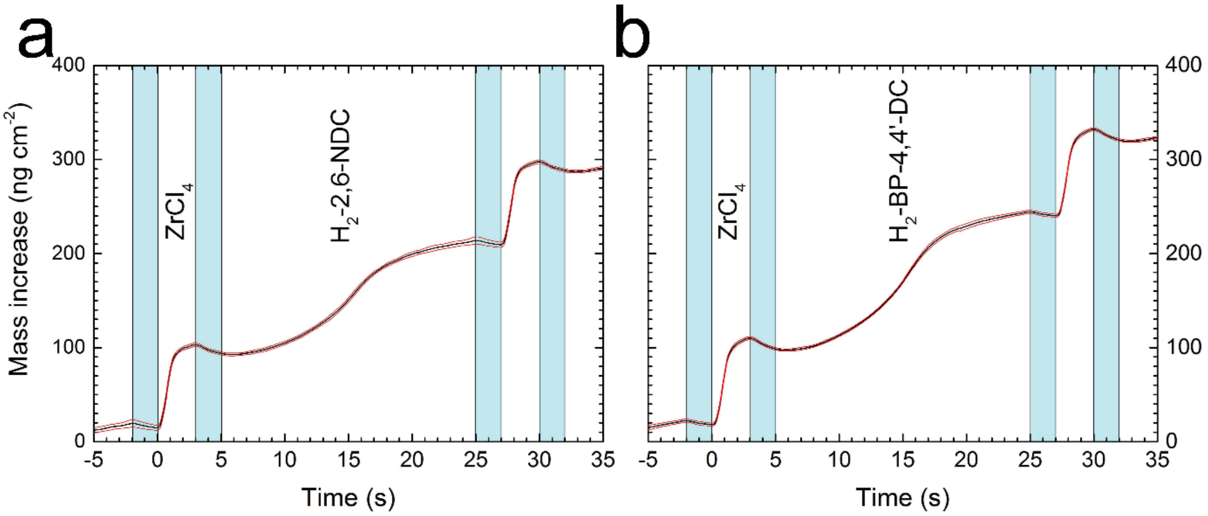

Figure 14: The mass increase as a function of time measured by QCM for (a) the Zr-2,6-NDC and (b) Zr-BP-4,4'-DC systems, taken from Paper III. The reaction temperature was 290 °C, and a pulse and purge sequence 3 s $ZrCl_4$ pulse, 2 s purge, 20 s acid pulse, and 2 s purge was used in both cases. The red lines show the standard deviation of the measurements (n=16).

Figure 15 shows the growth rate as a function of pulse and purge lengths in the Zr-2,6-NDC and Zr-BP-4,4-DC systems. From this figure, we can see a significant delay between the saturations of the QCM crystals in the back of the reaction chamber compared to the front crystal. This indicates that a low precursor dose due to low vapor pressures of the organic acids is the main factor behind the slow saturation that was observed.

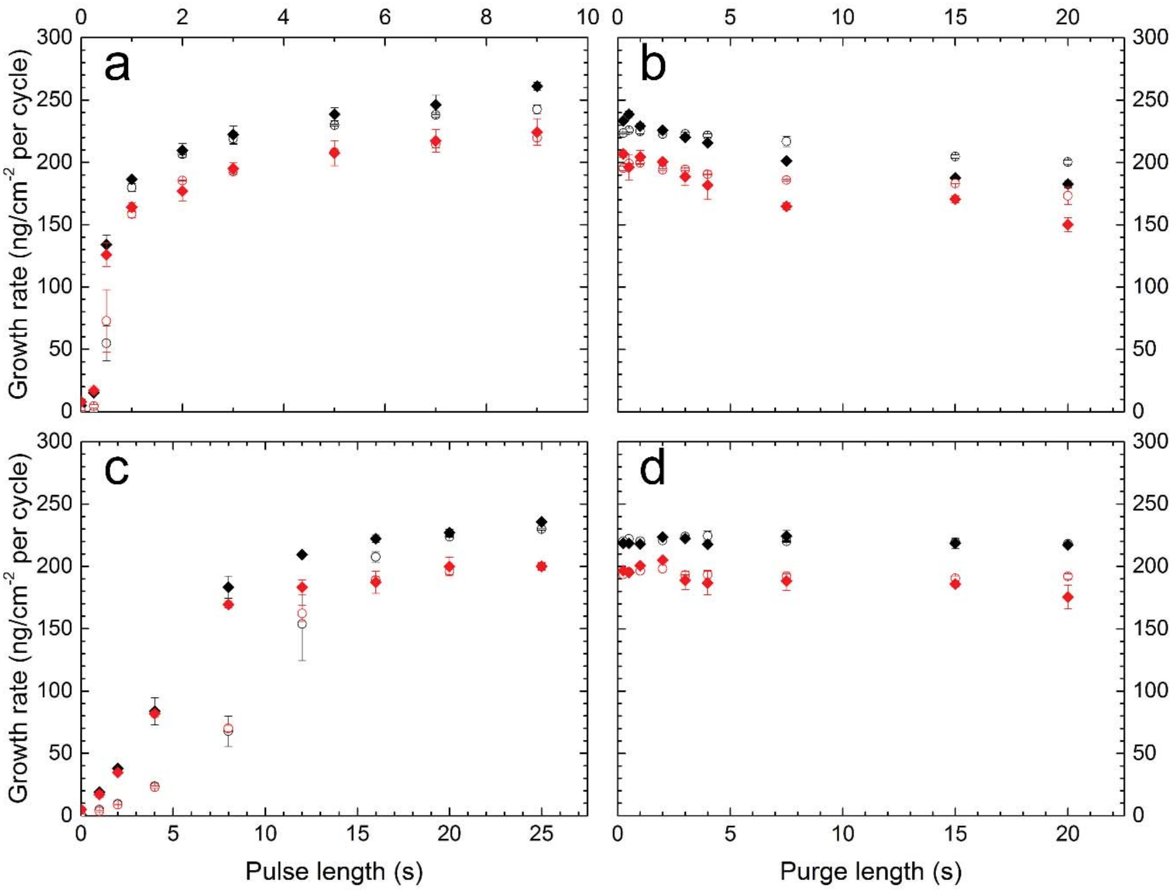

Figure 15: The growth rate as a function of pulse and purge lengths as measured by QCM for Zr-2,6-NDC (red) and Zr-BP-4,4'-DC (black). A standard pulsing sequence of 3 s $ZrCl_4$ pulse, 2 s purge, 20 s 2,6-NDC/BP-4,4'-DC pulse, and 2 s purge was used. The $ZrCl_4$ pulse length (a), the $ZrCl_4$ purge length (b), the organic acid pulse length (c), and the organic acid purge length (d) were varied individually. Two sensors were used, one in the front of the reaction chamber (solid diamonds) and one in the back (open circles), situated ca. 5 cm apart. All data points show the average of two replicates of the experiments, the error bars show the spread between them. Taken from Paper III.

Preliminary work has been carried out with bipyridine-5,5'-dicarbocylate (BPy-5,5'-DC) as linkers. This mostly includes *in situ* QCM characterizations of the growth rate as a function of pulse and purge lengths. As in the other MLD-systems, $ZrCl_4$ was sublimed at 165 °C. This was combined with H_2-BPy-5,5'-DC, which was heated to 225 °C. Figure 16 shows the QCM response normalized to the change in the response for the standard deposition sequence as a function of the pulse and purge lengths. The standard deposition sequence was in this case 3 s $ZrCl_4$ pulse, 2 s purge, 180 s H_2-BPy-5,5'-DC pulse, and 2 s purge. The data were normalized to account for a decreasing QCM response due to smoothening of the surface of the QCM crystal during the duration of the experiment. However, they have not yet been recalculated to a real mass change per area. A such normalization approach was standard procedure for all similar *in situ* QCM experiments in this thesis.

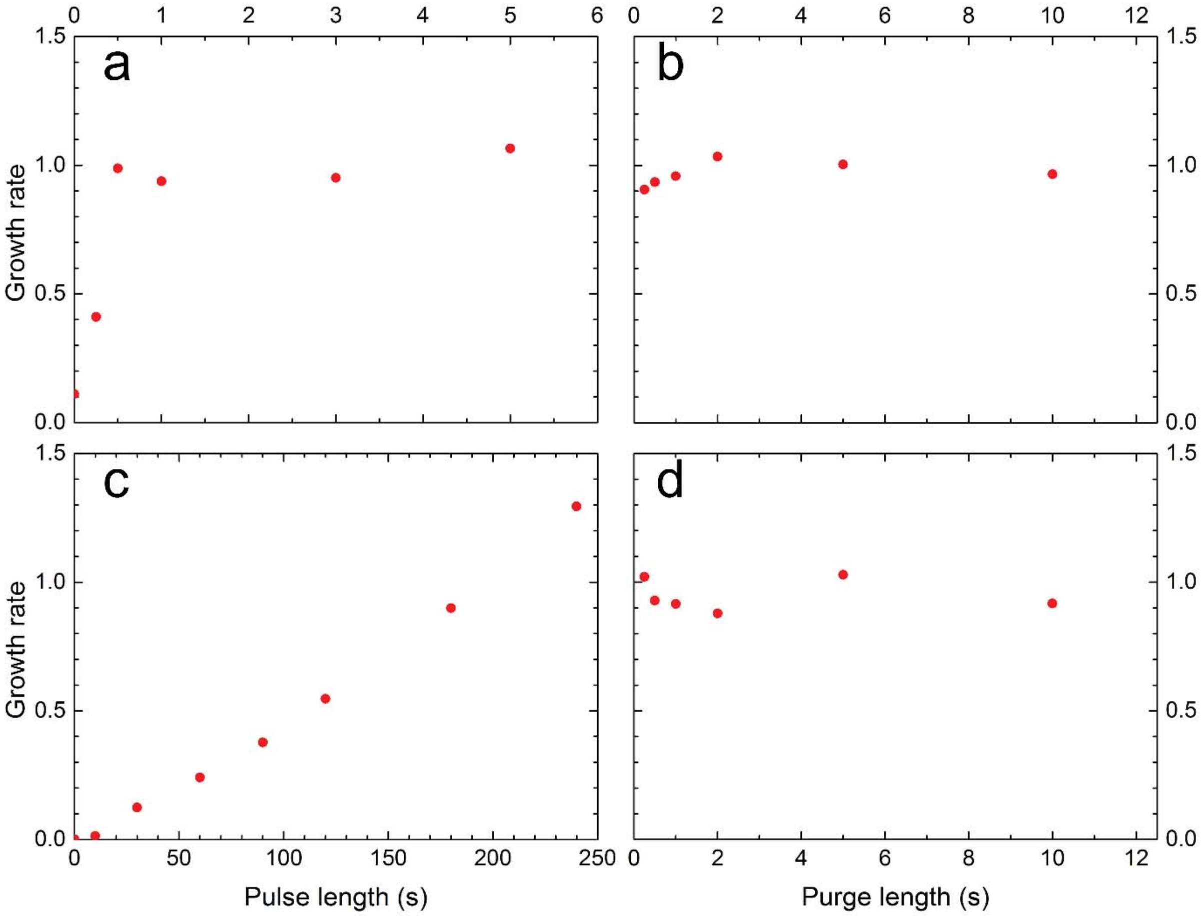

Figure 16: The growth rate (displayed as the response on the QCM crystals normalized to the standard deposition sequences) as a function of the (a) pulse length of $ZrCl_4$, (b) purge length after $ZrCl_4$, (c) pulse length of H_2-BPy-5,5'-DC, and (d) purge length after H_2-BPy-5,5'-DC.

From Figure 16c, we can see that the BPy-5,5'-DC linkers do not saturate the surface even after a four minute long pulse. This is probably because the vapor pressure of H_2- BPy-5,5'-DC is not sufficiently high when heated to 225 °C. A full saturation can possibly be reached with an even longer pulse or with a higher temperature on the precursor. The latter option is not trivial, since we observe that the precursor decomposes or polymerizes to form a yellowish white powder when heated for a long time (the fresh precursor is white). This degradation of the precursor occurs to a certain degree already when the sublimation temperature is 215 °C, but is likely be faster for higher temperatures.

5.2 Acetic Acid Modulation

Since the films were amorphous as-deposited, we investigated various means for crystallization by post treatment. Application of the same approach as described in the abovementioned work by Salmi et al.[128], i.e. exposure to moist air, did not lead to a crystalline MOF structure. For the Zr-1,4-BDC films, we rather obtained exsolution of H_2-1,4-BDC crystals on the surface. This led to the understanding that there was an excess amount of linker molecules present in these films. To avoid this excess amount of linker molecules, a modulation step was introduced to the deposition cycle by adding a pulse of acetic acid after the H_2-1,4-BDC pulse. Acetic acid has previously been used as a modulator to increase crystallization in wet based MOF synthesis[63]. This modulation approach works by allowing the modulator (acetic acid) to compete with the linker molecules for binding sites, causing linkers with a weak binding to be removed.

The result of modulation in the MLD process was no significant reduction in the overall growth rate, but a loss of the excess linkers, which could be seen by QCM as a decrease in mass, Figure 17.

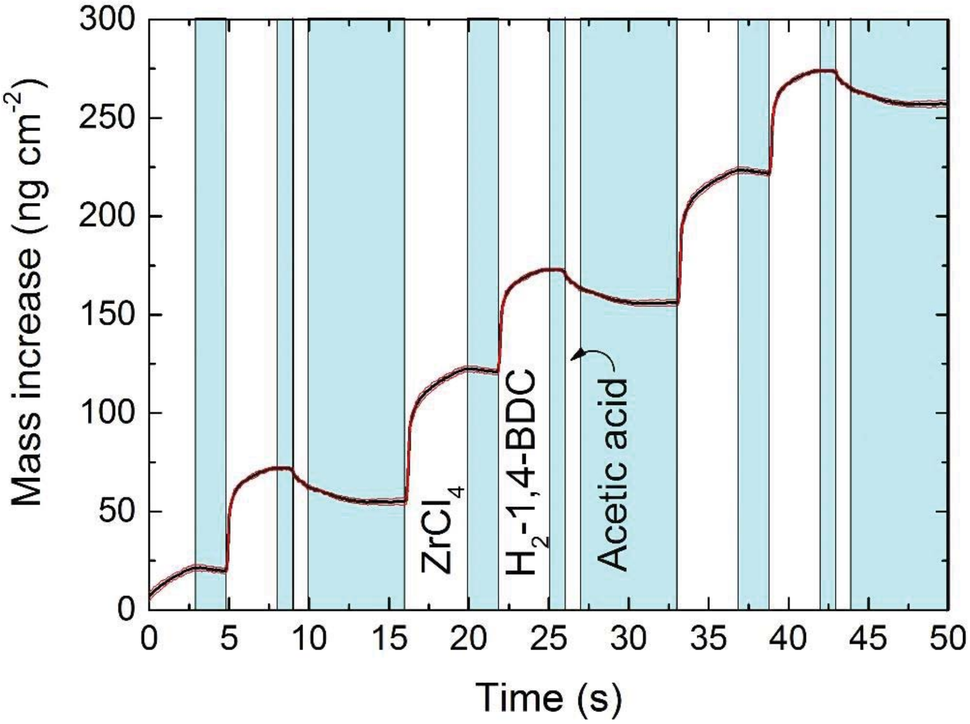

Figure 17: The mass increase (and decrease) as a function of time for the system where acetic acid modulation was introduced in addition to the $ZrCl_4$ and H_2-1,4-BDC precursors. The red lines show the standard deviation in the measurements (n=16). Adapted from Paper I.

The FTIR analyses shown in Figure 18 indicated that the excess amount of linker that was lost during the modulation mainly was the linkers with monodentate coordination to Zr. The mode of coordination was determined by noting the total splitting between peaks that correspond to the symmetric and asymmetric stretch in the carboxylate group. According to Verpoort et al.[152], this splitting is largest for monodentate coordination and smallest for bidentate coordination. Bridging coordination gives an intermediate splitting.

Introduction of the acetic acid modulator changed the bonding scheme of the 1,4-BDC linker from a monodentate to a bidentate bonding scheme. Subsequent attempts to crystallize the film by exposure to moisture did not result in exsolutions of ligand crystals, indicating that the modulated films no longer have an excess of linker molecules.

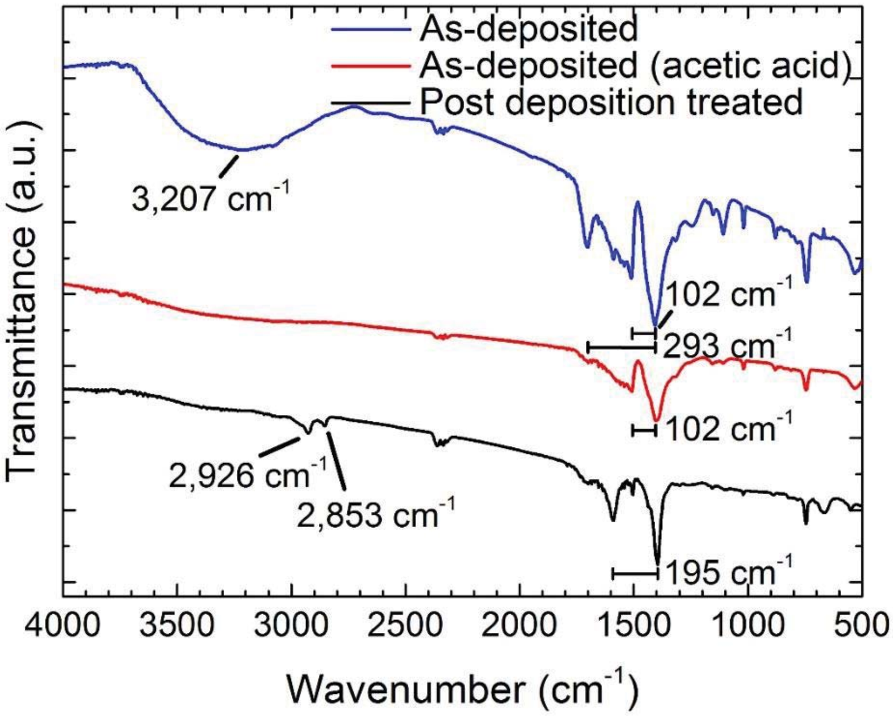

Figure 18: FTIR spectra for unmodulated films (blue), acetic acid modulated films (red), and crystallized films (black). The spectra show that monodentate coordination only occurs in the unmodulated films. Adapted from Paper I.

The behavior was quite different when acetic acid modulation was introduced in the Zr-2-amino-1,4-BDC system, Figure 19. There was no longer a mass loss corresponding to the loss of linkers with monodentate coordination to Zr during the acetic acid pulse. Instead, there was a small mass increase corresponding to physisorption of acetic acid, which was then mostly lost in the subsequent purge.

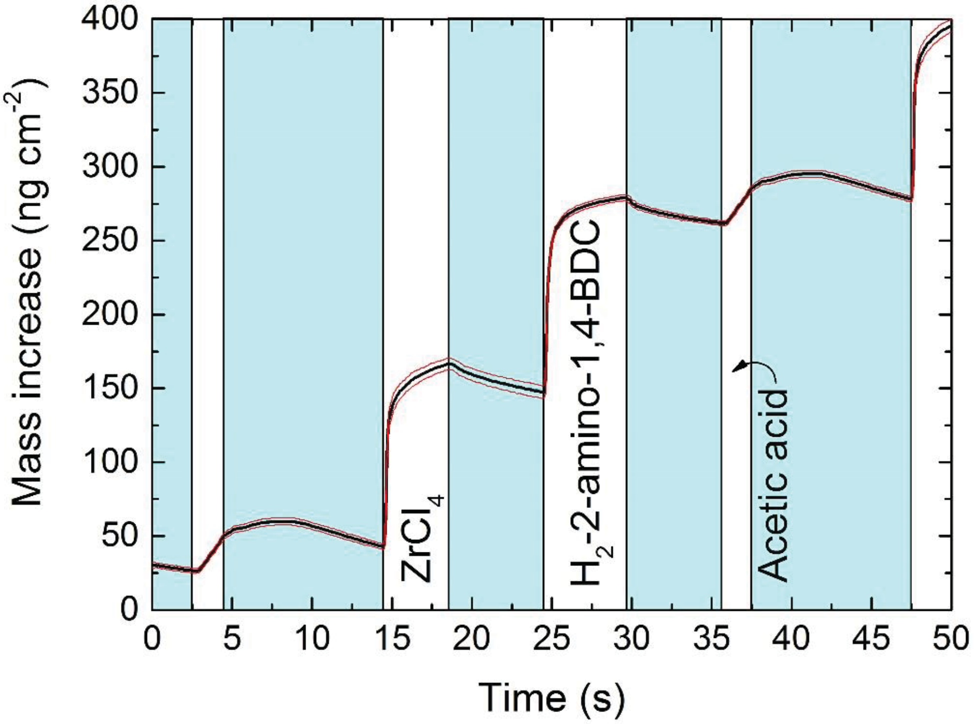

Figure 19: The mass increase as a function of time during the acetic acid modulated deposition where $ZrCl_4$ and H_2-2-amino-1,4-BDC were used as precursors. The red lines show the standard deviation in the measurements (n=16). Adapted from Paper II.

The fact that acetic acid modulation was less important for the Zr-2-amino-1,4-BDC system compared with the Zr-1,4-BDC system was further demonstrated by exposure of the amino-functionalized films to moist air. This no longer caused crystallization of excess linker molecules on the surface, regardless of whether the films were modulated or not. The reason why the modulation was not required in this case is the lack of monodentate coordination of the linker in these films as mentioned in chapter 5.1.

The Zr-2,6-NDC and Zr-BP-4,4’-DC systems showed different effects of the acetic acid modulation, where the Zr-2,6-NDC system was most similar to the amino-functionalized system, and the Zr-BP-4,4’-DC system was similar to the non-functionalized Zr-1,4-BDC system. Diffractograms obtained by GIXRD showed that films of these two systems deposited with or without modulation behaved differently in different environments, Figure 20.

For the Zr-2,6-NDC system, there was no exsolution of the organic acid upon exposure to moist air. However, when the samples were submerged in an aqueous solution of NaCl (0.9 wt%), a difference between modulated and unmodulated samples appeared. For the unmodulated samples, some

H_2-2,6-NDC crystallized on the surface, while this did not occur for the modulated sample. The lack of crystallized precursor on the modulated samples indicates that the modulation still plays a role in the formation of stronger bonds between Zr and the linkers, even though a monodentate coordination between these two could not be detected with FTIR (not shown).

In the Zr-BP-4,4'-DC system, GIXRD showed that a small amount of the H_2-BP-4,4'-DC precursor crystallized on the surface of the unmodulated films after exposure to moist air, while this did not happen for the modulated samples, Figure 20c. Similar to the Zr-2,6-NDC system, the crystallization of the organic acid on the unmodulated samples was much more significant when the sample was submerged in an aqueous solution of NaCl (0.9 wt%). However, unlike in the Zr-2,6-NDC system, this crystallization was not prevented by acetic acid modulation.

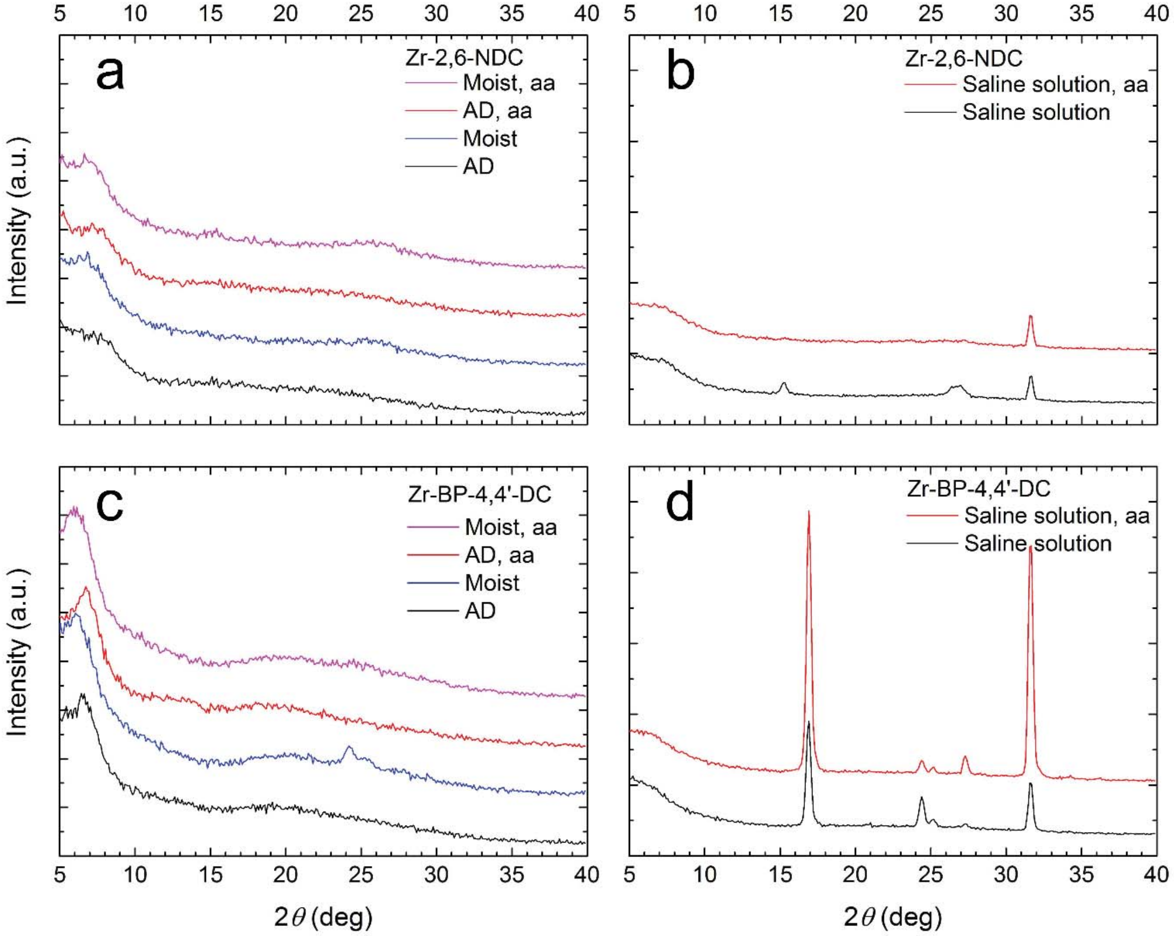

Figure 20: (a) and (c) show diffractograms by GIXRD for Zr-2,6-NDC films and Zr-BP-4,4'-DC films, respectively. As-deposited films (black and red) are compared films exposed to moist air (blue and magenta). Films deposited with (red and magenta) and without (blue and black) acetic acid modulation were tested. The effect of exposure to an aqueous solution of NaCl (0.9 wt%) is shown for Zr-2,6-NDC films (b) and Zr-BP-4,4'-DC films (d). Black indicates unmodulated films and red is films with acetic acid modulation. Taken from Paper III.

The discovery of the effects of acetic acid modulation is one of the important finding in this thesis. This gives information on the reaction kinetics in an MLD system where carboxylate groups have the opportunity to have monodentate, bidentate or bridging coordination to the metal atoms, and could potentially lead to more controlled growth of carboxylate-based hybrid films in the future. As mentioned above, the modulator competes with the linker for bonding sites, and guides the bonding of the linkers. In many ways, the modulator performs some of the same tasks as solvent molecules do in a solution, but they are able to do this in the gas phase. This can also affect crystallization as will be described in the next section.

5.3 Crystallization of MOF Thin Films

Although modulation of the deposition process was achieved, neither the process itself nor exposure to moist air gave crystalline MOF films. The search for a successful crystallization process continued with various autoclave-treatments of the films. Several combinations were explored for the Zr-1,4-BDC system, with water or DMF as solvents both with and without added acetic acid for modulation. Some attempts were also carried out with the same solvents, but with the sample suspended above rather than being immersed into the liquids. In addition, some attempts were performed with no solvent at all, and with only a few drops of the acetic acid modulator added. In all cases, the treatment was performed at 160 °C for 24 hours.

Although a selection of the combinations mentioned above gave a few reflections in the diffractograms obtained by GIXRD, none was as promising as the samples treated with only acetic acid. This treatment gave crystalline UiO-66 thin-films with the diffractogram that is shown in Figure 21.

Another evidence for the crystallinity of the films was found in the FTIR spectra shown in Figure 18. The spectrum for the crystalline film shows that the linkers bridge between two Zr atoms instead of being bonded monodentate or bidentate to one Zr atom. This bridging coordination is the same coordination as found for the linkers to the clusters in the UiO-66 structure[26].

Crystallization of the amino-functionalized films was done in the same way, by autoclave treatment at 160 °C for 24 hours in acetic acid vapor. This led to the formation of crystallites in the shape of hexagonal plates on the surface that are seen in the SEM images in Figure 22. This morphology is difficult to explain from the cubic crystal structure of UiO-66-NH_2. Therefore, it is likely that the formed crystal structure is similar to the hafnium UiO-67 nanosheets made by Cliffe et al.[153] or the hcp UiO-66 structure by Ermer et al.[154], which both have hexagonal symmetry.

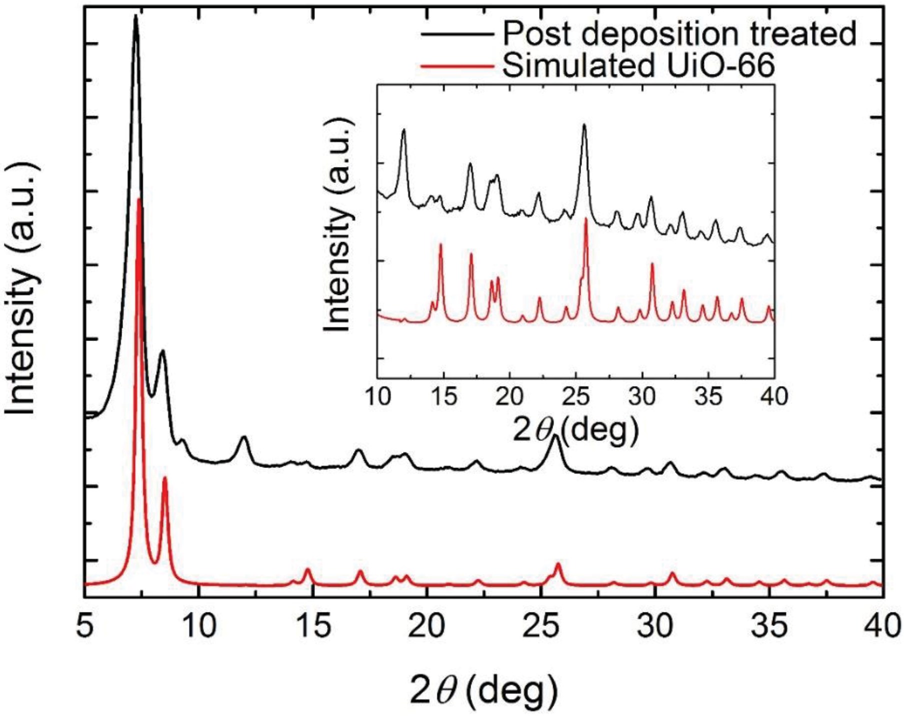

Figure 21: A diffractogram obtained by GIXRD for the UiO-66 film after autoclave-treatment in acetic acid vapor (black) compared to the simulated diffractogram for UiO-66 (red). Adapted from Paper I.

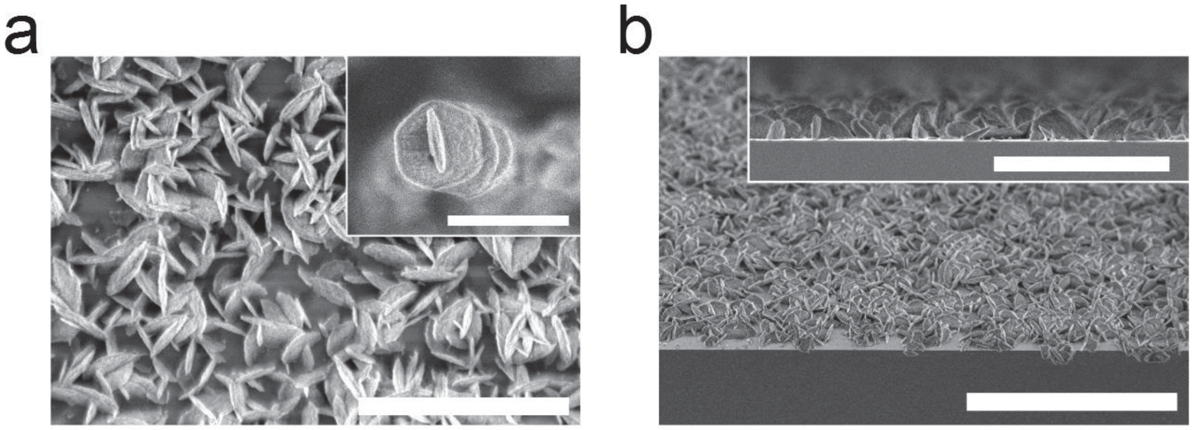

Figure 22: SEM images of the flat, hexagonal crystallites in the autoclave treated samples of Zr-2-amino-1,4-BDC. (a) A top down view with an enlarged view of one crystallite in the inset, scale bares are 2 µm and 1 µm, respectively. (b) A 45° angle cross section view with a 90° cross section view in the inset, with 5 µm and 2 µm scale bars, respectively.

For the Zr-2,6-NDC system, it is important to recognize that the same cluster geometry as present in UiO-66 combined with 2,6-NDC as a linker can lead to various MOF structures, such as DUT-52, DUT-53, and DUT-84[155] (DUT = Dresden University of Technology). The main difference between these structures is the connectivity of the linkers to the inorganic nodes. In DUT-52, the nodes are connected to 12 linkers, similar to UiO-66, whereas in DUT-53 and DUT-84, they are connected to eight and six linkers, respectively. In addition to this, it is possible to imagine clusters different from the UiO-66 structure. It is difficult to pinpoint which crystal structures were formed in the present study, and it may be a combination of different phases. However, it is clear from GIXRD shown in Figure 23 that the films are crystalline after autoclave treatment, and that the unit cells in the crystallites are large, indicating that MOF structures are formed.

Crystallization by autoclave treatment was possible also for the Zr-BP-4,4'-DC system. The diffractograms for two crystalline films of different thickness are given in Figure 23. There are indications of a small amount of crystalline UiO-67 in the films. However, this is in addition to a much larger amount of (at least) one other unknown phase. Again, this unknown phase has a large unit cell, like most MOF structures.

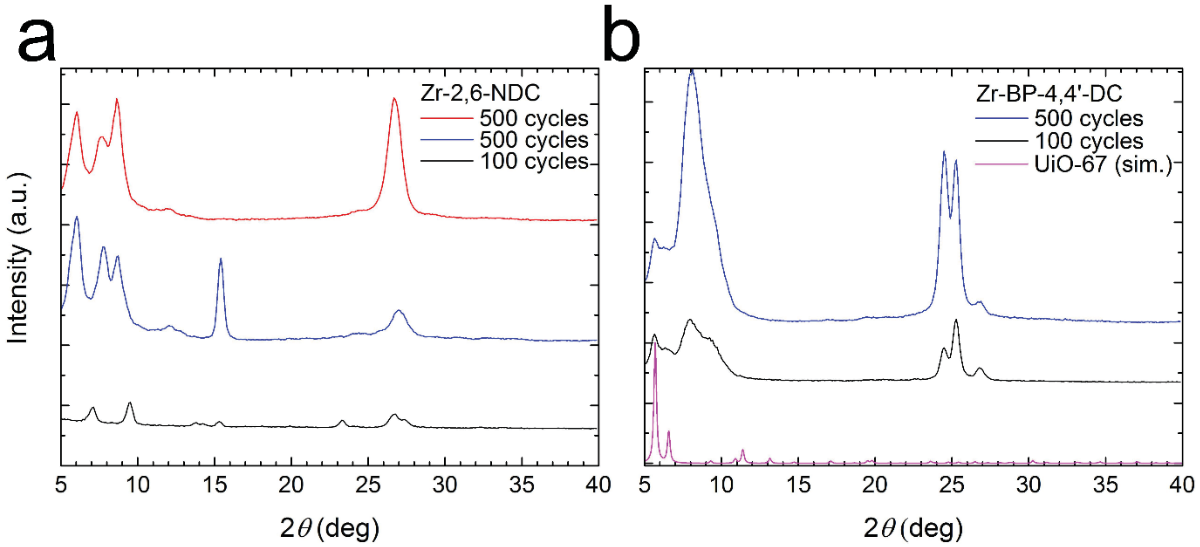

Figure 23: Diffractograms obtained by GIXRD for the Zr-2,6-NDC films (a) and the Zr-BP-4,4'-DC films (b). In (a), three crystallized films are shown, two that were deposited by 500 cycles (blue and red) and one deposited with 100 cycles (black). (b) Shows one film deposited with 500 cycles (blue), one deposited with 100 cycles (black) and a simulated diffractogram for UiO-67 (magenta). Adapted from Paper III.

Development of the crystallization procedure described above is another main achievement of this thesis. So far, it has led to highly crystalline films of UiO-66 and a phase closely related to UiO-66-NH_2. Discovery of some unknown phases and a small amount of what seems to be UiO-67 opens for the possibility of making several other MOF thin films by this technique. Through further optimization, pure UiO-67 films or perhaps thin-films of never before seen MOF phases may be possible. It is worth *mentioning that this crystallization step does not involve any solvents, and that the MOF structures thus have been made through an all-gas-phase technique.*

5.4 Porosity

Investigation of the porosity of the materials proved to be a challenge. Conventional methods for measuring the porosity of MOFs, such as determination of the internal surface area by the BET method[156] (BET = Brunauer-Emmett-Teller), were not possible due to the small amount of sample. Porosity measurements through ellipsometric porosimetry (EP) were also attempted. For this technique, SE is used to measure the refractive index of the material at different partial pressures of a solvent (such as water or toluene). The refractive index changes as the air in the pores in the material is replaced by solvent molecules, and from this, the total porosity and the pore size can be calculated. For the films that were measured with this technique, an indication of the porosity is seen. However, due to the high roughness of the crystallized films, it was difficult to achieve a good fit of the SE data, which in turn gives a high uncertainty in the EP results.

The solution was to demonstrate the porosity using QCM. For each film system, two QCM crystals were coated using 500 cycles of $ZrCl_4$ and the organic precursor. One of these crystals was then treated in an autoclave with acetic acid to crystallize the film, while the film on the other QCM crystal was left amorphous. Both crystals were placed back inside the ALD reactor under vacuum where they were exposed to a water pulse at room temperature. The mass uptake during this water pulse was recorded and compared to the mass uptake on uncoated QCM crystals during a similar water pulse. The mass uptake of the crystalline film was significantly larger than the uptake on the uncoated QCM crystals, up to three orders of magnitude higher. This behavior was used as a proof of porosity in the films, while exact surface areas were not possible to obtain. An example of a porosity test like this is shown in Figure 24.

Interestingly, the total mass uptake in the amorphous Zr-1,4-BDC film was approximately the same as in the crystalline UiO-66 film when the water pulse was sufficiently long. This indicates that the amorphous films are also porous, although with less accessible pores causing slower kinetics for water to get in and out of the pores. With a sufficiently long purge after the water pulse, all of the water left the structure. This indicates that the mass increase during the water pulse was not due to any reaction between water and the film, but rather adsorption of water on the internal surface area of the pores.

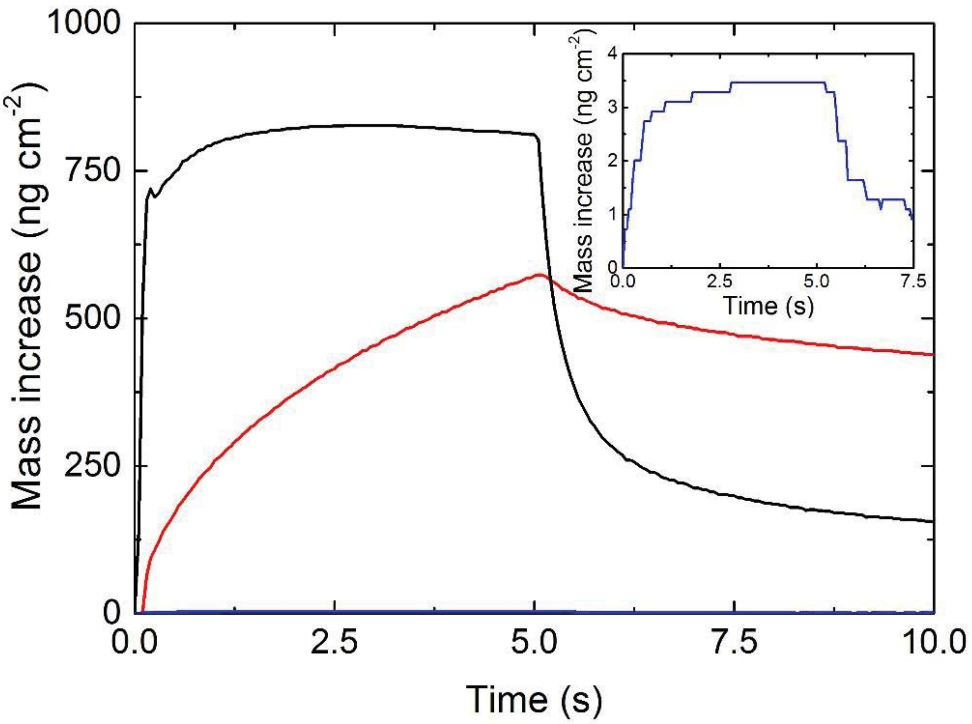

Figure 24: The mass increase during a 5 s long water pulse in a crystalline UiO-66 film (black), in an amorphous Zr-1,4-BDC film (red) and on uncoated QCM crystals as a control (blue) (expanded in inset) measured by QCM, adapted from Paper I.

The porosity measurements of the amino-functionalized films showed that the total porosity of the crystalline sample was about the same as for the non-functionalized UiO-66 film (see **Paper II**). It is worth mentioning that the saturation of the pores with water was much slower in these films, and that the total porosity of the amorphous films no longer was as high as the crystalline films. Both observations can be explained by partial pore blocking by the bulky amino group. Similar porosity tests were done for the Zr-2,6-NDC and Zr-BP-4,4'-DC systems, showing porosity for both amorphous and crystalline films (see **Paper III**).

Unfortunately, it was difficult to accurately determine the exact pore sizes in the films and determine a relation between the pore size and the linker length. However, the QCM porosity tests can give an indication of a difference in pore size if we compare the water uptake in the amorphous Zr-1,4-BDC, Zr-2,6-NDC, and Zr-BP-4,4'-DC films.

After a 42 s long water pulse, the amorphous Zr-1,4-BDC film was saturated with water. The total mass increase over that water pulse was 846 ng/cm^2. After an equally long water pulse over the amorphous Zr-2,6-NDC and Zr-BP-4,4'-DC films, the mass increases were 1831 and 2487 ng/cm^2, respectively. Saturation was reached for the two latter films after more than 60 s with uptakes of more than 2000 and 2700 ng/cm^2, respectively.

The mass increases in of all three films mentioned above are shown in Figure 25 for a 60 second long water pulse. It should be noted that the Zr-2,6-NDC and Zr-BP-4,4’-DC films were not completely saturated after 60 s, but still it is clear that the QCM response increased with increasing linker length.

In all cases, the films were deposited with 500 cycles with the aim of achieving a similar magnitude of clusters and pores. However, the amount of film formed will be affected by internal differences in growth rates and growth dynamics leading to variations in numbers of pores formed. In the parameter space available for such comparisons, we chose to focus on equal number of cycles when deposited at a desired temperature for each system. Within these variations we claim that the main reason for the increased response in the Zr-2,6-NDC and Zr-BP-4,4’-DC films compared to the Zr-1,4-BDC film is likely to be a larger total pore volume in films with longer linkers. This is also expected, since increasing pore size is found in isoreticular MOF structures with increasing linker lengths[38].

We have chosen to compare the amorphous films in this case because it eliminates some uncertainties that are present for the crystalline films such as different degrees of crystallization, variations in topography, *et cetera*.

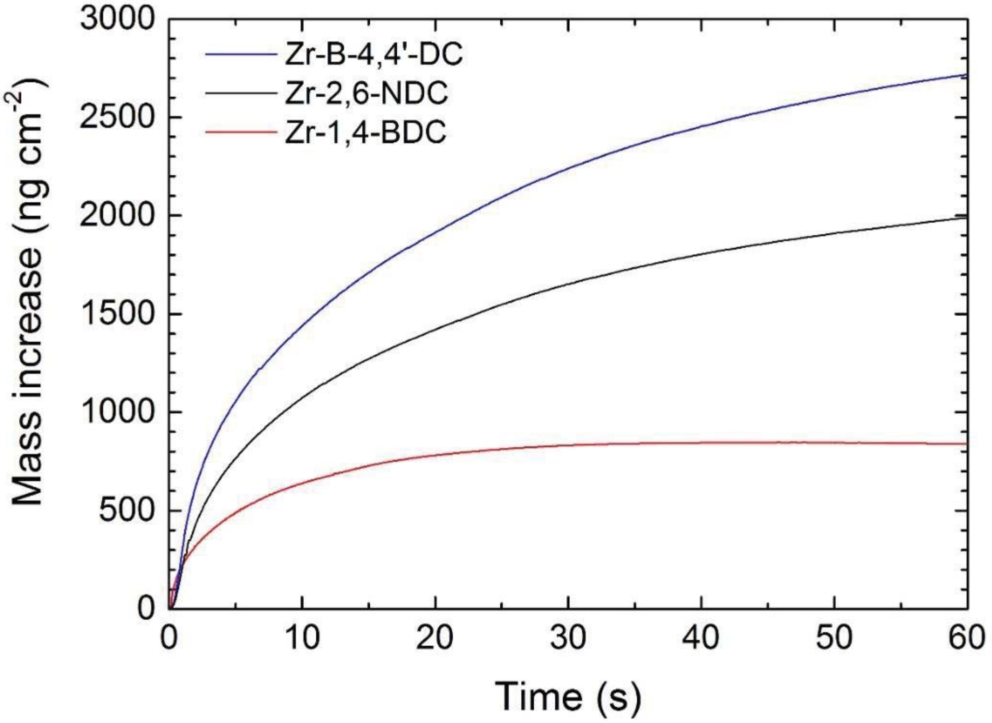

Figure 25: A comparison between the mass increases in the Zr-1,4-BDC, Zr-2,6-NDC, and Zr-BP-4,4’-DC films due to water uptake during a 60 s long water pulse, adapted from Paper III.

Measuring porosity with QCM was a pragmatic approach that proved useful for demonstrating the presence of porosity. This approach can be useful also in later studies where conventional measuring techniques are challenging. Further development of this technique may also enable a more precise modeling of the pore size from these measurements.

One of the most important discoveries from these porosity measurements is that the amorphous films are highly porous; in fact, they are equally porous as the crystalline films in some cases. These amorphous films are simpler to make since they do not need a post deposition treatment, and, as seen from the SEM images in Figure 26, they are flat and seemingly pinhole-free. This may be an advantage for several applications such as membranes.

Another important take-away from these measurements is that they serve as a proof-of-concept for increased sensitivity of sensors by using porous MOF films. The sensors in this case are the QCM crystals, which in some cases had a response to a water pulse that was three orders of magnitude higher when MOF films were added.

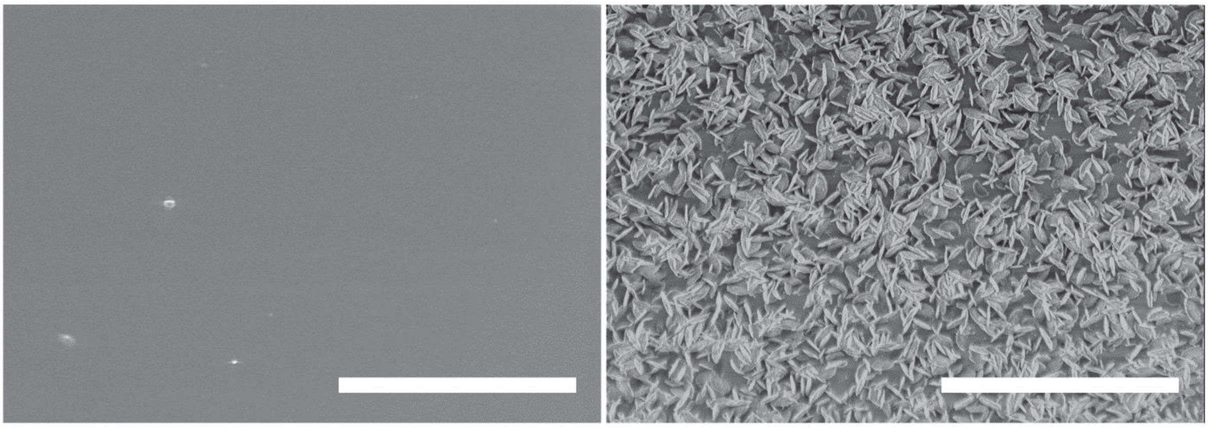

Figure 26: SEM images of an amorphous film (left) and a crystalline film (right). The difference in topology is exemplified by the Zr-2-amino-1,4-BDC system. The scale bars are 5 µm long.

5.5 Potential Applications

A few experiments have been performed to demonstrate possible applications for the porous hybrid films. Some of these attempts are mentioned in the sections below. None of the applications are fully optimized, but some can be promising with further development.

5.6.1 Separation Membranes

Attempts were made to make membranes for gas separations using the amorphous films. The attempts were carried out in a few different ways, including one attempt that will be described here. The internal surface area of a porous support structure was coated with amorphous 1,4-BDC films that filled the pores in this structure. The support structure was made to form a porous plug in a fused silica capillary tube. Before the MLD deposition, the pore size of the plug was in the μm range, and after the deposition, the pores were filled with Zr-1,4-BDC, which has a much smaller pore size.

Unfortunately, the films had a tendency to rupture when pressure was applied in order to push water through the pores in the Zr-1,4-BDC film. This led to the idea that films with higher hydrophilicity or slightly larger pores could enable water to pass through the membranes more easily. This is part of the reason for the studies that were done with H_2-2-amino-1,4-BDC, H_2-2,6-NDC, H_2-BP-4,4’-DC, and H_2-BPy-5,5’-DC as precursors. These systems have yet to be tested as separation membranes.

5.6.2 Luminescent Sensors

It is well known that several MOFs have luminescent properties[4]. This is also the case for the MOF thin films presented in this thesis. The combination of luminescence and the microporous structure of MOFs, make the thin films made in this work potentially applicable as sensors, if the luminescence is affected by interactions with a target molecule. The high internal surface area and the well-defined porosity open for both high sensitivity and selectivity.

The luminescent properties were measured for the Zr-1,4-BDC, Zr-2-amino-1,4-BDC, Zr-2,6-NDC, and Zr-BP-4,4’-DC films, and are displayed for the two latter in Figures 27 and 28. Photoluminescence excitation spectra was also measured and are shown for these films in Figure 27 b and d along with UV absorbance modeled from SE data.

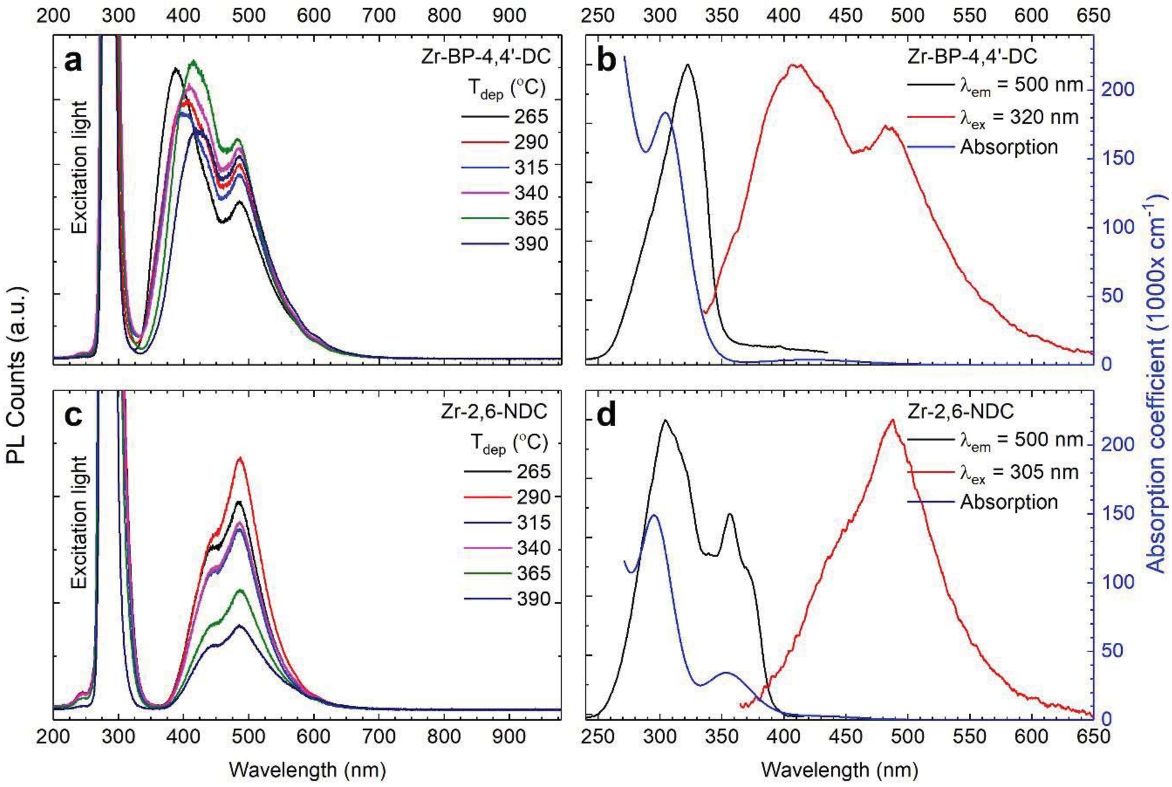

Figure 27: (a) And (c): photoluminescence (PL) counts as a function of wavelength for as-deposited Zr-BP-4,4'-DC and Zr-2,6-NDC films, respectively. The films were deposited at various temperatures. (b) And (d): the optical absorption (blue) modelled from ellipsometry data, excitation (black) and luminescence (red) data of the same films deposited at 290 °C. Taken from Paper III.

These measurements show that the emission spectra contain two maxima, one at 485 nm, which is seen in all films, and one at various wavelengths depending on the linker molecules. The fixed maximum probably originates from the Zr-clusters that are present in all films, while the others are likely to originate from the various organic linkers, since their positions change with the aromatic absorption of the linkers. The two types of luminescence may interact differently with exposure to various substances, which may be an advantage for use as sensor material since the unaffected one could function as internal standard.

For the Zr-BP-4,4'-DC, we observed a shift of the maximum associated with the aromatic structure when the deposition temperature was varied. A similar variation was not observed for the Zr-2,6-NDC films. This may be connected with the coordination between the linkers and Zr atoms and is further discussed in **Paper III**. The luminescence also bleaches upon exposure to UV light over time. This bleaching is different for the maxima from the clusters compared to the maxima from the aromatic structures and is also discussed further in **Paper III**.

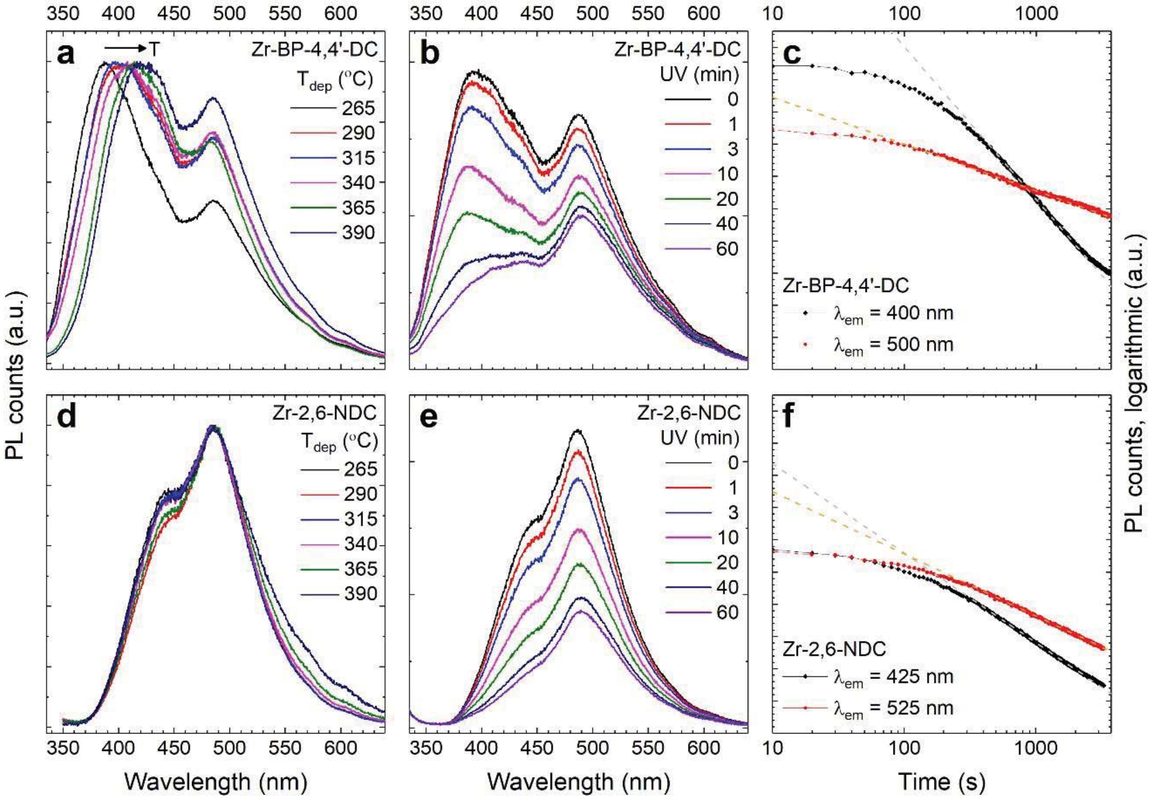

Figure 28: (a) And (d): normalized emission spectra from Zr-BP-4,4'-DC and Zr-2,6-NDC films. (b) And (e): the time evolution of these spectra upon UV exposure. (c) And (f): the evolution of the emission peaks from the aromatic linkers and zirconium cluster upon UV exposure. Taken from Paper III.

The films remain to be tested as sensors, but the properties that have been found are promising as long as a change in the luminescence associated with interactions between the films and measurable species can be found. Such effects are quite probable since luminescence often is sensitive to possible quenching routes, but it remains to be seen what will cause this quenching, and how selective this is toward various species.

5.6.3 Antibacterial Surfaces

A few examples of antibacterial effects of MOFs exist in the literature[5]. This property is very suitable for incorporation in thin-films as antibacterial coatings. Most examples in literature exploit a gradual degradation of the MOF to release metal ions or linkers with antibacterial effects [5, 157]. However, due to the UV-absorbance that was observed for the Zr-2,6-NDC and Zr-BP-4,4'-DC films, we decided to explore photo toxicity as the antibacterial mechanism. In **Paper III**, we discuss the antibacterial properties of these films with and without UV-irradiation. The Zr-BP-4,4'-DC films show no antibacterial effect, whereas the Zr-2,6-NDC reduce the number of viable bacteria by half compared to the uncoated cover glass controls when irradiated by UV light. This is explained by the absorbance spectra of the two films (seen in Figure 27) and the emission spectrum of the lamp that was used (shown in the article by Bergh et al.[158]). The absorbance spectrum for the Zr-2,6-NDC films overlap with the emission spectrum from the lamp for wavelengths between 350 and 400 nm, while the Zr-BP-4,4'-DC films do not absorb any of the light emitted by the lamp.

Since the Zr-2,6-NDC films showed antibacterial properties, a further investigation with three independent experiment was performed, Figure 29. It was found that the irradiated Zr-2,6-NDC films were significantly different from all other samples that were tested (marked by * in the figure).

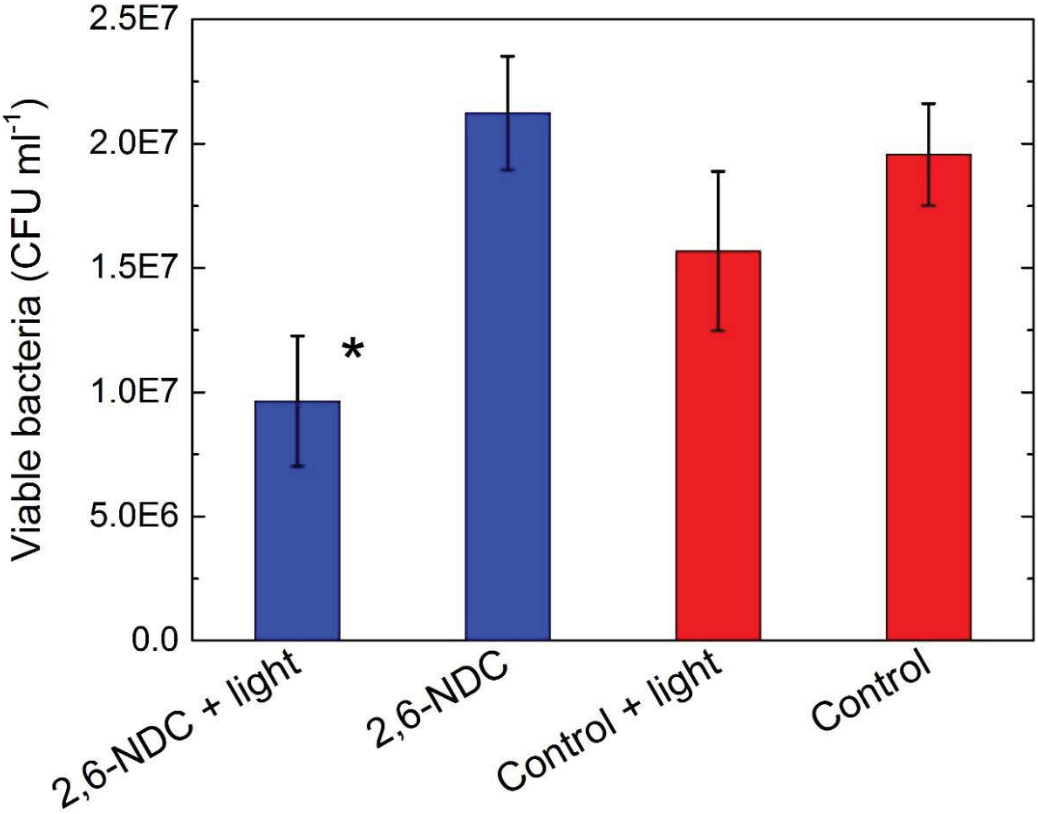

Figure 29: Viable bacteria measured as the number of colony forming units (CFU) per mL for the Zr-2,6-NDC films (blue) and controls (red), (n=3).

It is interesting to note that the antibacterial effect of the irradiated Zr-2,6-NDC films was significantly better than the controls, even though the overlap between the emitted light from the lamp and the absorption spectrum of these films is quite small. This paves the way for developing even more effective antibacterial MOF coatings when linkers with a larger overlap between their absorbance and the spectrum of UV-light emitted by the lamp are chosen. One possible candidate for such linkers, is the 2-amino-1,4-BDC linker that was used in **Paper II**. This linkers absorbance spectrum[159] should have a larger overlap with the emission spectrum from the lamp that was used. By also combining the photo toxicity described here and the well-known release of metal ions from Ag-, Cu-, Co-, or Zn-based MOFs[5], very effective antibacterial coatings could be made.

5.7 Context

The fields of MOF thin film synthesis and MLD of hybrid materials are expanding, and are currently merging into a new branch of research. This is an exciting development that both opens for fundamental research of reactivity between organic molecules and inorganic material without the influence of solvents, while also being application oriented. The combined MOF-MLD field is still very small, but with a potential to grow in the coming years. The work presented in this thesis falls into this category and joins the few prior works that have been mentioned earlier. These include the MOF-5[128] and IRMOF-8[129] films made by Salmi et al., and the copper(II)terephthalate[130] and iron terephthalate[131] MOF films made by Karppinen and coworkers. In addition, other crystalline coordination polymer films[134-136] that are closely related to MOFs have been made. The MOF-MLD field also includes some studies that attempt to implement these MOF films into devices. Most relevant to this thesis is the work presented by Lan et al.[160] They have used the synthesis method presented by us in **Paper I** to coat solid-phase microextraction arrows with a UiO-66 coating. The UiO-66 coating on the arrows was reported to have a comparable or better extraction efficiency and selectivity than commercial coatings, towards most polar compounds.

The advantages that these MOF-MLD synthesis methods have over other MOF thin film synthesis techniques come from the properties of MLD (or ALD) and include the ability to form conformal films with exceptional thickness control even on complex substrates. Some of these advantages can also be exploited by using an ALD grown film as a precursor layer for the MOF or as a nucleation film for regular MOF synthesis. The synthesis of ZIF-8 films by Stassen et al.[137], which was done by allowing an oxide film made by conventional ALD to react with the vapor of the linker molecules, is an example of the precursor layer approach. This synthesis method is very closely related to MOF-MLD, the only difference is that the organic precursor was incorporated into the film in a subsequent reaction instead of being a part of the ALD cycle. Nucleation layers for MOF growth made by ALD have been demonstrated by Zhao et al.[161] and Lee et al.[17], who have covered fibers and fabrics with UiO-type MOFs for degradation of chemical warfare agents. The MOF films that nucleate on the ALD grown thin films can cover complex substrates in a quite conformal manner. However, they lose some of the thickness control compared to ALD or MLD since the MOFs are grown by solvothermal synthesis.

If we look past MLD or ALD as synthesis methods for MOF films, a few other works should be mentioned. Most relevant for this thesis are the various synthesis methods for UiO-type MOF thin films. The electrochemical approach by Stassen et al.[78] is worth mentioning. They synthesized UiO-66 by immersing Zr metal electrodes in a solution of DMF, nitric acid, water and acetic acid, with dissolved H_2-1,4-BDC. They then heated the solution and applied a voltage between the electrodes to achieve MOF film growth. The work by Miyamoto et al.[63] is also of interest. They synthesize UiO-66 films by solvothermal synthesis, and are able to achieve highly oriented films when modulation was performed with a combination of acetic acid and water. Electrophoretic deposition of MOF particles demonstrated by Hod et al.[162], is another approach that has been used to make UiO-66 films. In this case, premade UiO-66 particles were dispersed in toluene and deposited on a positively charged electrode when an electric field was applied. This deposition occurs due to a negative charge in the MOFs that come from surface defects.

The abovementioned studies show that UiO-66 thin films can be prepared in various ways, but all of these works rely on liquid phase techniques. The only solvent free technique for making UiO-66 until now is through mechanochemical synthesis[163], which can be used to make bulk powders of UiO-66. The work in this thesis, and the rest of the MOF-MLD synthesis field mentioned above provides new possibilities for solvent free synthesis of MOFs and even solvent free synthesis of MOF thin films. This could be an advantage if MOF thin films are to be used in microelectronics with delicate features.

6. Conclusion and Future Outlook

This chapter will focus on the most notable achievements of the work in this thesis, and suggest a path forward with further research that could lead to thin films of other MOF structures and applications for MOF films.

Perhaps the most notable achievement in this project is the development of an all-gas-phase technique for synthesis of crystalline MOFs, which was an important aim of the study. All-gas-phase syntheses of MOFs have been demonstrated in only a few other cases[130, 137], most recently for an iron terephthalate with a MOF-2-like structure[131]. However, until now this has not been possible for highly stable MOFs such as the relatively complex UiO-66 structure. In this work, a few different MOF structures have been synthesized as crystalline thin films in an all-gas-phase manner. These include UiO-66; a structure closely related to UiO-66-NH_2; a small amount of what seems to be UiO-67; and a few unknown phases that are related to UiO-67 and the DUT-series of MOFs where 2,6-NDC is the linker.

Thin films of these MOFs are promising for a number of applications, but there is still work to be done to achieve these. Until now, only two prepared films are reasonably phase pure (UiO-66 and the UiO-66-NH_2-like structure), while the others seem to incorporate several MOF phases. We believe that continued efforts in mapping crystallization behavior of such films can open for single-phase films and probably new MOF structures. Further studies should include tuning of experimental parameters during the crystallization step such as temperature, duration, amount of modulator, and types of modulators. Acetic acid may not be the ideal modulator for structures with larger pores than UiO-66. Other organic acids that match alternative pore sizes and shapes should be tested in the crystallization step. In this way, the modulator can both fill the pore volume and act as a template molecule while at the same time compete with the linker molecules for binding sites. Some work has already been carried out by Lan et al.[160] to optimize the crystallization step from **Paper I** in order to make UiO-66 thin films for their applications, more systematic work such as this is needed.

In addition, there is more room for exploration of synthesis routes where the crystallization occurs in the ALD reactor instead of in a post-deposition autoclave treatment. If this were achieved, the deposition of crystalline MOF films would be more streamlined, and perhaps more attractive for implementation in devises. An attempt has already been made to replicate the autoclave conditions (temperature, acetic acid vapor and some moisture, but not elevated pressure) in the ALD reactor, directly after deposition. Unfortunately, this attempt did not lead to crystalline films. However, the parameter space is large and further attempts may be successful, particularly with more insight into the crystallization process inside the autoclave.

Another important discovery in this work is that the amorphous as-deposited films are highly porous. This has typically not been observed for other hybrid films, but was seen for all of the Zr hybrid films presented in this thesis (apart from Zr-BPy-5,5'-DC, which has yet to be tested for porosity). It would be interesting to investigate whether this is also true for the large range of other hybrid films that have been produced by MLD but have not been characterized with respect to porosity. The observation of porosity in the amorphous films is very promising for applications such as membranes, since the as-deposited films are flat, very conformal, and seemingly pinhole-free. With proper support they may also withstand the higher pressures required for filters and membranes. Should this be achieved, membranes for gas or liquid separations could be within reach.

The amorphous thin films could also be useful for many of the other applications that have been proposed for MOF thin films, including drug delivery, sensor technology, low-κ materials for microelectronics and possibly several other. However, there is still a lot of work to be done with exploring such applications.

Acetic acid modulation during the MLD deposition is a third significant achievement in this thesis. This has enabled control of the coordination mode between the linker molecules and the metal atoms. We have also observed that the stability of the films can be improved by this modulation, since exsolution of the linker molecules in some cases no longer occurs for films that have been deposited with acetic acid modulation. This is an important discovery if the films are to be used in moist or wet environments. A modulation step like this could potentially be useful also in other similar MLD processes. Although the modulation procedure has been introduced here, further studies are needed, including *in situ* FTIR measurements that could shed light on the role that acetic acid plays in the deposition. This also applies to expansion of the modulation process with alternative reactants and MLD processes. A natural continuation is to investigate effects of carboxylic acids with varying carbon chain lengths or with aromatic moieties such as benzoic acid to match the desired pore size, as mentioned above.

Further work should also be carried out with BPy-5,5'-DC as a linker to open for MOF thin films that can be further functionalized. One possible approach could be co-pulsing of BP-4,4'-DC with BPy-5,5'-DC, which could give a UiO-67 MOF with some BPy-5,5'-DC linkers where metal complexes can be attached. Co-pulsing of linkers could also be interesting for mixing in various amounts of 2-amino-1,4-BDC into the UiO-66 structure. This could lead to formation of new crystal structures, and a tuneability of properties such as hydrophilicity.

The techniques developed in this work present several interesting topics for further research beyond the UiO-series of MOFs. This work has shown that it is possible to form some of the complex metal clusters that are found in many MOFs through the gas phase in addition to more simple clusters with one or two metal atoms. Depositing MOFs with complex clusters from other metals than zirconium could be possible, and should be attempted. The field of ALD provides precursors for most elements in the periodic table. These can be combined with rigid organic molecules such as the ones that are typically used as MOF linkers in order to deposit hybrid film and potentially other MOF structures. Many such hybrid films have already been made, for instance films containing aluminum[125-127] or zinc[128, 129], in combination with carboxylic acid linkers. It would be very interesting to attempt our modulation and crystallization technique on these systems.

The range of possibilities in choice of linker molecules for implementation in MOF-MLD is vast. To map their suitability, determination of their sublimation temperatures is a good start. Some molecules will have a sufficiently low sublimation temperature, while others will decompose or polymerize before they reach a sufficient vapor pressure. This is especially true if the linker molecules are large and complex, or if they have two or more functional groups that can react with each other at elevated temperatures. For instance, a linker with both a carboxylic acid and an amino group can polymerize by forming peptide bonds, although we know from **Paper II** that this combination of functional groups will not always be a problem.

Where the linkers of a known MOF structure show promising sublimation behavior, it is tempting to try a direct implementation into an MLD process in combination with an appropriate metal precursor. A scan of the presently known MOF structures shows a large range of probable combinations where some are already tested and resulted in amorphous films, a few are crystalline, while others remain untested. However, if decomposition or polymerization of the organic linker prevents direct reaction, there may still be ways around this problem. For instance, if a long and complex linker such as the one used in IRMOF-74-XI (shown in the bottom of Figure 3) is needed, sublimation will probably not be possible. In this case, one could try to construct a similar, long linker by building the linker through the gas phase in an MLD manner, provided that the chemistry is possible. One such chemistry to exploit is ring opening reactions in MLD[164]. An advantage of this approach is that a ring structure with for instance one carboxylic acid group can be used, which lowers the sublimation temperature of the organic precursor compared to one with multiple functional groups. This ring is then broken apart to form new functional groups for instance by using ozone. In this way or through other chemistries, the complex MOF linkers could be synthesized directly in the film. A completely different solution could be to alter the linkers that do not sublime by substituting fluorine for some hydrogen atoms. This may lower the sublimation temperature by reducing the intermolecular forces, but will also alter some of the functionality of the linker.

When completely new systems like these are investigated, the possibilities with choice of metal precursor (controlling reaction rates and by-products), modulator (reactivity and shape), and reactive sites on organic linker (alcohol vs. ether, carboxylic acid vs. acid anhydride vs. ester), lead to numerous possible permutations.

In other words, there are many possibilities to advance this work further, and to develop more in the field of MOF-MLD. Nevertheless, we should be aware of a few possible limitations. As indicated above, not all MOF linkers can be volatilized, and can therefore not be used in MLD. In addition, there needs to be a balance in temperatures in the MLD system. If a high temperature is needed in order to sublime the linkers, an even higher reaction temperature must be used in order to avoid condensation of the linker. This sets a certain demand on the bond strength between the metal and the linker in the MOF, since this bond strength must be sufficiently high to survive the high reaction temperature. However, even with these limitations, there should be many MOFs that are promising candidates for MOF-MLD.

Combining the experience from other groups that work on MOF-MLD and related techniques with our approach is also important as it could improve depositions of MOFs that have already been made such as MOF-5 or ZIF-8, or enable all-gas-phase depositions of thin films of other iconic MOF structures such as HKUST-1.

In accordance with the aim of the study, a few applications have been tested for the MOF films that were made. Some of these are promising and should be further developed. In particular, the possibility to combine porous structures with luminescent properties open for sensor materials with high sensitivity and hopefully increased selectivity. In addition, the combination of optically active structures and materials providing antibacterial surfaces open for possibilities within photocatalysis. However, this requires further studies to elucidate the mechanism of activation.

The work in this thesis is summarized in Figure 30 by a graphic showing the MLD cycle for $ZrCl_4$ and the various organic linkers together with the subsequent crystallization step in an autoclave with acetic acid vapor. For simplicity, the acetic acid modulation is not included in the figure, this would be a part of the MLD cycle, and is added after the pulse of the organic acids.

All in all, the work presented in this thesis brings us one step closer to achieving applications for MOFs by synthesizing thin films in an all-gas-phase manner. Along the way, an acetic acid modulation of the MLD process, and a gas-phase autoclave crystallization of the films have been developed. Together, they provide further parameters to tune in order to improve the films or develop a larger repertory of MOF thin films. Since the properties of MOFs can vary greatly with their structure and chemical composition, a wide selection of MOF thin films could enable several new technologies that may include new diagnostic methods, more controlled cancer treatment, highly sensitive gas sensors or new types of batteries. At this stage, it is impossible to know if or when these dreams can be realized and only time and further research will tell.

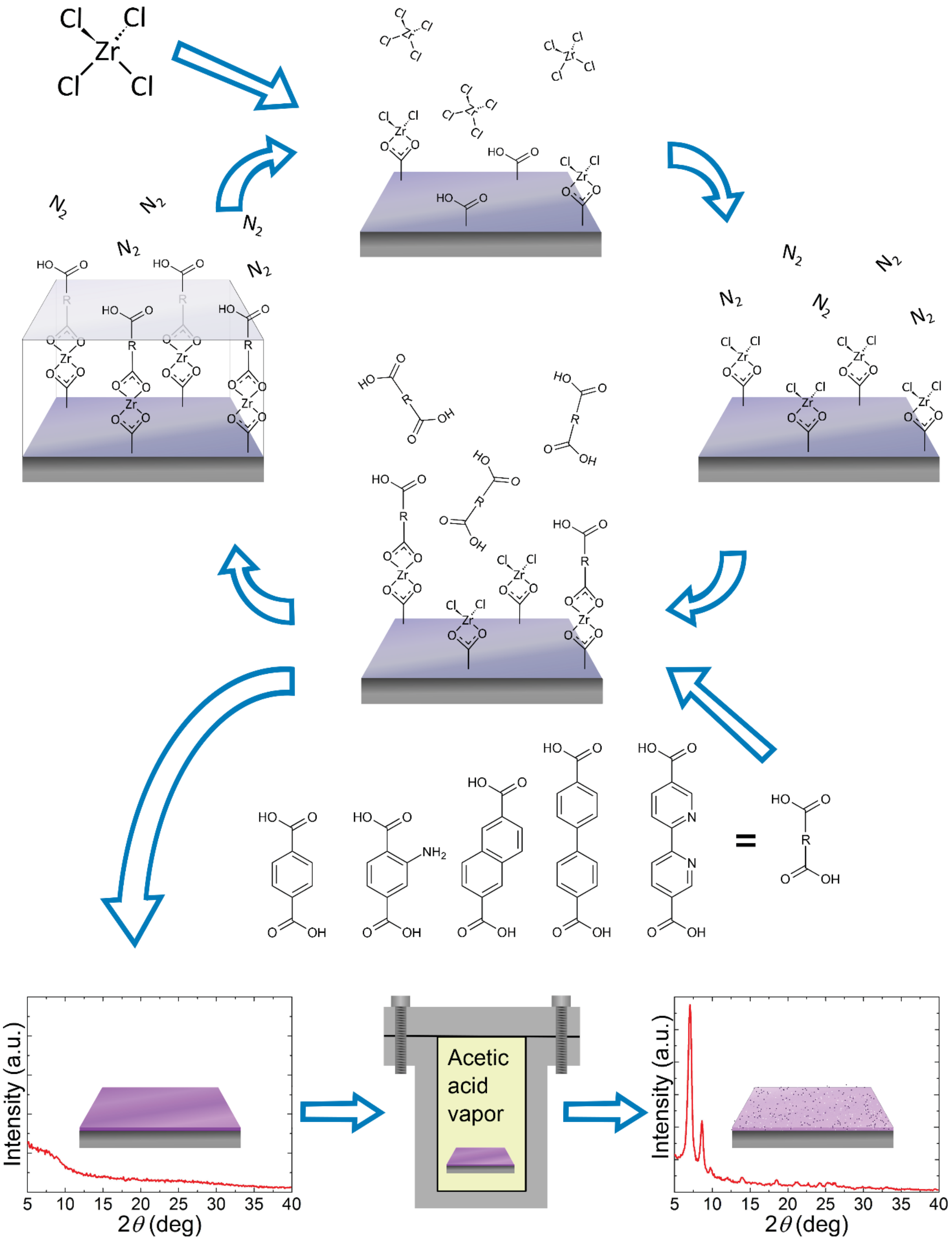

Figure 30: An illustration summarizing the work in this thesis including the MLD cycle and the subsequent crystallization step. Acetic acid modulation during the MLD cycle is not shown in this illustration.

7. References

1. United Nations, *Transforming our World: The 2030 Agenda for Sustainable Development*, **2015**, URL:https://sustainabledevelopment.un.org/post2015/transformingourworld. Accessed: 2018-10-29. (Archived by WebCite® at http://www.webcitation.org/73X7Gqyw7)
2. Liu, X., Keser Demir, N., Wu, Z. and Li, K., *Highly Water Stable Zirconium Metal-Organic Framework UiO-66 Membranes Supported on Alumina Hollow Fibers for Desalination*, *Journal of the American Chemical Society*, **2015**, 6999–7002.
3. Allendorf, M. D., Schwartzberg, A., Stavila, V. and Talin, A. A., *A Roadmap to Implementing Metal–Organic Frameworks in Electronic Devices: Challenges and Critical Directions*, *Chemistry – A European Journal*, **2011**, *17*, 11372-11388.
4. Allendorf, M. D., Bauer, C. A., Bhakta, R. K. and Houk, R. J. T., *Luminescent metal–organic frameworks*, *Chemical Society Reviews*, **2009**, *38*, 1330-1352.
5. Wyszogrodzka, G., Marszałek, B., Gil, B. and Dorożyński, P., *Metal-organic frameworks: mechanisms of antibacterial action and potential applications*, *Drug Discovery Today*, **2016**, *21*, 1009-1018.
6. Mueller, U., Schubert, M., Teich, F., Puetter, H., Schierle-Arndt, K. and Pastré, J., *Metal–organic frameworks—prospective industrial applications*, *Journal of Materials Chemistry*, **2006**, *16*, 626-636.
7. Abid, H. R., Tian, H., Ang, H.-M., Tade, M. O., Buckley, C. E. and Wang, S., *Nanosize Zr-metal organic framework (UiO-66) for hydrogen and carbon dioxide storage*, *Chemical Engineering Journal*, **2012**, *187*, 415-420.
8. Suh, M. P., Park, H. J., Prasad, T. K. and Lim, D.-W., *Hydrogen Storage in Metal–Organic Frameworks*, *Chemical Reviews*, **2012**, *112*, 782-835.
9. Getman, R. B., Bae, Y.-S., Wilmer, C. E. and Snurr, R. Q., *Review and Analysis of Molecular Simulations of Methane, Hydrogen, and Acetylene Storage in Metal–Organic Frameworks*, *Chemical Reviews*, **2012**, *112*, 703-723.
10. Lee, J., Farha, O. K., Roberts, J., Scheidt, K. A., Nguyen, S. T. and Hupp, J. T., *Metal-organic framework materials as catalysts*, *Chemical Society Reviews*, **2009**, *38*, 1450-1459.
11. Long, J., Wang, S., Ding, Z., Wang, S., Zhou, Y., Huang, L. and Wang, X., *Amine-functionalized zirconium metal–organic framework as efficient visible-light photocatalyst for aerobic organic transformations*, *Chemical Communications*, **2012**, *48*, 11656-11658.
12. Li, J.-R., Sculley, J. and Zhou, H.-C., *Metal–Organic Frameworks for Separations*, *Chemical Reviews*, **2012**, *112*, 869-932.
13. Taylor-Pashow, K. M. L., Rocca, J. D., Xie, Z., Tran, S. and Lin, W., *Postsynthetic Modifications of Iron-Carboxylate Nanoscale Metal−Organic Frameworks for Imaging and Drug Delivery*, *Journal of the American Chemical Society*, **2009**, *131*, 14261-14263.
14. Jakobsen, S., Gianolio, D., Wragg, D. S., Nilsen, M. H., Emerich, H., Bordiga, S., Lamberti, C., Olsbye, U., Tilset, M. and Lillerud, K. P., *Structural determination of a highly stable metal-organic framework with possible application to interim radioactive waste scavenging: Hf-UiO-66*, *Physical Review B*, **2012**, *86*, 125429.
15. Wang, C., Liu, X., Chen, J. P. and Li, K., *Superior removal of arsenic from water with zirconium metal-organic framework UiO-66*, *Scientific Reports*, **2015**, *5*, 16613.
16. Mondloch, J. E., Katz, M. J., Isley Iii, W. C., Ghosh, P., Liao, P., Bury, W., Wagner, G. W., Hall, M. G., DeCoste, J. B., Peterson, G. W., Snurr, R. Q., Cramer, C. J., Hupp, J. T. and Farha, O. K., *Destruction of chemical warfare agents using metal–organic frameworks*, *Nature Materials*, **2015**, *14*, 512-516.

17. Lee, D. T., Zhao, J., Peterson, G. W. and Parsons, G. N., *Catalytic "MOF-Cloth" Formed via Directed Supramolecular Assembly of UiO-66-NH_2 Crystals on Atomic Layer Deposition-Coated Textiles for Rapid Degradation of Chemical Warfare Agent Simulants*, *Chemistry of Materials*, **2017**, *29*, 4894-4903.

18. Hoskins, B. F. and Robson, R., *Design and construction of a new class of scaffolding-like materials comprising infinite polymeric frameworks of 3D-linked molecular rods. A reappraisal of the zinc cyanide and cadmium cyanide structures and the synthesis and structure of the diamond-related frameworks [N(CH3)4][CuIZnII(CN)4] and CuI[4,4',4'',4'''-tetracyanotetraphenylmethane]BF4.xC6H5NO2*, *Journal of the American Chemical Society*, **1990**, *112*, 1546-1554.

19. Hoskins, B. F. and Robson, R., *Infinite polymeric frameworks consisting of three dimensionally linked rod-like segments*, *Journal of the American Chemical Society*, **1989**, *111*, 5962-5964.

20. Yaghi, O. M., Li, G. and Li, H., *Selective binding and removal of guests in a microporous metal–organic framework*, *Nature*, **1995**, *378*, 703.

21. Li, H., Eddaoudi, M., O'Keeffe, M. and Yaghi, O. M., *Design and synthesis of an exceptionally stable and highly porous metal-organic framework*, *Nature*, **1999**, *402*, 276-279.

22. Chui, S. S.-Y., Lo, S. M.-F., Charmant, J. P. H., Orpen, A. G. and Williams, I. D., *A Chemically Functionalizable Nanoporous Material* $[Cu_3(TMA)_2(H_2O)_3]_n$, *Science*, **1999**, *283*, 1148-1150.

23. Férey, G., Serre, C., Mellot-Draznieks, C., Millange, F., Surblé, S., Dutour, J. and Margiolaki, I., *A Hybrid Solid with Giant Pores Prepared by a Combination of Targeted Chemistry, Simulation, and Powder Diffraction*, *Angewandte Chemie*, **2004**, *116*, 6456-6461.

24. Férey, G., Mellot-Draznieks, C., Serre, C., Millange, F., Dutour, J., Surblé, S. and Margiolaki, I., *A Chromium Terephthalate-Based Solid with Unusually Large Pore Volumes and Surface Area*, *Science*, **2005**, *309*, 2040-2042.

25. Banerjee, R., Phan, A., Wang, B., Knobler, C., Furukawa, H., O'Keeffe, M. and Yaghi, O. M., *High-Throughput Synthesis of Zeolitic Imidazolate Frameworks and Application to* CO_2 *Capture*, *Science*, **2008**, *319*, 939-943.

26. Cavka, J. H., Jakobsen, S., Olsbye, U., Guillou, N., Lamberti, C., Bordiga, S. and Lillerud, K. P., *A new zirconium inorganic building brick forming metal organic frameworks with exceptional stability*, *Journal of the American Chemical Society*, **2008**, *130*, 13850-13851.

27. Stock, N. and Biswas, S., *Synthesis of Metal-Organic Frameworks (MOFs): Routes to Various MOF Topologies, Morphologies, and Composites*, *Chemical Reviews*, **2012**, *112*, 933-969.

28. Lock, N., Wu, Y., Christensen, M., Cameron, L. J., Peterson, V. K., Bridgeman, A. J., Kepert, C. J. and Iversen, B. B., *Elucidating Negative Thermal Expansion in MOF-5*, *The Journal of Physical Chemistry C*, **2010**, *114*, 16181-16186.

29. Yakovenko, A. A., Reibenspies, J. H., Bhuvanesh, N. and Zhou, H.-C., *Generation and applications of structure envelopes for porous metal-organic frameworks*, *Journal of Applied Crystallography*, **2013**, *46*, 346-353.

30. Karagiaridi, O., Lalonde, M. B., Bury, W., Sarjeant, A. A., Farha, O. K. and Hupp, J. T., *Opening ZIF-8: A Catalytically Active Zeolitic Imidazolate Framework of Sodalite Topology with Unsubstituted Linkers*, *Journal of the American Chemical Society*, **2012**, *134*, 18790-18796.

31. Øien, S., Wragg, D., Reinsch, H., Svelle, S., Bordiga, S., Lamberti, C. and Lillerud, K. P., *Detailed Structure Analysis of Atomic Positions and Defects in Zirconium Metal–Organic Frameworks*, *Crystal Growth & Design*, **2014**, *14*, 5370-5372.

32. Li, H., Eddaoudi, M., Groy, T. L. and Yaghi, O. M., *Establishing Microporosity in Open Metal−Organic Frameworks: Gas Sorption Isotherms for Zn(BDC) (BDC = 1,4-Benzenedicarboxylate)*, *Journal of the American Chemical Society*, **1998**, *120*, 8571-8572.

33. Furukawa, H., Cordova, K. E., O'Keeffe, M. and Yaghi, O. M., *The Chemistry and Applications of Metal-Organic Frameworks*, *Science*, **2013**, *341*.

34. Braglia, L., Borfecchia, E., Lomachenko, K. A., Bugaev, A. L., Guda, A. A., Soldatov, A. V., Bleken, B. T. L., Øien-Ødegaard, S., Olsbye, U., Lillerud, K. P., Bordiga, S., Agostini, G., Manzoli, M. and Lamberti, C., *Tuning Pt and Cu sites population inside functionalized UiO-67 MOF by controlling activation conditions*, *Faraday Discussions*, **2017**, *201*, 265-286.

35. Yaghi, O. M., O'Keeffe, M., Ockwig, N. W., Chae, H. K., Eddaoudi, M. and Kim, J., *Reticular synthesis and the design of new materials*, *Nature*, **2003**, *423*, 705.

36. Nagao, Y., Ikeda, R., Kanda, S., Kubozono, Y. and Kitagawa, H., *Complex-Plane Impedance Study on a Hydrogen-Doped Copper Coordination Polymer: N,N '-bis-(2-hydroxyethyl)dithiooxamidato-copper(II)*, *Molecular Crystals and Liquid Crystals*, **2002**, *379*, 89-94.

37. Taylor, J. M., Dawson, K. W. and Shimizu, G. K. H., *A Water-Stable Metal–Organic Framework with Highly Acidic Pores for Proton-Conducting Applications*, *Journal of the American Chemical Society*, **2013**, *135*, 1193-1196.

38. Deng, H., Grunder, S., Cordova, K. E., Valente, C., Furukawa, H., Hmadeh, M., Gándara, F., Whalley, A. C., Liu, Z., Asahina, S., Kazumori, H., O'Keeffe, M., Terasaki, O., Stoddart, J. F. and Yaghi, O. M., *Large-Pore Apertures in a Series of Metal-Organic Frameworks*, *Science*, **2012**, *336*, 1018-1023.

39. Wang, C., *Pt Nanoparticles@Photoactive Metal–Organic Frameworks: Efficient Hydrogen Evolution via Synergistic Photoexcitation and Electron Injection*, *Journal of the American Chemical Society*, **2012**, *v. 134*, pp. 7211-7214-2012 v.7134 no.7217.

40. Thoresen, E. M., Balcells, D., Øien-Ødegaard, S., Hylland, K. T., Tilset, M. and Amedjkouh, M., *Cyclometalated ruthenium complexes with carboxylated ligands from a combined experimental/computational perspective*, *Dalton Transactions*, **2018**, *47*, 2589-2601.

41. Huang, L., Wang, H., Chen, J., Wang, Z., Sun, J., Zhao, D. and Yan, Y., *Synthesis, morphology control, and properties of porous metal–organic coordination polymers*, *Microporous and Mesoporous Materials*, **2003**, *58*, 105-114.

42. Tranchemontagne, D. J., Hunt, J. R. and Yaghi, O. M., *Room temperature synthesis of metal-organic frameworks: MOF-5, MOF-74, MOF-177, MOF-199, and IRMOF-0*, *Tetrahedron*, **2008**, *64*, 8553-8557.

43. Jhung, S. H., Lee, J.-H., Forster, P. M., Férey, G., Cheetham, A. K. and Chang, J.-S., *Microwave Synthesis of Hybrid Inorganic–Organic Porous Materials: Phase-Selective and Rapid Crystallization*, *Chemistry – A European Journal*, **2006**, *12*, 7899-7905.

44. Ahnfeldt, T., Moellmer, J., Guillerm, V., Staudt, R., Serre, C. and Stock, N., *High-Throughput and Time-Resolved Energy-Dispersive X-Ray Diffraction (EDXRD) Study of the Formation of CAU-1-(OH)$_2$: Microwave and Conventional Heating*, *Chemistry – A European Journal*, **2011**, *17*, 6462-6468.

45. Haque, E., Khan, N. A., Park, J. H. and Jhung, S. H., *Synthesis of a Metal–Organic Framework Material, Iron Terephthalate, by Ultrasound, Microwave, and Conventional Electric Heating: A Kinetic Study*, *Chemistry – A European Journal*, **2010**, *16*, 1046-1052.

46. Chalati, T., Horcajada, P., Gref, R., Couvreur, P. and Serre, C., *Optimisation of the synthesis of MOF nanoparticles made of flexible porous iron fumarate MIL-88A*, *Journal of Materials Chemistry*, **2011**, *21*, 2220-2227.

47. Bauer, S. and Stock, N., *Implementation of a Temperature-Gradient Reactor System for High-Throughput Investigation of Phosphonate-Based Inorganic–Organic Hybrid Compounds*, *Angewandte Chemie International Edition*, **2007**, *46*, 6857-6860.

48. Rabenau, A., *The Role of Hydrothermal Synthesis in Preparative Chemistry*, *Angewandte Chemie International Edition in English*, **1985**, *24*, 1026-1040.

49. Millange, F., Medina, M. I., Guillou, N., Férey, G., Golden, K. M. and Walton, R. I., *Time-Resolved In Situ Diffraction Study of the Solvothermal Crystallization of Some Prototypical Metal–Organic Frameworks*, *Angewandte Chemie*, **2010**, *122*, 775-778.

50. Willans, C. E., French, S., Anderson, K. M., Barbour, L. J., Gertenbach, J.-A., Lloyd, G. O., Dyer, R. J., Junk, P. C. and Steed, J. W., *Tripodal imidazole frameworks: Reversible vapour sorption both with and without significant structural changes*, *Dalton Transactions*, **2011**, *40*, 573-582.

51. Pichon, A., Lazuen-Garay, A. and James, S. L., *Solvent-free synthesis of a microporous metal–organic framework*, *CrystEngComm*, **2006**, *8*, 211-214.

52. Pichon, A. and James, S. L., *An array-based study of reactivity under solvent-free mechanochemical conditions—insights and trends*, *CrystEngComm*, **2008**, *10*, 1839-1847.

53. Yuan, W., Garay, A. L., Pichon, A., Clowes, R., Wood, C. D., Cooper, A. I. and James, S. L., *Study of the mechanochemical formation and resulting properties of an archetypal MOF: Cu3 (BTC) 2 (BTC= 1, 3, 5-benzenetricarboxylate)*, *CrystEngComm*, **2010**, *12*, 4063-4065.

54. Crawford, D., Casaban, J., Haydon, R., Giri, N., McNally, T. and James, S. L., *Synthesis by extrusion: continuous, large-scale preparation of MOFs using little or no solvent*, *Chemical Science*, **2015**, *6*, 1645-1649.

55. Klimakow, M., Klobes, P., Thünemann, A. F., Rademann, K. and Emmerling, F., *Mechanochemical synthesis of metal− organic frameworks: a fast and facile approach toward quantitative yields and high specific surface areas*, *Chemistry of Materials*, **2010**, *22*, 5216-5221.

56. Friščić, T. and Fábián, L., *Mechanochemical conversion of a metal oxide into coordination polymers and porous frameworks using liquid-assisted grinding (LAG)*, *CrystEngComm*, **2009**, *11*, 743-745.

57. Yuan, W., Friščić, T., Apperley, D. and James, S. L., *High Reactivity of Metal–Organic Frameworks under Grinding Conditions: Parallels with Organic Molecular Materials*, *Angewandte Chemie International Edition*, **2010**, *49*, 3916-3919.

58. Bux, H., Liang, F., Li, Y., Cravillon, J., Wiebcke, M. and Caro, J., *Zeolitic Imidazolate Framework Membrane with Molecular Sieving Properties by Microwave-Assisted Solvothermal Synthesis*, *Journal of the American Chemical Society*, **2009**, *131*, 16000-16001.

59. Arnold, M., Kortunov, P., Jones, D. J., Nedellec, Y., Kärger, J. and Caro, J., *Oriented Crystallisation on Supports and Anisotropic Mass Transport of the Metal-Organic Framework Manganese Formate*, *European Journal of Inorganic Chemistry*, **2007**, *2007*, 60-64.

60. Yao, J., Dong, D., Li, D., He, L., Xu, G. and Wang, H., *Contra-diffusion synthesis of ZIF-8 films on a polymer substrate*, *Chemical Communications*, **2011**, *47*, 2559-2561.

61. Hermes, S., Schröder, F., Chelmowski, R., Wöll, C. and Fischer, R. A., *Selective Nucleation and Growth of Metal−Organic Open Framework Thin Films on Patterned COOH/CF_3-Terminated Self-Assembled Monolayers on Au(111)*, *Journal of the American Chemical Society*, **2005**, *127*, 13744-13745.

62. Zacher, D., Baunemann, A., Hermes, S. and Fischer, R. A., *Deposition of microcrystalline [$Cu_3(btc)_2$] and [$Zn_2(bdc)_2(dabco)$] at alumina and silica surfaces modified with patterned self assembled organic monolayers: evidence of surface selective and oriented growth*, *Journal of Materials Chemistry*, **2007**, *17*, 2785-2792.

63. Miyamoto, M., Kohmura, S., Iwatsuka, H., Oumi, Y. and Uemiya, S., *In situ solvothermal growth of highly oriented Zr-based metal organic framework UiO-66 film with monocrystalline layer*, *CrystEngComm*, **2015**, *17*, 3422-3425.

64. Shekhah, O., Wang, H., Zacher, D., Fischer, R. A. and Wöll, C., *Growth Mechanism of Metal–Organic Frameworks: Insights into the Nucleation by Employing a Step-by-Step Route*, *Angewandte Chemie International Edition*, **2009**, *48*, 5038-5041.

65. Shekhah, O., Wang, H., Kowarik, S., Schreiber, F., Paulus, M., Tolan, M., Sternemann, C., Evers, F., Zacher, D. and Fischer, R. A., *Step-by-step route for the synthesis of metal− organic frameworks*, *Journal of the American Chemical Society*, **2007**, *129*, 15118-15119.

66. Munuera, C., Shekhah, O., Wang, H., Wöll, C. and Ocal, C., *The controlled growth of oriented metal–organic frameworks on functionalized surfaces as followed by scanning force microscopy*, *Physical Chemistry Chemical Physics*, **2008**, *10*, 7257-7261.

67. Shekhah, O., Wang, H., Paradinas, M., Ocal, C., Schüpbach, B., Terfort, A., Zacher, D., Fischer, R. A. and Wöll, C., *Controlling interpenetration in metal–organic frameworks by liquid-phase epitaxy*, *Nature Materials*, **2009**, *8*, 481.

68. Zacher, D., Yusenko, K., Bétard, A., Henke, S., Molon, M., Ladnorg, T., Shekhah, O., Schüpbach, B., de los Arcos, T., Krasnopolski, M., Meilikhov, M., Winter, J., Terfort, A., Wöll, C. and Fischer, R. A., *Liquid-Phase Epitaxy of Multicomponent Layer-Based Porous Coordination Polymer Thin Films of [M(L)(P)0.5] Type: Importance of Deposition Sequence on the Oriented Growth*, *Chemistry – A European Journal*, **2011**, *17*, 1448-1455.

69. Guo, H., Zhu, S., Cai, D. and Liu, C., *Fabrication of ITO glass supported Tb-MOF film for sensing organic solvent*, *Inorganic Chemistry Communications*, **2014**, *41*, 29-32.

70. Demessence, A., Boissiere, C., Grosso, D., Horcajada, P., Serre, C., Férey, G., Soler-Illia, G. J. and Sanchez, C., *Adsorption properties in high optical quality nanoZIF-8 thin films with tunable thickness*, *Journal of Materials Chemistry*, **2010**, *20*, 7676-7681.

71. Gascon, J., Aguado, S. and Kapteijn, F., *Manufacture of dense coatings of $Cu_3(BTC)_2$ (HKUST-1) on α-alumina*, *Microporous and Mesoporous Materials*, **2008**, *113*, 132-138.

72. Bux, H., Feldhoff, A., Cravillon, J., Wiebcke, M., Li, Y.-S. and Caro, J., *Oriented Zeolitic Imidazolate Framework-8 Membrane with Sharp H_2/C_3H_8 Molecular Sieve Separation*, *Chemistry of Materials*, **2011**, *23*, 2262-2269.

73. Li, Y.-S., Bux, H., Feldhoff, A., Li, G.-L., Yang, W.-S. and Caro, J., *Controllable Synthesis of Metal–Organic Frameworks: From MOF Nanorods to Oriented MOF Membranes*, *Advanced Materials*, **2010**, *22*, 3322-3326.

74. Yusenko, K., Meilikhov, M., Zacher, D., Wieland, F., Sternemann, C., Stammer, X., Ladnorg, T., Wöll, C. and Fischer, R. A., *Step-by-step growth of highly oriented and continuous seeding layers of $[Cu_2(ndc)_2(dabco)]$ on bare oxide and nitride substrates*, *CrystEngComm*, **2010**, *12*, 2086-2090.

75. Kubo, M., Chaikittisilp, W. and Okubo, T., *Oriented Films of Porous Coordination Polymer Prepared by Repeated in Situ Crystallization*, *Chemistry of Materials*, **2008**, *20*, 2887-2889.

76. Lu, G. and Hupp, J. T., *Metal−Organic Frameworks as Sensors: A ZIF-8 Based Fabry−Pérot Device as a Selective Sensor for Chemical Vapors and Gases*, *Journal of the American Chemical Society*, **2010**, *132*, 7832-7833.

77. Ameloot, R., Stappers, L., Fransaer, J., Alaerts, L., Sels, B. F. and De Vos, D. E., *Patterned Growth of Metal-Organic Framework Coatings by Electrochemical Synthesis*, *Chemistry of Materials*, **2009**, *21*, 2580-2582.

78. Stassen, I., Styles, M., Van Assche, T., Campagnol, N., Fransaer, J., Denayer, J., Tan, J.-C., Falcaro, P., De Vos, D. and Ameloot, R., *Electrochemical Film Deposition of the Zirconium Metal–Organic Framework UiO-66 and Application in a Miniaturized Sorbent Trap*, *Chemistry of Materials*, **2015**, *27*, 1801-1807.

79. Bétard, A. and Fischer, R. A., *Metal–Organic Framework Thin Films: From Fundamentals to Applications*, *Chemical Reviews*, **2012**, *112*, 1055-1083.

80. Shekhah, O., Liu, J., Fischer, R. and Wöll, C., *MOF thin films: existing and future applications*, *Chemical Society Reviews*, **2011**, *40*, 1081-1106.

81. Stassen, I., Campagnol, N., Fransaer, J., Vereecken, P., De Vos, D. and Ameloot, R., *Solvent-free synthesis of supported ZIF-8 films and patterns through transformation of deposited zinc oxide precursors*, *CrystEngComm*, **2013**, *15*, 9308-9311.

82. Ameloot, R., Gobechiya, E., Uji-i, H., Martens, J. A., Hofkens, J., Alaerts, L., Sels, B. F. and De Vos, D. E., *Direct Patterning of Oriented Metal–Organic Framework Crystals via Control over Crystallization Kinetics in Clear Precursor Solutions*, *Advanced Materials*, **2010**, *22*, 2685-2688.

83. Ameloot, R., Pandey, L., Van der Auweraer, M., Alaerts, L., Sels, B. F. and De Vos, D. E., *Patterned film growth of metal–organic frameworks based on galvanic displacement*, *Chemical Communications*, **2010**, *46*, 3735-3737.

84. Miikkulainen, V., Leskelä, M., Ritala, M. and Puurunen, R. L., *Crystallinity of inorganic films grown by atomic layer deposition: Overview and general trends*, *Journal of Applied Physics*, **2013**, *113*, 021301.

85. Malygin, A. A., Drozd, V. E., Malkov, A. A. and Smirnov, V. M., *From V. B. Aleskovskii's "Framework" Hypothesis to the Method of Molecular Layering/Atomic Layer Deposition*, *Chemical Vapor Deposition*, **2015**, *21*, 216-240.

86. Suntola, T. and Antson, J., *Method for producing compound thin films*, **1977**.

87. Hoffmann, L., Brinkmann, K. O., Malerczyk, J., Rogalla, D., Becker, T., Theirich, D., Shutsko, I., Görrn, P. and Riedl, T., *Spatial Atmospheric Pressure Atomic Layer Deposition of Tin Oxide as an Impermeable Electron Extraction Layer for Perovskite Solar Cells with Enhanced Thermal Stability*, *ACS Applied Materials & Interfaces*, **2018**, *10*, 6006-6013.

88. Mousa, M. B. M., Oldham, C. J. and Parsons, G. N., *Atmospheric Pressure Atomic Layer Deposition of* Al_2O_3 *Using Trimethyl Aluminum and Ozone*, *Langmuir*, **2014**, *30*, 3741-3748.

89. Vee, I., Master thesis, University of Oslo, **2012**.

90. Matero, R., Rahtu, A., Ritala, M., Leskelä, M. and Sajavaara, T., *Effect of water dose on the atomic layer deposition rate of oxide thin films*, *Thin Solid Films*, **2000**, *368*, 1-7.

91. Törndahl, T., Platzer-Björkman, C., Kessler, J. and Edoff, M., *Atomic layer deposition of* $Zn_{1-x}Mg_xO$ *buffer layers for* $Cu(In,Ga)Se_2$ *solar cells*, *Progress in Photovoltaics: Research and Applications*, **2007**, *15*, 225-235.

92. Aaltonen, T., Alnes, M., Nilsen, O., Costelle, L. and Fjellvåg, H., *Lanthanum titanate and lithium lanthanum titanate thin films grown by atomic layer deposition*, *Journal of Materials Chemistry*, **2010**, *20*, 2877-2881.

93. Kemell, M., Färm, E., Ritala, M. and Leskelä, M., *Surface modification of thermoplastics by atomic layer deposition of* Al_2O_3 *and* TiO_2 *thin films*, *European Polymer Journal*, **2008**, *44*, 3564-3570.

94. Färm, E., Kemell, M., Santala, E., Ritala, M. and Leskelä, M., *Selective-area atomic layer deposition using poly (vinyl pyrrolidone) as a passivation layer*, *Journal of the Electrochemical Society*, **2010**, *157*, K10-K14.

95. Hiltunen, L., Kattelus, H., Leskelä, M., Mäkelä, M., Niinistö, L., Nykänen, E., Soininen, P. and Tiittad, M., *Growth and characterization of aluminium oxide thin films deposited from various source materials by atomic layer epitaxy and chemical vapor deposition processes*, *Materials Chemistry and Physics*, **1991**, *28*, 379-388.

96. Jakschik, S., Schroeder, U., Hecht, T., Krueger, D., Dollinger, G., Bergmaier, A., Luhmann, C. and Bartha, J. W., *Physical characterization of thin ALD–Al_2O_3 films*, *Applied Surface Science*, **2003**, *211*, 352-359.

97. Kawahara, T., Torii, K., Mitsuhashi, R., Muto, A., Horiuchi, A., Ito, H. and Kitajima, H., *Effect of Hf sources, oxidizing agents, and NH_3/Ar plasma on the properties of $HfAlO_x$ films prepared by atomic layer deposition*, *Japanese journal of applied physics*, **2004**, *43*, 4129.

98. Jokinen, J., Haussalo, P., Keinonen, J., Ritala, M., Riihelä, D. and Leskelä, M., *Analysis of AlN thin films by combining TOF-ERDA and NRB techniques*, *Thin Solid Films*, 1996, *289*, 159-165.

99. Hiltunen, L., Leskelä, M., Mäkelä, M., Niinistö, L., Nykänen, E. and Soininen, P., *NITRIDES OF TITANIUM, NIOBIUM, TANTALUM AND MOLYBDENUM GROWN AS THIN FILMS BY THE ATOMIC LAYER EPITAXY METHOD*, Proceedings of the 15th International Conference on Metallurgical Coatings, San Diego, CA, U.S.A., April 11–15, 1988, 149-154.

100. Pilvi, T., Hatanpää, T., Puukilainen, E., Arstila, K., Bischoff, M., Kaiser, U., Kaiser, N., Leskelä, M. and Ritala, M., *Study of a novel ALD process for depositing MgF_2 thin films*, *Journal of Materials Chemistry*, **2007**, *17*, 5077-5083.

101. Pilvi, T., Ritala, M., Leskelä, M., Bischoff, M., Kaiser, U. and Kaiser, N., *Atomic layer deposition process with TiF_4 as a precursor for depositing metal fluoride thin films*, *Applied Optics*, **2008**, *47*, C271-C274.

102. Pore, V., Ritala, M. and Leskelä, M., *Atomic layer deposition of titanium disulfide thin films*, *Chemical Vapor Deposition*, **2007**, *13*, 163-168.

103. Mårtensson, P. and Carlsson, J. O., *Atomic layer epitaxy of copper on tantalum*, *Chemical Vapor Deposition*, **1997**, *3*, 45-50.

104. Henkel, C., Abermann, S., Bethge, O. and Bertagnolli, E., *Atomic layer-deposited platinum in high-k/metal gate stacks*, *Semiconductor Science and Technology*, **2009**, *24*, 125013.

105. Yoshimura, T., Tatsuura, S. and Sotoyama, W., *Polymer films formed with monolayer growth steps by molecular layer deposition*, *Applied Physics Letters*, **1991**, *59*, 482-484.

106. Salmi, L. D., Puukilainen, E., Vehkamäki, M., Heikkilä, M. and Ritala, M., *Atomic Layer Deposition of Ta_2O_5/Polyimide Nanolaminates*, *Chemical Vapor Deposition*, **2009**, *15*, 221-226.

107. Putkonen, M., Harjuoja, J., Sajavaara, T. and Niinistö, L., *Atomic layer deposition of polyimide thin films*, *Journal of Materials Chemistry*, **2007**, *17*, 664-669.

108. Shao, H.-I., Umemoto, S., Kikutani, T. and Okui, N., *Layer-by-layer polycondensation of nylon 66 by alternating vapour deposition polymerization*, *Polymer*, **1997**, *38*, 459-462.

109. Du, Y. and George, S. M., *Molecular Layer Deposition of Nylon 66 Films Examined Using in Situ FTIR Spectroscopy*, *The Journal of Physical Chemistry C*, **2007**, *111*, 8509-8517.

110. Peng, Q., Efimenko, K., Genzer, J. and Parsons, G. N., *Oligomer Orientation in Vapor-Molecular-Layer-Deposited Alkyl-Aromatic Polyamide Films*, *Langmuir*, **2012**, *28*, 10464-10470.

111. Loscutoff, P. W., Zhou, H., Clendenning, S. B. and Bent, S. F., *Formation of Organic Nanoscale Laminates and Blends by Molecular Layer Deposition*, *ACS Nano*, **2010**, *4*, 331-341.

112. Ivanova, T. V., Maydannik, P. S. and Cameron, D. C., *Molecular layer deposition of polyethylene terephthalate thin films*, *Journal of Vacuum Science & Technology A*, **2012**, *30*, 01A121.

113. Meng, X., *An overview of molecular layer deposition for organic and organic–inorganic hybrid materials: mechanisms, growth characteristics, and promising applications*, *Journal of Materials Chemistry A*, **2017**, *5*, 18326-18378.

114. Leskelä, M., Ritala, M. and Nilsen, O., *Novel materials by atomic layer deposition and molecular layer deposition*, *MRS bulletin*, **2011**, *36*, 877-884.

115. Nilsen, O. and Fjellvag, H., *Thin films prepared with gas phase deposition technique*, **2012**.

116. Park, Y., Han, K. S., Lee, B. H., Cho, S., Lee, K. H., Im, S. and Sung, M. M., *High performance n-type organic–inorganic nanohybrid semiconductors for flexible electronic devices*, *Organic Electronics*, **2011**, *12*, 348-352.

117. Yoon, B., Lee, B. H. and George, S. M., *Highly Conductive and Transparent Hybrid Organic–Inorganic Zincone Thin Films Using Atomic and Molecular Layer Deposition*, *The Journal of Physical Chemistry C*, **2012**, *116*, 24784-24791.

118. Kao, C.-Y., Yoo, J.-W., Min, Y. and Epstein, A. J., *Molecular Layer Deposition of an Organic-Based Magnetic Semiconducting Laminate*, *ACS Applied Materials & Interfaces*, **2012**, *4*, 137-141.

119. Van de Kerckhove, K., Mattelaer, F., Deduytsche, D., Vereecken, P. M., Dendooven, J. and Detavernier, C., *Molecular layer deposition of "titanicone", a titanium-based hybrid material, as an electrode for lithium-ion batteries*, *Dalton Transactions*, **2016**, *45*, 1176-1184.

120. Dameron, A. A., Seghete, D., Burton, B. B., Davidson, S. D., Cavanagh, A. S., Bertrand, J. A. and George, S. M., *Molecular Layer Deposition of Alucone Polymer Films Using Trimethylaluminum and Ethylene Glycol*, *Chemistry of Materials*, **2008**, *20*, 3315-3326.

121. Zhou, W., Leem, J., Park, I., Li, Y., Jin, Z. and Min, Y.-S., *Charge trapping behavior in organic–inorganic alloy films grown by molecular layer deposition from trimethylaluminum, p-phenylenediamine and water*, *Journal of Materials Chemistry*, **2012**, *22*, 23935-23943.

122. Park, Y.-S., Kim, H., Cho, B., Lee, C., Choi, S.-E., Sung, M. M. and Lee, J. S., *Intramolecular and Intermolecular Interactions in Hybrid Organic–Inorganic Alucone Films Grown by Molecular Layer Deposition*, *ACS Applied Materials & Interfaces*, **2016**, *8*, 17489-17498.

123. Brown, J. J., Hall, R. A., Kladitis, P. E., George, S. M. and Bright, V. M., *Molecular layer deposition on carbon nanotubes*, *ACS Nano*, **2013**, *7*, 7812-7823.

124. Peng, Q., Gong, B., VanGundy, R. M. and Parsons, G. N., *"Zincone" Zinc Oxide−Organic Hybrid Polymer Thin Films Formed by Molecular Layer Deposition*, *Chemistry of Materials*, **2009**, *21*, 820-830.

125. Klepper, K. B., Nilsen, O., Levy, T. and Fjellvag, H., *Atomic Layer Deposition of Organic-Inorganic Hybrid Materials Based on Unsaturated Linear Carboxylic Acids*, *European Journal of Inorganic Chemistry*, **2011**, *34*, 5305-5312.

126. Klepper, K. B., Nilsen, O., Hansen, P. A. and Fjellvag, H., *Atomic layer deposition of organic-inorganic hybrid materials based on saturated linear carboxylic acids*, *Dalton Transactions*, **2011**, *40*, 4636-4646.

127. Klepper, K. B., Nilsen, O. and Fjellvag, H., *Deposition of thin films of organic-inorganic hybrid materials based on aromatic carboxylic acids by atomic layer deposition*, *Dalton Transactions*, **2010**, *39*, 11628-11635.

128. Salmi, L. D., Heikkilä, M. J., Puukilainen, E., Sajavaara, T., Grosso, D. and Ritala, M., *Studies on atomic layer deposition of MOF-5 thin films*, *Microporous and Mesoporous Materials*, **2013**, *182*, 147-154.

129. Salmi, L. D., Heikkilä, M. J., Vehkamäki, M., Puukilainen, E., Ritala, M. and Sajavaara, T., *Studies on atomic layer deposition of IRMOF-8 thin films*, *Journal of Vacuum Science & Technology A*, **2015**, *33*, 01A121.

130. Ahvenniemi, E. and Karppinen, M., *Atomic/molecular layer deposition: a direct gas-phase route to crystalline metal–organic framework thin films*, *Chemical Communications*, **2016**, 1139-1142.

131. Tanskanen, A. and Karppinen, M., *Iron-Terephthalate Coordination Network Thin Films Through In-Situ Atomic/Molecular Layer Deposition*, *Scientific Reports*, **2018**, *8*, 8976.

132. Lausund, K. B. and Nilsen, O., *All-gas-phase synthesis of UiO-66 through modulated atomic layer deposition*, *Nature Communications*, **2016**, *7*, 13578.

133. Lausund, K. B., Petrovic, V. and Nilsen, O., *All-gas-phase synthesis of amino-functionalized UiO-66 thin films*, *Dalton Transactions*, **2017**, *46*, 16983-16992.

134. Ahvenniemi, E. and Karppinen, M., *In Situ Atomic/Molecular Layer-by-Layer Deposition of Inorganic–Organic Coordination Network Thin Films from Gaseous Precursors*, *Chemistry of Materials*, **2016**, *28*, 6260-6265.

135. Penttinen, J., Nisula, M. and Karppinen, M., *Atomic/Molecular Layer Deposition of s-Block Metal Carboxylate Coordination Network Thin Films*, *Chemistry – A European Journal*, **2017**, *23*, 18225-18231.

136. Nisula, M. and Karppinen, M., *Atomic/Molecular Layer Deposition of Lithium Terephthalate Thin Films as High Rate Capability Li-Ion Battery Anodes*, *Nano Letters*, **2016**, *16*, 1276-1281.

137. Stassen, I., Styles, M., Grenci, G., Van Gorp, H., Vanderlinden, W., De Feyter, S., Falcaro, P., De Vos, D., Vereecken, P. and Ameloot, R., *Chemical vapour deposition of zeolitic imidazolate framework thin films*, *Nature Materials*, **2015**, *15*, 304–310.

138. Theeten, J. and Aspnes, D., *Ellipsometry in thin film analysis*, *Annual Review of Materials Science*, **1981**, *11*, 97-122.

139. Sauerbrey, G., *Verwendung von Schwingquarzen zur Wägung dünner Schichten und zur Mikrowägung*, *Zeitschrift für Physik*, **1959**, *155*, 206-222.

140. Griffiths, P. R. and De Haseth, J. A., *Fourier transform infrared spectrometry*, John Wiley & Sons, Hoboken, New Jersey, USA, **2007**.

141. Birkholz, M., *Thin Film Analysis by X-Ray Scattering*, WILEY-VCH Verlag GmbH & Co. KGaA, Dramstadt, Germany, **2006**.

142. Daillant, J. and Gibaud, A., *X-ray and Neutron Reflectivity: Principles and Applications*, Springer, Berlin Heidelberg, **2009**.

143. Kazmiruk, V, *Scanning Electron Microscopy,* IntechOpen, **2012**.

144. McMullan, D., *Scanning electron microscopy 1928–1965*, *Scanning*, **1995**, *17*, 175-185.

145. Hunger, K., Mischke, P. and Rieper, W., *Surface and Thin-Film Analysis, 5. Scanning Probe Microscopy*, *Ullmann's Encyclopedia of Industrial Chemistry*, **2011**, DOI: doi:10.1002/14356007.o25_o11.

146. Yuan, Y. and Lee, T. R., in *Surface Science Techniques*, eds. Bracco, G. and Holst, B., Springer Berlin Heidelberg, Berlin, Heidelberg, **2013**, DOI: 10.1007/978-3-642-34243-1_1, pp. 3-34.

147. Kanngießer, B. and Wolff, N. L. R. W. H., *Handbook of practical X-Ray fluorescence analysis*, *Beckhoff, B., Kanngiesser, B., Langhoff, N., Wedell, R., Wolff, H., Eds*, **2006**, 433-474.

148. Coats, A. and Redfern, J., *Thermogravimetric analysis. A review*, *Analyst*, **1963**, *88*, 906-924.

149. Leus, K., Bogaerts, T., De Decker, J., Depauw, H., Hendrickx, K., Vrielinck, H., Van Speybroeck, V. and Van Der Voort, P., *Systematic study of the chemical and hydrothermal stability of selected "stable" Metal Organic Frameworks*, *Microporous and Mesoporous Materials*, **2016**, *226*, 110-116.

150. Xu, L., Luo, Y., Sun, L., Pu, S., Fang, M., Yuan, R.-X. and Du, H.-B., *Tuning the properties of the metal–organic framework UiO-67-bpy via post-synthetic N-quaternization of pyridine sites*, *Dalton Transactions*, **2016**, *45*, 8614-8621.

151. Dewar, M. J. S. and Schmeising, H. N., *Resonance and conjugation—II Factors determining bond lengths and heats of formation*, *Tetrahedron*, **1960**, *11*, 96-120.

152. Verpoort, F., Haemers, T., Roose, P. and Maes, J. P., *Characterization of a Surface Coating Formed from Carboxylic Acid-Based Coolants*, *Applied Spectroscopy*, **1999**, *53*, 1528-1534.

153. Cliffe, M. J., Castillo-Martínez, E., Wu, Y., Lee, J., Forse, A. C., Firth, F. C. N., Moghadam, P. Z., Fairen-Jimenez, D., Gaultois, M. W., Hill, J. A., Magdysyuk, O. V., Slater, B., Goodwin, A. L. and Grey, C. P., *Metal–Organic Nanosheets Formed via Defect-Mediated Transformation of a Hafnium Metal–Organic Framework*, *Journal of the American Chemical Society*, **2017**, *139*, 5397-5404.

154. Ermer, M., Mehler, J., Kriesten, M., Avadhut, Y., Schulz, P. S. and Hartmann, M., *Synthesis of the novel MOF hcp UiO-66 employing ionic liquids as linker precursors*, *Dalton Transactions*, **2018**.

155. Bon, V., Senkovska, I., Weiss, M. S. and Kaskel, S., *Tailoring of network dimensionality and porosity adjustment in Zr- and Hf-based MOFs*, *CrystEngComm*, **2013**, *15*, 9572-9577.

156. Walton, K. S. and Snurr, R. Q., *Applicability of the BET Method for Determining Surface Areas of Microporous Metal−Organic Frameworks*, *Journal of the American Chemical Society*, **2007**, *129*, 8552-8556.

157. Azad, F. N., Ghaedi, M., Dashtian, K., Hajati, S. and Pezeshkpour, V., *Ultrasonically assisted hydrothermal synthesis of activated carbon–HKUST-1-MOF hybrid for efficient simultaneous ultrasound-assisted removal of ternary organic dyes and antibacterial investigation: Taguchi optimization*, *Ultrasonics Sonochemistry*, **2016**, *31*, 383-393.

158. Bergh, V., Bruzell, E., Hegge, A. and Tønnesen, H., *Influence of formulation on photoinactivation of bacteria by lumichrome*, *Die Pharmazie-An International Journal of Pharmaceutical Sciences*, **2015**, *70*, 574-580.

159. Allen, C. A. and Cohen, S. M., *Near-UV photo-induced modification in isoreticular metal–organic frameworks*, *Journal of Materials Chemistry*, **2012**, *22*, 10188-10194.

160. Lan, H., Salmi, L. D., Rönkkö, T., Parshintsev, J., Jussila, M., Hartonen, K., Kemell, M. and Riekkola, M.-L., *Integrated atomic layer deposition and chemical vapor reaction for the preparation of metal organic framework coatings for solid-phase microextraction Arrow*, *Analytica Chimica Acta*, **2018**, *1024*, 93-100.

161. Zhao, J., Lee, D. T., Yaga, R. W., Hall, M. G., Barton, H. F., Woodward, I. R., Oldham, C. J., Walls, H. J., Peterson, G. W. and Parsons, G. N., *Ultra-Fast Degradation of Chemical Warfare Agents Using MOF–Nanofiber Kebabs*, *Angewandte Chemie*, **2016**, *55*, 13224-13228.

162. Hod, I., Bury, W., Karlin, D. M., Deria, P., Kung, C. W., Katz, M. J., So, M., Klahr, B., Jin, D. and Chung, Y. W., *Directed Growth of Electroactive Metal-Organic Framework Thin Films Using Electrophoretic Deposition*, *Advanced Materials*, **2014**, *26*, 6295-6300.

163. Uzarevic, K., Wang, T. C., Moon, S.-Y., Fidelli, A. M., Hupp, J. T., Farha, O. K. and Friscic, T., *Mechanochemical and solvent-free assembly of zirconium-based metal-organic frameworks*, *Chemical Communications*, **2016**, *52*, 2133-2136.

164. Keskiväli, L., Putkonen, M., Puhakka, E., Kenttä, E., Kint, J., Ramachandran, R. K., Detavernier, C. and Simell, P., *Molecular Layer Deposition Using Ring-Opening Reactions: Molecular Modeling of the Film Growth and the Effects of Hydrogen Peroxide*, *ACS Omega*, **2018**, *3*, 7141-7149.

Appendix

This appendix contains the three papers associated with this thesis:

Paper I: All-gas-phase synthesis of UiO-66 through modulated atomic layer deposition

Paper II: All-gas-phase synthesis of amino-functionalized UiO-66 thin films

Paper III: MOF thin films with bi-aromatic linkers by molecular layer deposition

along with their supplementary information.

I

Paper I

All-gas-phase synthesis of UiO-66 through modulated atomic layer deposition

K. B. Lausund and O. Nilsen, *Nature Communications*, 2016, **7**, 13578.

I

nature COMMUNICATIONS

ARTICLE

Received 9 Feb 2016 | Accepted 17 Oct 2016 | Published 23 Nov 2016

DOI: 10.1038/ncomms13578

OPEN

All-gas-phase synthesis of UiO-66 through modulated atomic layer deposition

Kristian Blindheim Lausund[1] & Ola Nilsen[1]

Thin films of stable metal-organic frameworks (MOFs) such as UiO-66 have enormous application potential, for instance in microelectronics. However, all-gas-phase deposition techniques are currently not available for such MOFs. We here report on thin-film deposition of the thermally and chemically stable UiO-66 in an all-gas-phase process by the aid of atomic layer deposition (ALD). Sequential reactions of $ZrCl_4$ and 1,4-benzenedicarboxylic acid produce amorphous organic–inorganic hybrid films that are subsequently crystallized to the UiO-66 structure by treatment in acetic acid vapour. We also introduce a new approach to control the stoichiometry between metal clusters and organic linkers by modulation of the ALD growth with additional acetic acid pulses. An all-gas-phase synthesis technique for UiO-66 could enable implementations in microelectronics that are not compatible with solvothermal synthesis. Since this technique is ALD-based, it could also give enhanced thickness control and the possibility to coat irregular substrates with high aspect ratios.

---

[1] Centre for Materials Science and Nanotechnology (SMN), Department of Chemistry, University of Oslo, P.O. Box 1033 Blindern, Oslo N-0315, Norway. Correspondence and requests for materials should be addressed to O.N. (email: ola.nilsen@kjemi.uio.no).

Metal-organic frameworks (MOFs) are a class of compounds combining both inorganic and organic functionalities. These crystalline materials typically have a porous framework with porosity exceeding that of the well-known zeolites[1]. The pores in crystalline MOFs are a part of their crystal structure, which results in an accurate pore size control. Thanks to the wide choice of inorganic and organic building units, the range of possible compounds is huge and only a fraction of these have been explored, especially with respect to characterization of their physical properties.

Due to their very high porosity, MOFs are promising for a number of applications such as gas storage[2], catalysis[3], drug delivery[4], handling and destruction of toxins[5–7], and as membranes for desalination[8]. Practical routes for deposition of thin and conformal films of porous materials will lead to many new applications, particularly within membrane development or within microelectronics for use as active material in highly sensitive gas sensors based on cantilevers or as low-κ dielectrics, as envisioned by Allendorf *et al.*[9].

Organic–inorganic hybrid materials have been deposited as thin films by atomic layer deposition (ALD) in a mode also known as molecular layer deposition (MLD)[10–12]. These films are typically amorphous and do not show the same properties as crystalline MOFs. ALD and MLD are techniques where two or more precursors are individually pulsed into a reaction chamber through the gas phase and allowed to react with, and saturate, the surface of a substrate. When the surface is saturated by the first precursor, excess precursor is removed by purging with an inert gas, and the process is repeated for the second precursor. A thin-film is constructed one atomic layer or one molecular layer at a time by reiterating these steps in a cyclic process[13].

To realize MOF applications within electronics and sensors, it is vital to develop synthesis routes that do not involve solvents, since these typically cause chemical contamination in the circuitry or stiction of small features. An all-gas-phase synthesis utilizing ALD/MLD of MOFs is therefore a highly suitable approach with very precise control of the amount of deposited material.

Possibilities for deposition of crystalline MOF thin films by vapour-phase techniques have recently emerged[14,15], opening the possibility of disruptive technologies due to the unique properties of these microporous crystalline materials. Suitable all-gas-phase processes are essential for enabling nanostructures of these compounds, as the stiction associated with wet-based techniques is avoided. The established MLD technique should be well suited for deposition of such microporous materials. However, sequential deposition makes it difficult to form the complex metal clusters found in MOF structures; instead giving amorphous structures without the required clusters. Even approaches using metal precursors providing suitable clusters in the gas phase[16] have required sequential wet-based hydrothermal treatment to crystallize in the desired structure.

One of the most stable MOFs is UiO-66. This zirconium-based MOF was discovered by Cavka *et al.*[17] in 2008. Thin films of this MOF would be particularly useful due to its stability in many chemical environments, which is why it was chosen for this work. There are very few other examples of synthesis of thin films of UiO-66 or solvent-free synthesis of bulk UiO-66 in literature, and no examples of thin-film deposition by all vapour-phase approaches. The prior examples of deposition of UiO-66 as thin films have been by electrophoretic deposition of pre-synthesized UiO-66 particles from a toluene suspension[18], electrochemical deposition[19] or by solvothermal growth[20]; and, to our knowledge, the only example of solvent-free synthesis of bulk UiO-66 was through mechanochemical synthesis[21].

We demonstrate a new approach utilizing a modulated MLD process where the metal-to-linker stoichiometry is controlled by modulating the process with an additional non-linker compound to construct the archetypical MOF material UiO-66 with high crystallinity. This approach opens up new possibilities in deposition of crystalline microporous materials with complex metal clusters. UiO-66 is deposited through application of $ZrCl_4$, and 1,4-benzenedicarboxylic acid (1,4-BDC, also known as terephthalic acid) as the organic linker.

Results

Deposition of hybrid films without modulation. The $ZrCl_4 + $1,4-BDC system was initially investigated using the *in situ* quartz-crystal microbalance (QCM) technique for a deposition temperature of 265 °C. The typical sensor response for growth using the sequence of a 4 s $ZrCl_4$ pulse, 6 s purge, 5 s 1,4-BDC pulse and 6 s purge is shown in Fig. 1. This pulsing sequence was used as a standard sequence throughout the QCM experiments, if not stated otherwise. The pulsing sequence showed self-limiting growth for both types of precursors, as can be seen in Fig. 2. The mass increase per precursor sums to 42.3% for the $ZrCl_4$ pulse and 57.7% for the 1,4-BDC precursor. This corresponds well with a relative mass increase of 178.35 g mol^{-1} during the $ZrCl_4$ pulse and 241.11 g mol^{-1} during the 1,4-BDC pulse, obtained from an average reaction scheme of:

$$\begin{aligned}&ZrCl_4\ \text{pulse:}\\&|-(OH)_{1.5} + ZrCl_4(g) = |-O_{1.5}ZrCl_{2.5} + 1.5\ HCl\ (g)\end{aligned} \tag{1}$$

$$\begin{aligned}&1,4\text{-BDC pulse:}\\&|-O_{1.5}ZrCl_{2.5} + 2C_6H_4(COOH)_2(g) = |-O_{1.5}Zr(C_6H_4O_{3.25})_2(OH)_{1.5} + 2.5\,HCl\ (g)\end{aligned} \tag{2}$$

The pulse/purge system was also investigated by QCM based on the growth as averaged over 16 cycles when changing the individual pulse or purge parameters of the 4-6-5-6 standard sequence for two sensors situated 5 cm apart along the direction of the gas stream (Fig. 2). This experiment was repeated twice. The reactions were self-saturating and delayed saturation of $ZrCl_4$ along the flow stream was found based on our dual-QCM sensor approach, as can be seen from the lower growth rate in the back of the chamber with pulse lengths of 0.75, 1 and 2 s; this is to a certain degree also seen for 1,4-BDC since the growth rate is lower in the back of the chamber with 0.25 and 0.5 s pulses (Fig. 2a,c). The standard pulsing scheme of 4-6-5-6 is well within ALD-type growth conditions.

The growth of the $ZrCl_4 + $1,4-BDC system was investigated as a function of deposition temperature (Fig. 3a). A number of

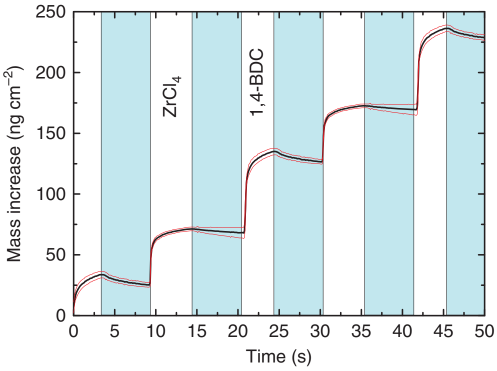

Figure 1 | QCM characterization. Mass gain as a function of time measured with QCM for the ALD/MLD system with alternating $ZrCl_4$ and terephthalic acid (1,4-BDC) pulses separated by inert gas (N_2) purges (blue). The red lines show the s.d. for the QCM data ($n = 16$).

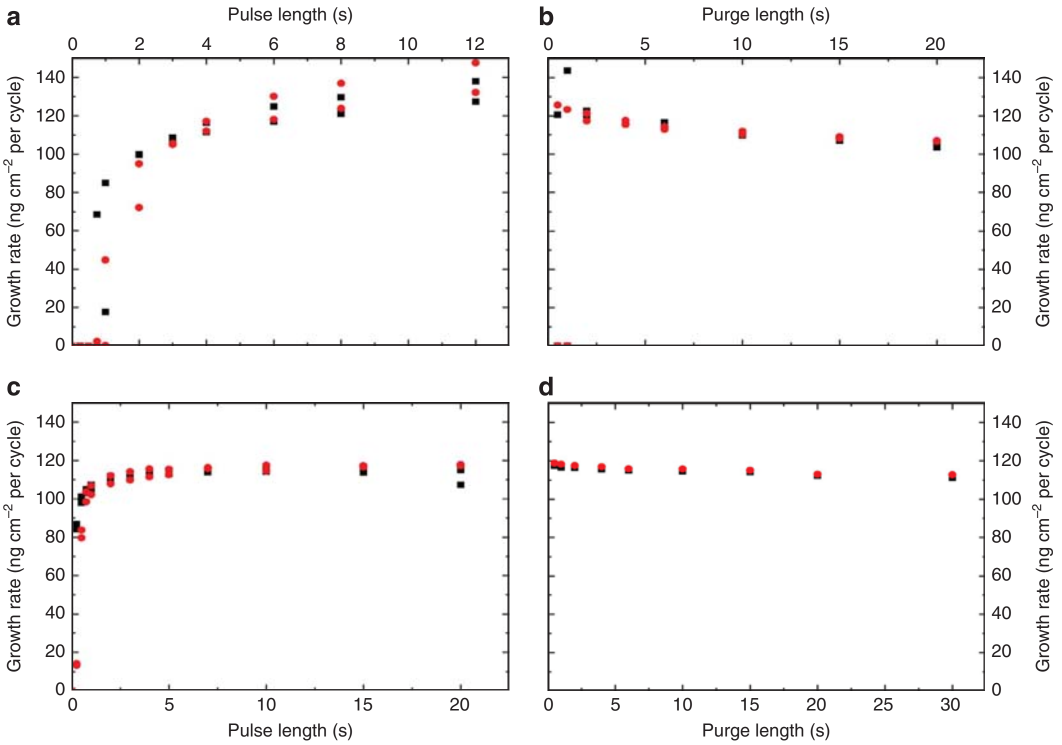

Figure 2 | Test of self-saturated growth. The growth rate for the system in Fig. 1 as a function of lengths of the $ZrCl_4$ pulse (**a**), the $ZrCl_4$ purge (**b**), the 1,4-BDC pulse (**c**) and the 1,4-BDC purge (**d**). Two sensors were used, one in the front of the reaction chamber (black square), and one in the back (red dot), situated ca. 5 cm apart. The experiment was repeated twice with the same sensors.

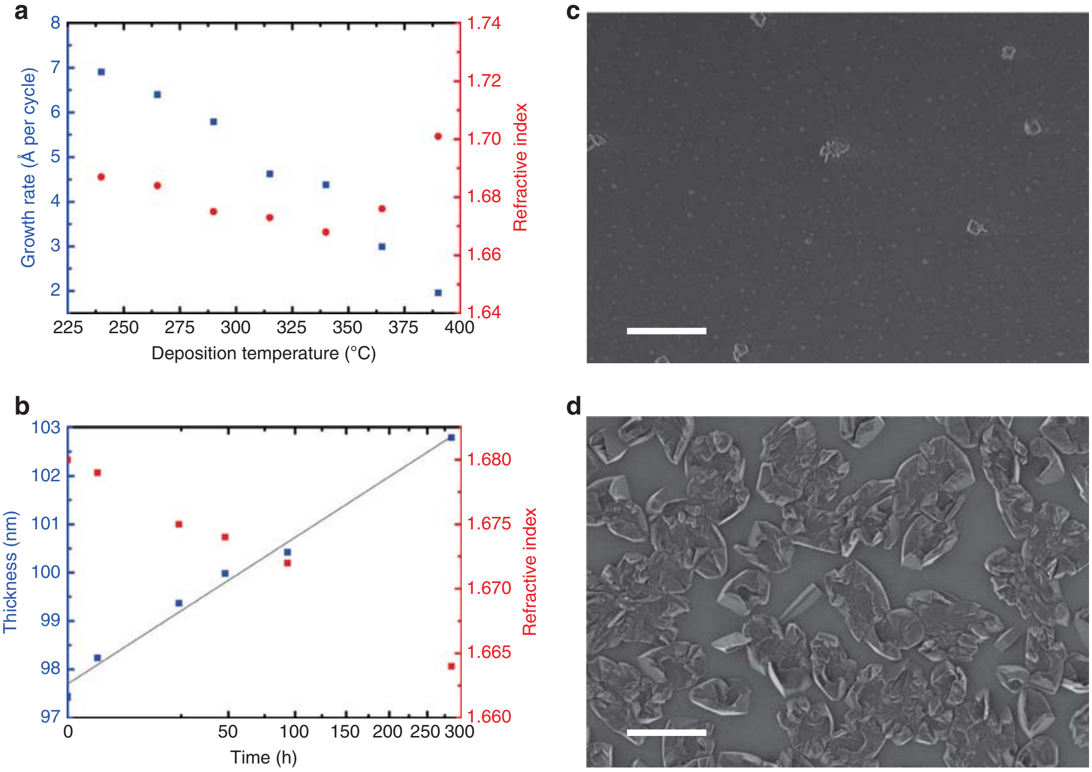

Figure 3 | Effects of deposition temperature and storage conditions. (**a**) Growth rate and refractive index of the $ZrCl_4$ + 1,4-BDC system as function of the deposition temperature. (**b**) Thickness and refractive index as a function of storage time with a square root dependency on the time scale. (**c**,**d**) show SEM images of a 130 nm film deposited at 265 °C before and after exposure to moisture, respectively. Scale bar, 2 μm.

depositions were made with 143 cycles of 4 s $ZrCl_4$ pulse, 2 s purge, 3 s 1,4-BDC pulse and 1 s purge, and increasing reactor temperature from 235 to 390 °C. The growth rate decreases with increasing temperature from 7 to 2 Å cycle^{-1}, and the refractive index shows a slight reduction between 235 and 335 °C, and then undergoes a significant increase.

A sample stored in air was characterized by spectroscopic ellipsometry (SE) over time to identify its environmental stability (Fig. 3b). The film thickness increased as a function of the square root of the time. Coherently, the refractive index was reduced from 1.680 to 1.664.

The increase in thickness over time is most likely due to a reaction with moisture from the air. A selection of the samples was exposed to a moist environment with a relative humidity of 70–75% at room temperature for 24 h. This resulted in an increase in thickness of ca. 20% and a drastic change in topography, as can be seen from the scanning electron microscope (SEM) images in Fig. 3d. Judged by the SEM image in Fig. 3c the as-deposited films are rather smooth. This is also confirmed by X-ray reflectometry (XRR) analysis, where we see a roughness of 0.3 nm on a 30.9-nm thick film.

Grazing incidence X-ray diffraction analyses of the films before and after exposure to a moist environment, which are presented later in the results section, indicate that some of the 1,4-BDC precursor crystallized on the surface of the films. This is most likely due to subsequent reactions between parts of the 1,4-BDC that are not optimally bonded to the Zr clusters.

Deposition of hybrid films with water pulsing. Within the same QCM experiment as mentioned above, four different pulsing schemes in which H_2O was pulsed in addition to the two precursors were investigated to see what effect this would have on the films. One of these pulsing schemes is shown in Fig. 4. For all systems, it is evident that pulsing water causes a large mass increase that is mostly lost in the subsequent purge. This is most likely due to adsorption (followed by desorption) of water and may indicate that the film is porous to small molecules like water during deposition. This corresponds well with the porosity test performed on amorphous films, which is presented towards the end of the results section. In addition to the loss of water during the purge, there is probably also a slight reduction of the amount of 1,4-BDC in the film during the water pulse, which is concealed by the mass increase from the water uptake. This is shown by Fourier transform infrared (FTIR) spectroscopy, where we see that the peak corresponding to 1,4-BDC in monodentate coordination is lost in a manner similar to the effect of modulation with acetic acid, which will be discussed in the next section (Supplementary Fig. 1a). Our theory that this poorly bonded 1,4-BDC is removed from the film when water is pulsed is further supported by the fact that 1,4-BDC no longer crystallizes on the surface when the films deposited with H_2O pulsing are exposed to a 70–75% relative humidity over 24 h as seen by GI X-ray diffraction (Supplementary Fig. 1b). GI X-ray diffraction of a film deposited with additional water pulses also shows that the crystallinity of the films is not affected by the water pulse in that they remain amorphous as-deposited. However, the ratio of Cl to Zr is reduced from 3.2 to 0.1 wt% compared with an as-deposited film with a pulse sequence of 4 s $ZrCl_4$ pulse, 2 s purge, 3 s 1,4-BDC pulse and 1 s purge. This loss in chlorine may also contribute to a mass loss during the water pulse.

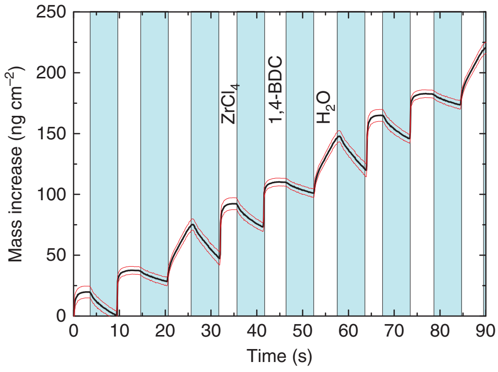

Figure 4 | Deposition of hybrid film with H_2O. Mass gain as a function of time measured with QCM for the ALD/MLD system with $ZrCl_4$, 1,4-BDC and H_2O. The blue panels indicate inert gas (N_2) purging. The red lines show the standard deviations for the QCM data ($n = 16$).

Due to the porous nature of these films and the fact that the desorption of water from the films seems to be a relatively slow process, it is possible that the film acts as a reservoir for water allowing some water to come in contact with $ZrCl_4$ during the next pulse causing unwanted reactions. This can be seen from the QCM graph in Fig. 4. The mass loss during the purge following the water pulse seems to carry over to the purges following the $ZrCl_4$ and 1,4-BDC pulses indicating that water is still leaving the film while $ZrCl_4$ is pulsed. Because of this we have chosen not to go further with this approach.

Deposition of hybrid films with acetic acid modulation. As mentioned above, GI X-ray diffraction analyses indicate that some of the 1,4-BDC precursor crystallized on the surface of samples deposited without modulation when exposed to a relative humidity of 70–75% over 24 h (Fig. 5). An attempt was made to reduce this excess of 1,4-BDC in the film by introducing additional pulses of acetic acid after 1,4-BDC in the deposition process. Acetic acid has previously been used as a modulator in MOF synthesis, and the hypothesis is that it may replace some of the 1,4-BDC that is not optimally bonded to the surface during its pulse[20,22]. The growth dynamics were investigated by QCM, which shows a notable reduction in mass increase when acetic acid is pulsed (Fig. 5a). Adding the acetic acid pulse does not affect the overall growth rate in terms of mass increase per cycle, as compared with the growth in Fig. 1. Both systems show an overall growth rate of ca. 100.8 ng cm^{-2} cycle^{-1}. The mass increase for the $ZrCl_4$ is increased by 55% as compared with the process without acetic acid. By assuming that no acetic acid is included in the film during growth, as supported by the FTIR characterization presented in the end of the 'Results' section, the overall growth scheme assumes a 66% mass increase for the $ZrCl_4$ pulse and the remaining 34% during the 1,4-BDC + acetic acid pulse. This mass variation cannot be described by the reaction scheme in equation (1) and (2), which assumes an overall stoichiometry of $Zr(1,4\text{-}BDC)_2$, while UiO-66 has a 1:1 stoichiometry between Zr and 1,4-BDC using $Zr_6O_4(OH)_4^{12+}$ clusters bonded to 12 $-COO^-$ functional groups. On this basis it is possible to sketch a reaction scheme according to:

$$\begin{gathered}\mathrm{ZrCl_4\ pulse:}\\ |-(\mathrm{OH})_{1.75}+\mathrm{ZrCl_4(g)}=|-\mathrm{O_{1.75}ZrCl_{2.25}}+1.75\,\mathrm{HCl\ (g)}\end{gathered} \tag{3}$$

$$\begin{gathered}\mathrm{1,4\text{-}BDC\ pulse:}\\ |-\mathrm{O_{1.75}ZrCl_{2.25}}+\mathrm{C_6H_4(COOH)_2(g)}=|-\mathrm{O_{1.75}Zr(C_6H_4O_{2.25})(OH)_{1.75}}+2.25\mathrm{HCl\ (g)}\end{gathered} \tag{4}$$

With a relative mass increase of 169.23 g mol^{-1} and 84.10 g mol^{-1} for the $ZrCl_4$ and 1,4-BDC pulses, respectively. This reaction scheme does not explain or take into account formation of the Zr clusters or the occurrence of the additional

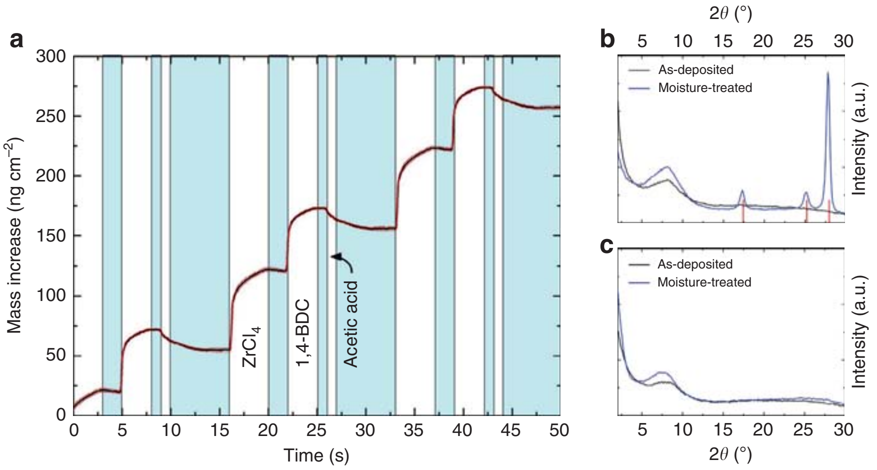

Figure 5 | Effects of acetic acid modulation on the ALD process. (**a**) QCM measurements showing mass increase (and loss) as the precursors and the modulator are pulsed. The blue panels indicate inert gas (N_2) purging. The red lines show the standard deviations for the QCM data ($n = 16$). (**b**,**c**) show GI X-ray diffractograms for the films that were deposited without and with acetic acid modulation, respectively. The black lines show the as-deposited samples, and the blue lines are the moisture-treated samples. Positions for reflections of the crystalline 1,4-BDC phase of more than 10% intensity are given by the red vertical lines in **b** (ref. 23).

O^{2-} or OH^-. We can at this stage only assume that they are added through the subsequent reactions with air and acetic acid in the sealed autoclave or during handling before this treatment. This remains to be investigated with more dedicated techniques.

The films that were deposited with additional pulses of acetic acid were also exposed to moisture after deposition. The GI X-ray diffractogram of the moisture-treated sample no longer shows reflections corresponding to crystals of 1,4-BDC (Fig. 5c). This indicates that there is probably no longer an excess of 1,4-BDC in the films and that a more optimal growth is obtained when acetic acid is used.

Crystallization and characterization of the films. Several different attempts were made to induce crystallization of the deposited films. One approach was treatment under solvothermal conditions after deposition. Water and dimethylformamide were used as solvents, and different configurations were tested where the film was either submerged in the solvent or supported above it to avoid direct contact. These solvothermal treatments showed a varying degree of crystallinity but they all lacked strong XRD reflections at 2θ below 10 degrees, which would indicate crystalline UiO-66.

In addition to the solvothermal treatments, a film made with acetic acid modulation was placed in an autoclave with ~0.1 ml of acetic acid, sealed and heated to 160 °C for 24 h, essentially heating the film in acetic acid vapour (Fig. 6a).

This treatment resulted in a film with a very similar GI X-ray diffractogram to the ref. 17 for UiO-66 (Fig. 7). The thickness of the film increased from 229 nm as-deposited to ~500 nm as can be seen from the cross-section SEM image in the inset in Fig. 6b. The treatment also roughened the surface giving a root mean squared roughness of ~45 nm, as measured by atomic force microscopy (AFM). This roughness prevented XRR measurements on the treated samples (Fig. 6b,c).

A similar autoclave treatment without acetic acid in the autoclave was also performed on a sample deposited without acetic acid modulation. The resulting film was promising, as the GI X-ray diffractogram showed reflections corresponding to crystalline UiO-66, albeit with lower intensity than when acetic acid was added in the autoclave. This sample was deposited without acetic modulation, so 1,4-BDC also crystallized on the surface.

Since XRR measurements could not be used to determine the density of the post-deposition-treated samples, a porosity test was done using QCM measurements. Two QCM-crystals were coated with 500 cycles of ZrCl4, 1,4-BDC and acetic acid for modulation, which should give a film thickness of ~230 nm. One of these crystals was then treated in the autoclave as described above. The QCM-crystals with as-deposited and post-deposition-treated films were exposed to a 5-s long water vapour pulse in the ALD reactor to determine the water uptake. The test was done at room temperature with a base pressure of ~5 mbar N_2. The same procedure was also done to two uncoated crystals as a control. The results show a response over 200 times higher from the post-deposition-treated sample compared with the uncoated crystals. The as-deposited sample also shows a high response, which is delayed as compared with the post-deposition-treated sample (Fig. 8). Given a sufficiently long water pulse, both samples show similar saturation values (Supplementary Fig. 2a); and with a sufficiently long purge, the water uptake is completely lost (Supplementary Fig. 2b). This indicates that both the amorphous (as-deposited sample) and the crystalline (post deposition treated sample) are porous, but that the pores in the treated sample are much more accessible. By comparing the mass increase during the water pulse (found from Supplementary Fig. 2a) with the total mass gain during the deposition (49,594 ng cm^{-2}) of the post-deposition-treated film we see that the water uptake in the film is ~1.9 wt%. This is at a relative humidity in the ALD chamber of ~7% (found by measuring a 2.2 mbar pressure increase in the chamber during the water pulse, which corresponds to the partial pressure of water, and converting this to relative humidity). For comparison, Schoenecker *et al.*[24] present a water uptake in UiO-66 of ~2 wt% with a relative humidity in this range. FTIR measurements were done of a modulated, as-deposited sample before and after exposure to water, to ensure that the water pulse during the porosity test does not affect the composition of the film, but no change was seen (Supplementary Fig. 3).

FTIR spectroscopy was performed on samples deposited with and without acetic acid modulation, and a modulated sample that in addition was heated in an autoclave in acetic acid vapour

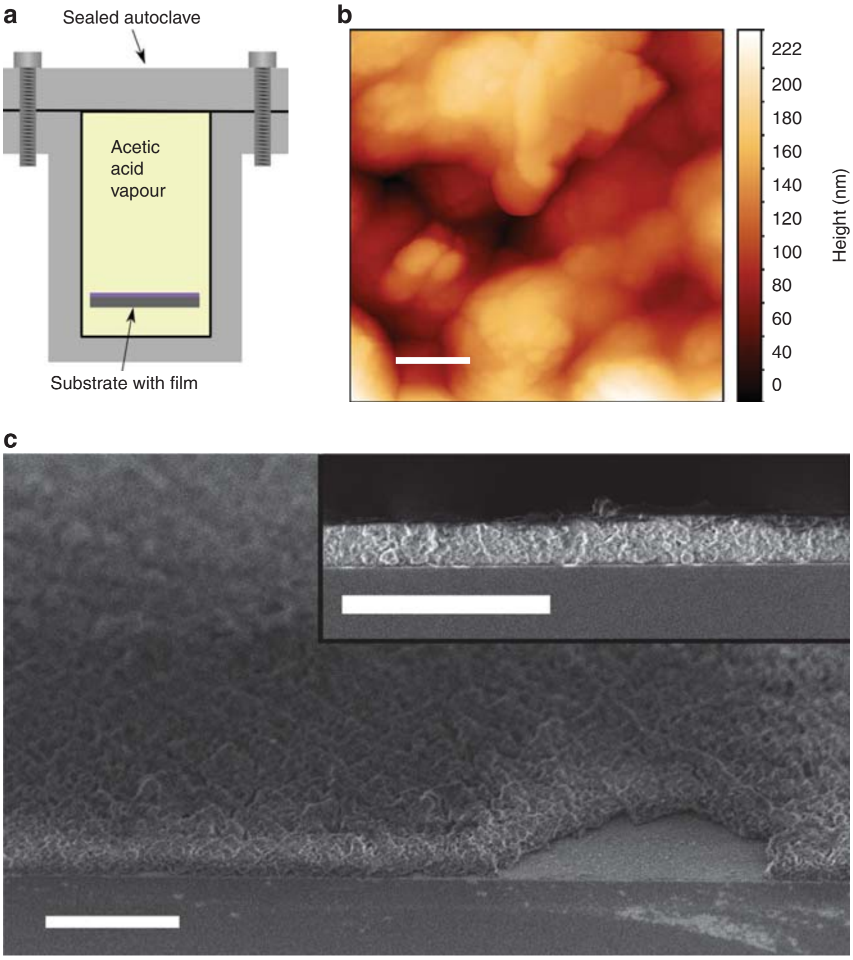

Figure 6 | Post-deposition crystallization. (**a**) Experimental setup for heat treatment of the films in acetic acid vapour. (**b**) AFM image of the Zr-1,4-BDC film after treatment in acetic acid vapour. (**c**) Cross-section SEM images of the same surface viewed at 45° and 90° angles. Scale bar, 0.2 µm (**b**), 2 µm (**c**).

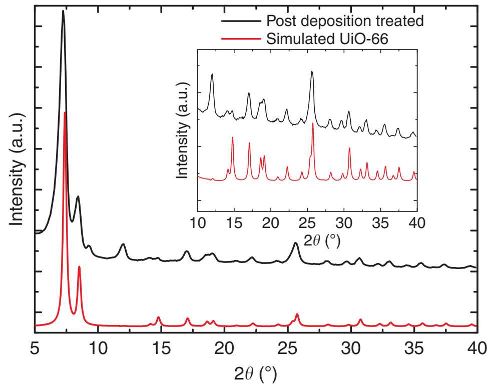

Figure 7 | GI X-ray diffraction on crystallized film. GI X-ray diffractogram for a film that was heated to 160 °C in acetic acid vapour in a sealed autoclave for 24 h (black) and a simulated powder diffractogram for desolvated UiO-66 (red); the inset shows the same diffractograms zoomed in on peaks with 2θ between 10 and 40 degrees.

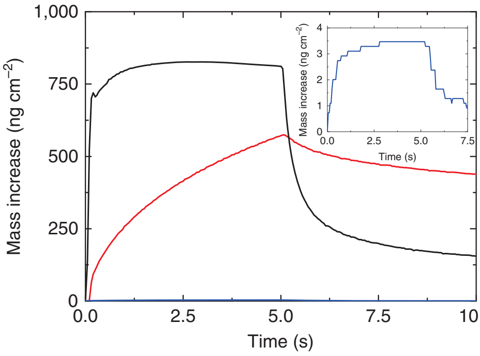

Figure 8 | Porosity test. Porosity test performed by monitoring the water uptake by QCM-crystals during a 5 s water pulse. The test was performed in the ALD reactor at room temperature with a base pressure of 5 mbar N_2. Red is the as-deposited sample (ca. 230 nm), black is the post-deposition-treated sample (ca. 500 nm), and blue is the average of the two uncoated QCM-crystals as a control. The inset shows the control enlarged.

(Fig. 9d). According to Verpoort *et al.*[25], the wave number separations between the most prominent peaks around 1,400 cm^{-1} and 1,500–1,700 cm^{-1} can reveal information on the coordination modes of 1,4-BDC to zirconium (Fig. 9a–c). These two peaks correspond to the symmetric and asymmetric stretches of the carboxylate group, respectively. The splitting is larger than 200 cm^{-1} when the 1,4-BDC molecule acts as a monodentate ligand, and in the range of 50–150 cm^{-1} if it acts as a bidentate ligand. A splitting of 130–200 cm^{-1} is expected for bridging ligands (Fig. 9). The amount of splitting observed by

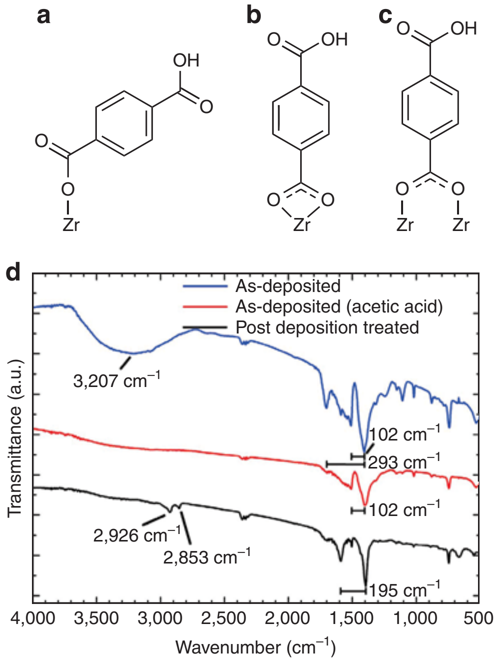

Figure 9 | Infrared spectroscopy. (**a**–**c**) show the possible coordination modes of 1,4-BDC to zirconium. **a** is monodentate, **b** is bidentate and **c** is bridging. (**d**) The FTIR spectra for as-deposited samples with and without acetic acid modulation and a post-deposition-treated modulated sample. The splitting between the major peaks and values of selected peaks are noted.

FTIR is shown in Fig. 9d. This shows that acetic acid modulation removes monodentate 1,4-BDC molecules, leaving only the ones with a bidentate coordination. It can also be seen that the post-deposition treatment changes the coordination from bidentate to bridging, which agrees with the UiO-66 structure.

Discussion

The *in situ* QCM investigations of the ALD/MLD sequence with ZrCl$_4$ and 1,4-BDC as precursors show a self-terminating growth manner for the pure hybrid film (Fig. 2). The growth rate is ∼6–7 Å cycle^{-1} with a reaction temperature of 265 °C, which is notably higher than normal ALD-processes, but within what is expected for an ALD/MLD process. The hybrid films show very little surface roughness as-deposited, which is as expected for growth of amorphous films (Fig. 3c). When exposed to moisture, the thickness of the films increases along with a considerable change in topography (Fig. 3b–d). During this process, pure 1,4-BDC crystallizes on the surface as shown by the GI X-ray diffractograms in Fig. 5b. Such crystallization of 1,4-BDC was prevented when additional pulses of acetic acid were introduced after the 1,4-BDC pulses. The overall growth rates for these two pulsing schemes resulted in identical values in terms of mass per area, although the relative mass change between ZrCl$_4$ and 1,4-BDC indicates a clear change in stoichiometry towards more equiatomic composition. The physical growth rates for the pulsing schemes without and with acetic acid were 8.3 Å cycle^{-1} and 4.6 Å cycle^{-1}, respectively, indicating an increase in overall density when modulation is introduced. This has also been confirmed by XRR and can be understood by the FTIR analysis of the films proving a transition of the bonding scheme from both monodentate and bidentate ligands for films deposited without acetic acid, to only bidentate coordination when acetic acid is used. It is possible that purely bidentate coordination yields straight columns of zirconium and 1,4-BDC linkers that orientate in a more dense manner than for a combination of bidentate and monodentate coordination, where an angled coordination between 1,4-BDC and zirconium is expected. From both the GI X-ray diffractograms and the FTIR results we can see that UiO-66 is not nucleated until it is treated with acetic acid vapour in an autoclave.

The films were crystallized by heating to 160 °C for 24 h in a sealed autoclave with ∼0.1 ml of acetic acid. The resulting GI X-ray diffractograms show an almost identical pattern to the X-ray diffractograms for UiO-66. The coordination also changed from bidentate to bridging, which corresponds to the coordination environment in the UiO-66 structure. This may indicate that the addition of acetic acid during deposition aids the overall composition, while proper crystallization of the UiO-66 phase does not occur before higher concentrations of acetic acid are used in the autoclave treatment. The FTIR spectrum for the as-deposited film also shows a broad peak at 3,207 cm^{-1}, which is possibly due to OH groups on monodentate 1,4-BDC molecules that are poorly bonded and have only coordinated to Zr on one side leaving the other carboxylic group protonated. We also see two peaks at 2,926 and 2,853 cm^{-1} for the post-deposition-treated sample. This may indicate that there is some acetic acid left in the structure after the autoclave treatment. These peaks are not observed in the sample deposited with acetic acid, which indicates that no acetic acid is left in the structure after the ALD/MLD deposition.

In summary, an all-gas-phase deposition technique for porous, crystalline UiO-66 has been developed through a combination of modulated ALD and additional exposure to acetic acid vapour. The films deposited without acetic acid modulation show an excess of 1,4-BDC, but when acetic acid pulsing is used during deposition this no longer is the case. The films are amorphous as-deposited but crystallize to the UiO-66 structure on treatment in acetic acid vapour. This synthesis method has substantial advantages compared with normal MOF synthesis since thin films of UiO-66 now can be implemented in microelectronics otherwise not compatible with wet-based processing. The importance of this was also exemplified by Stassen *et al.*[14], who developed a synthesis route for the MOF ZIF-8 by allowing dense zinc oxide to react with vapours of the organic linker molecule. UiO-66 has superb thermal and chemical stabilities compared with other MOF materials, and is thus ideal both as a model material and for implementation in real applications. To the best of our knowledge, no all-gas-phase synthesis technique for UiO-66 thin films has been reported before this work. This method benefits from all the advantages of ALD, for example, great thickness control even on irregular substrates with high aspect ratios. This is also a good example of a modulator being used directly in the ALD sequence for MOF synthesis. Previously, inhibitors have been used in the ALD sequence to reduce and distribute the amount of precursor embedded as dopant material[26,27]. Our approach leads to a technique for controlling the composition of MLD materials to form crystalline MOF structures, which has, until now, been difficult. This could enable a wider selection of MOF materials to be deposited by all-gas-phase approaches in the future.

Methods

Atomic/molecular layer deposition. The ALD/MLD depositions were performed in an F-120 Sat-type ALD reactor (ASM Microchemistry Ltd) using ZrCl$_4$ (MERCK Schuchardt OHG >98%) and 1,4-BDC(MERCK Schuchardt OHG ≥98%) as precursors. Type 2 water and acetic acid (MERCK KGaA 100%) were also used as co-reactants in selected experiments. The carrier and purging gas was N$_2$ separated from air in a nitrogen generator (Schmidlin UHPN3001 N$_2$ purifier, >99.999% N$_2$ + Ar purity). A total flow of ca. 250 sccm (standard cubic cm min^{-1}) of N_2 was used throughout the experiments, leading to a background pressure of ca. 5 mBar. The vapourization temperatures for $ZrCl_4$ and 1,4-BDC were set to 165 and 220 °C, respectively, based on previous investigations[11,28]. Water and acetic acid were kept at room temperature in external containers. The films were deposited on as-received, pre-cleaned Si(001) substrates of 2×2 cm^2. Their native oxide thickness was measured by SE before deposition and taken into account when the film thickness was determined.

Spectroscopic ellipsometry. SE data were collected using a J.A. Woollam alpha-SE spectroscopic ellipsometer using a wavelength range of 390–900 nm, and modelled to a Cauchy-function using the CompleteEASE software package to determine the thicknesses and refractive indices (at $\lambda = 632.8$ nm) of the films.

***In situ* QCM.** *In situ* QCM analyses were performed using two 6 MHz AT cut quartz crystals mounted ca. 5 cm apart on a home-made holder to monitor the mass increase during the deposition and uncover possible delayed saturations through the reaction chamber. The signals were recorded using a Maxtek TM-400 and processed by averaging over 16 consecutive cycles. The signal from the QCM analysis was converted from $-\Delta$Hz to ng cm^{-2} by calibrating the sensitivity of each sensor with the thickness and density data measured by XRR of films deposited separately from the QCM measurements. Variations in sensitivity of the sensors throughout the QCM experiment were also corrected for by using a standard sequence repeatedly throughout the experiment and adjusting all results based on variations in this standard. To ensure a reliable response from the QCM-crystals, the temperature was stabilised for 3 h before any experiments were performed.

Post-deposition treatment. Some of the films were exposed to moisture for 24 h in a chamber which was held at a relative humidity of 70–75% by storing a saturated NaCl solution in the chamber. Crystallization of the films was performed by heating the samples to 160 °C for 24 h in a sealed autoclave with an internal volume of 35 ml with ~0.1 ml of acetic acid added.

X-ray characterizations. GI X-ray diffraction and XRR analyses were performed using a PANalytical Empyrean diffractometer, equipped with a Cu Kα source powered at 45 kV/40 mA ($\lambda = 1.5406$ Å), a parallel beam X-ray mirror and a proportional point detector (PW 3011/20). For GI X-ray diffraction the incident angle was $\omega = 0.30°$, while for XRR analysis 2θ was scanned from 0.08° to 6°. The XRR results were analysed using the X'Pert Reflectivity software provided by PANalytical. X-ray fluorescence was performed on a PANalytical Axios mAX minerals instrument, and analysed using the Stratos software.

Infrared spectroscopy. FTIR spectroscopy was performed using a Bruker VERTEX 80 FTIR spectrometer in transmission mode. A spectrum obtained from an uncoated silicon substrate was used as background.

Electron microscopy. SEM images were obtained using a HITACHI SU8230 SEM with a cold cathode field emission type electron gun. The working distance was ~2 mm, and the acceleration voltage was typically 1 kV with a beam current of 10 μA.

Atomic force microscopy. AFM and roughness measurements were performed using a Park Systems XE-70 AFM equipped with a standard NCHR tip. Data were analysed using the Gwyddion 2.43 SPM visualization tool[29].

Simulation. The simulation of the XRD diffractogram for UiO-66 was done using Mercury[30] based on the data from the paper by Valenzano *et al.*[31].

Data availability. The data that support the findings of this study are available from the corresponding author on request.

References

1. Li, H., Eddaoudi, M., O'Keeffe, M. & Yaghi, O. M. Design and synthesis of an exceptionally stable and highly porous metal-organic framework. *Nature* **402,** 276–279 (1999).
2. Abid, H. R. *et al.* Nanosize Zr-metal organic framework (UiO-66) for hydrogen and carbon dioxide storage. *Chem. Eng. J.* **187,** 415–420 (2012).
3. Lee, J. *et al.* Metal-organic framework materials as catalysts. *Chem. Soc. Rev.* **38,** 1450–1459 (2009).
4. Taylor-Pashow, K. M. L., Rocca, J. D., Xie, Z., Tran, S. & Lin, W. Postsynthetic modifications of iron-carboxylate nanoscale metal – organic frameworks for imaging and drug delivery. *J. Am. Chem. Soc.* **131,** 14261–14263 (2009).
5. Jakobsen, S. *et al.* Structural determination of a highly stable metal-organic framework with possible application to interim radioactive waste scavenging: Hf-UiO-66. *Phys. Rev. B* **86,** 125429 (2012).
6. Wang, C., Liu, X., Chen, J. P. & Li, K. Superior removal of arsenic from water with zirconium metal-organic framework UiO-66. *Sci. Rep.* **5,** 16613 (2015).
7. Mondloch, J. E. *et al.* Destruction of chemical warfare agents using metal–organic frameworks. *Nat. Mater.* **14,** 512–516 (2015).
8. Liu, X., Keser Demir, N., Wu, Z. & Li, K. Highly water stable zirconium metal-organic framework UiO-66 membranes supported on alumina hollow fibers for desalination. *J. Am. Chem. Soc.* **137,** 6999–7002 (2015).
9. Allendorf, M. D., Schwartzberg, A., Stavila, V. & Talin, A. A. A Roadmap to implementing metal–organic frameworks in electronic devices: challenges and critical directions. *Chem. Eur. J.* **17,** 11372–11388 (2011).
10. Nilsen, O., Klepper, K., Nielsen, H. & Fjellvaåg, H. Deposition of organic-inorganic hybrid materials by atomic layer deposition. *ECS Trans.* **16,** 3–14 (2008).
11. Klepper, K. B., Nilsen, O. & Fjellvag, H. Deposition of thin films of organic-inorganic hybrid materials based on aromatic carboxylic acids by atomic layer deposition. *Dalton Trans.* **39,** 11628–11635 (2010).
12. Sundberg, P. & Karppinen, M. Organic and inorganic–organic thin film structures by molecular layer deposition: a review. *Beilstein J. Nanotechnol.* **5,** 1104–1136 (2014).
13. Miikkulainen, V., Leskelä, M., Ritala, M. & Puurunen, R. L. Crystallinity of inorganic films grown by atomic layer deposition: overview and general trends. *J. Appl. Phys.* **113,** 021301 (2013).
14. Stassen, I. *et al.* Chemical vapour deposition of zeolitic imidazolate framework thin films. *Nat. Mater.* **15,** 304–310 (2016).
15. Ahvenniemi, E. & Karppinen, M. Atomic/molecular layer deposition: a direct gas-phase route to crystalline metal–organic framework thin films. *Chem. Commun.* **52,** 1139–1142 (2016).
16. Salmi, L. D. *et al.* Studies on atomic layer deposition of MOF-5 thin films. *Micropor. Mesopor. Mater.* **182,** 147–154 (2013).
17. Cavka, J. H. *et al.* A new zirconium inorganic building brick forming metal organic frameworks with exceptional stability. *J. Am. Chem. Soc.* **130,** 13850–13851 (2008).
18. Hod, I. *et al.* Directed growth of electroactive metal-organic framework thin films using electrophoretic deposition. *Adv. Mater.* **26,** 6295–6300 (2014).
19. Stassen, I. *et al.* Electrochemical film deposition of the zirconium metal–organic framework UiO-66 and application in a miniaturized sorbent trap. *Chem. Mater.* **27,** 1801–1807 (2015).
20. Miyamoto, M., Kohmura, S., Iwatsuka, H., Oumi, Y. & Uemiya, S. *In situ* solvothermal growth of highly oriented Zr-based metal organic framework UiO-66 film with monocrystalline layer. *Cryst. Eng. Comm.* **17,** 3422–3425 (2015).
21. Uzarevic, K. *et al.* Mechanochemical and solvent-free assembly of zirconium-based metal-organic frameworks. *Chem. Commun.* **52,** 2133–2136 (2016).
22. Schaate, A. *et al.* Modulated synthesis of Zr-based metal–organic frameworks: from nano to single crystals. *Chem. Eur. J.* **17,** 6643–6651 (2011).
23. Bailey, M. & Brown, C. J. The crystal structure of terephthalic acid. *Acta Crystallogr.* **22,** 387–391 (1967).
24. Schoenecker, P. M., Carson, C. G., Jasuja, H., Flemming, C. J. J. & Walton, K. S. Effect of water adsorption on retention of structure and surface area of metal–organic frameworks. *Ind. Eng. Chem. Res.* **51,** 6513–6519 (2012).
25. Verpoort, F., Haemers, T., Roose, P. & Maes, J. P. Characterization of a surface coating formed from carboxylic acid-based coolants. *Appl. Spectrosc.* **53,** 1528–1534 (1999).
26. Yanguas-Gil, A., Libera, J. A. & Elam, J. W. Modulation of the growth per cycle in atomic layer deposition using reversible surface functionalization. *Chem. Mater.* **25,** 4849–4860 (2013).
27. Yanguas-Gil, A., Peterson, K. E. & Elam, J. W. Controlled dopant distribution and higher doping efficiencies by surface-functionalized atomic layer deposition. *Chem. Mater.* **23,** 4295–4297 (2011).
28. Rahtu, A. & Ritala, M. Reaction mechanism studies on the zirconium chloride–water atomic layer deposition process. *J. Mater. Chem.* **12,** 1484–1489 (2002).
29. Nečas, D. & Klapetek, P. Gwyddion: an open-source software for SPM data analysis. *Open Phys.* **10,** 181–188 (2012).
30. Macrae, C. F. *et al.* Mercury CSD 2.0—new features for the visualization and investigation of crystal structures. *J. Appl. Crystallogr.* **41,** 466–470 (2008).
31. Valenzano, L. *et al.* Disclosing the complex structure of UiO-66 metal organic framework: a synergic combination of experiment and theory. *Chem. Mater.* **23,** 1700–1718 (2011).

Acknowledgements

We thank the strategic research environment Diatech@UiO at the University of Oslo for funding. K.B.L. is also thankful to the co-supervisors of this project Elsa Lundanes, Carl Henrik Gørbitz and Steven Wilson for their ideas and comments, Leva Momtazi and Greig Shearer for help with FTIR measurements, David Wragg for proof reading and to other colleagues at the University of Oslo for their aid. We also like to thank the Norwegian national infrastructure for X-ray diffraction and scattering (RECX), and the Department of Geosciences at the University of Oslo for use of the X-ray fluorescence equipment.

Author contributions

The experiments were planned by both authors. All depositions, post deposition treatments and characterisations were performed by K.B.L. The manuscript was written by both authors.

Additional information

Supplementary Information accompanies this paper at http://www.nature.com/naturecommunications

Competing financial interests: The authors declare no competing financial interests.

How to cite this article: Lausund, K. B. & Nilsen, O. All-gas-phase synthesis of UiO-66 through modulated atomic layer deposition. *Nat. Commun.* **7,** 13578 doi: 10.1038/ncomms13578 (2016).

Supplementary figures

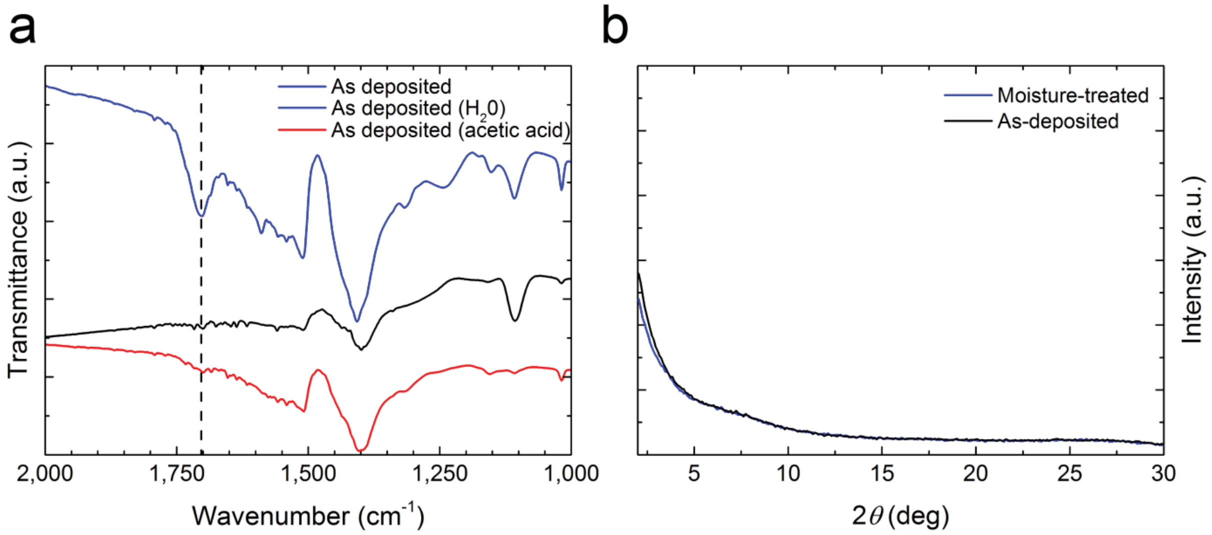

Supplementary Figure 1 | Characterisations of films deposited with H_2O pulsing. a, Fourier transform infrared (FTIR) spectra of the film deposited with H_2O pulses in addition to the two precursors $ZrCl_4$ and 1,4-benzene dicarboxylic acid (1,4-BDC) (black); and an unmodulated sample (blue) and an acetic acid modulated samples (red) for comparison. The peak that indicates a monodentate coordination of 1,4-BDC, which is seen in the unmodulated sample (dashed line), is removed when water or acetic acid is pulsed in addition to the two precursors. **b**, a GIXRD pattern for a film deposited with H_2O pulsing as deposited (black), and a GIXRD pattern for the same film after exposure to a relative humidity of 70-75 % for 24h (blue). No peaks corresponding to crystalline 1,4-BDC are seen on the sample that has been exposed to moisture, indicating that the excess 1,4-BDC is removed similar to the effect seen with acetic acid in Figure 5c.

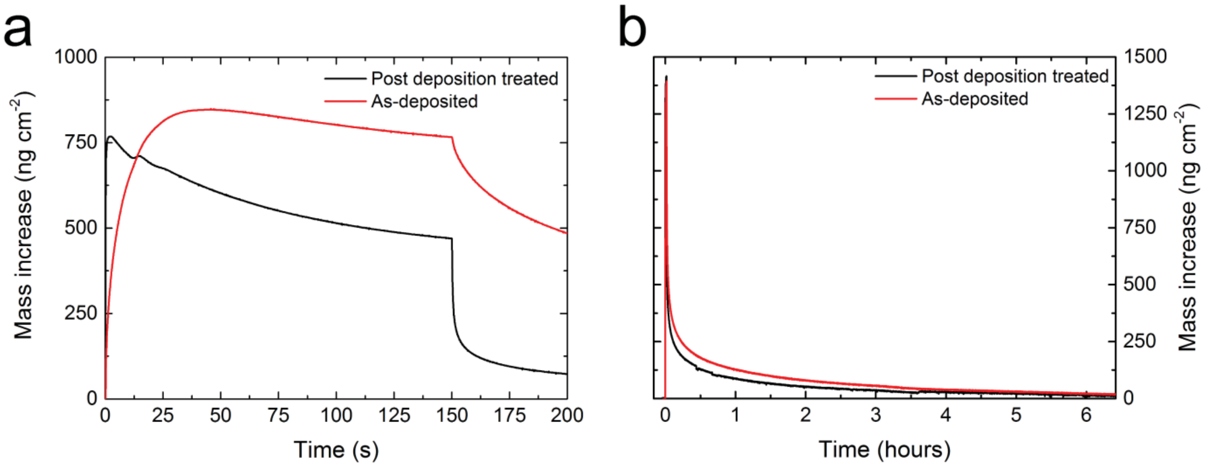

Supplementary Figure 2 | Saturated porosity test. a, porosity test performed by monitoring the water uptake by QCM-crystals during a 150 second water pulse. The test was performed in the ALD reactor at room temperature with a base pressure of 5 mbar N_2. Red is the as-deposited sample (ca. 230 nm) and black is the post deposition treated sample (ca. 500 nm). Both samples saturate with water. The kinetics of the saturation are not investigated further due to too many unknown factors, such as a drop in the partial pressure of water over time during the pulse and a likely difference in pore size in the two films. **b**, a similar porosity test performed with the same samples and a pulse length of 1 minute followed by a long purge. All of the adsorbed mass is lost during the purge. The relative humidity during this pulse was approximately 11% compared to approximately 7% for all the other porosity tests due to an increased water dosage during the pulse.

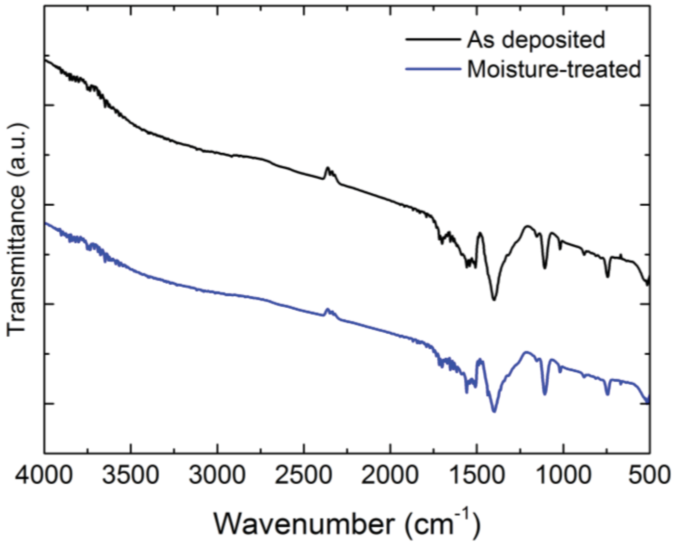

Supplementary Figure 3 | FTIR of moisture treated sample. FTIR spectra of a film deposited with acetic acid modulation, before (black) and after (blue) exposure to a relative humidity of 70-75 % for 24h. No changes occur in the FTIR spectrum upon exposure to moisture. These samples are similar to the ones used for the porosity tests.

Paper II

All-gas-phase synthesis of amino-functionalized UiO-66 thin films

II

K. B. Lausund, V. Petrovic and O. Nilsen,

Dalton Transactions, 2017, **46**, 16983-16992

II

Dalton Transactions

PAPER

View Article Online
View Journal | View Issue

Cite this: *Dalton Trans.*, 2017, **46**, 16983

All-gas-phase synthesis of amino-functionalized UiO-66 thin films†

Kristian Blindheim Lausund, *[a,b] Veljko Petrovic[a,b] and Ola Nilsen *[a,b]

Received 19th September 2017,
Accepted 25th October 2017

DOI: 10.1039/c7dt03518g

rsc.li/dalton

Thin films of metal–organic frameworks (MOFs) prepared using all-gas-phase techniques such as atomic/molecular layer deposition (ALD/MLD) are emerging due to their potential for enabling suitable applications. Their high and specific porosity enables their use as membranes for separations and as a basis for sensors in microelectronics, provided that films can be made. The properties of such MOF materials can be tuned by choosing linker molecules that are functionalized with a variety of chemical groups. However, thin films of these functionalised MOFs have so far been prepared through wet based chemistries, which are difficult to combine with microelectronics and high aspect ratio structures. We here report on the thin film deposition of amino-functionalised UiO-66 through an all-gas-phase ALD/MLD process. By using amino-functionalised linkers, modulation by acetic acid to control the stoichiometry of the deposited film was no longer required, as opposed to the case in which unmodified terephthalic acid was used as a linker. The growth and properties of the films were characterised using an *in situ* quartz crystal microbalance (QCM), spectroscopic ellipsometry (SE), grazing incidence X-ray diffraction (GIXRD), Fourier transform infrared spectroscopy (FTIR) and other techniques to obtain information on their growth dynamics and physical properties.

Introduction

Metal–organic frameworks (MOFs) are a class of materials that consists of inorganic metal-based clusters bound together by organic linker molecules. This creates a highly ordered porous framework with well-defined pore sizes with narrow distributions.[2] The porosity of these materials exceeds that of the well-known zeolites, making them attractive for several applications such as gas storage,[3] catalysis,[4] separations,[5] drug delivery,[6] handling and destruction of toxins,[7–9] and degradation of chemical warfare agents.[9,10] So far, the majority of these MOF materials have only been produced as powders through wet based techniques such as solvothermal synthesis. By enabling the deposition of such materials as thin films, crystalline or amorphous, numerous new areas of applications such as membrane filters and integrated sensors or low-κ dielectrics in microelectronics can be realised.[11]

The properties of MOFs can be tuned to serve different needs by functionalising the linker molecule itself. Among the properties that are demonstrated to be tunable are selectivity to certain gas molecules,[12,13] hydrophilicity,[14] and catalytic properties.[15] It is thus also of interest to investigate how the functionalisation of the linkers affects the growth of such materials. In this study we compare the growth of UiO-66 with amino-functionalised terephthalic acid (UiO-66-NH_2) with our prior reports on the deposition of UiO-66 using terephthalic acid.[1]

The atomic layer deposition (ALD) technique, also known as molecular layer deposition (MLD)[16–18] when larger molecules are included in the growth, such as here, enables the outmost control of the deposited material even when deposited on complex geometries. The film is made one atomic or molecular layer at a time through gas-to-surface reactions. The precursors are pulsed sequentially and separately into the reaction chamber where they react with and saturate the surfaces of the substrates. Inert gas purge steps separate the precursor pulses and avoid reactions in the gas phase. By repeating these steps for a given number of cycles, a thin film with the desired thickness is made. A more thorough description of the deposition technique is given in the reviews.[19–21]

By enabling the thin film deposition of functionalized MOFs through MLD, we can introduce the same tunability as noticed in traditionally synthesized MOFs for applications in which an all-gas-phase deposition technique is required, such as in microelectronics.

---

[a] *Department of Chemistry, University of Oslo, Postboks 1033, Blindern, 0315 OSLO, Norway. E-mail: ola.nilsen@kjemi.uio.no, k.b.lausund@kjemi.uio.no*
[b] *Centre for Materials Science and Nanotechnology, University of Oslo, Postboks 1033, Blindern, 0315 OSLO, Norway*

† Electronic supplementary information (ESI) available: Some additional results including TG data for the organic precursor (2-amino-1,4-BDC), GIXRD diffractograms for post-treated films that were deposited at 315 °C and a graph showing the full porosity test. See DOI: 10.1039/c7dt03518g

Another important factor that affects the applicability of MOF thin films is their stability. In the early days of MOF-research, the crystals were unstable when removed from the solution in which they were made. Numerous examples of stable MOF-compounds have now been demonstrated, and it is important to choose the appropriate one among these when designing for applications.[22] Our choice has been the thermally and chemically stable UiO-66 type as the basis for further explorations.[23]

There are only few examples in the literature of MOF thin films with functional groups on the linkers, and no examples where the films are made by all-gas phase processes such as MLD. These films are typically made by liquid phase epitaxial growth (LPE) on self-assembled monolayers (SAMs) on gold substrates. One example is the work performed by Shekhah *et al.*[24] who used LPE on a SAM functionalized gold surface to make a layer based MOF with the chemical formula [$Cu_2(NH_2$-bdc$)_2$(dabco)] where NH_2-bdc = 2-amino-1,4-benzene dicarboxylic acid (abbreviated in this work as 2-amino-1,4-BDC), and dabco = 1,4-diazabicyclo[2.2.2]octane. They also demonstrated the possibility of post-synthesis modification (PSM) by allowing the NH_2 groups to react with larger chemical groups such as 1-ferrocenylmethylisocyanate. Another example of functionalized MOF thin films made by this technique is the work by Wang *et al.*[25] where they made [$Zn_2(N_3$-bdc$)_2$(dabco)] (N_3-bdc = 2-azidoterephthalic acid) and demonstrated PSM by reactions with the azido group. An example of functionalized MOF films that are synthesized through a different approach is seen in the work by Yoo *et al.*[26] in which a film of IRMOF-3 (amino-functionalized) is grown by solvothermal synthesis on a surface seeded by IRMOF-1 (non-functionalized) crystals.

Our present films are made using $ZrCl_4$ and 2-amino-1,4-benzene dicarboxylic acid (2-amino-1,4-BDC, also known as 2-amino-terephthalic acid) and will be compared to our prior work on the deposition of UiO-66 using $ZrCl_4$ and 1,4-benzene dicarboxylic acid (1,4-BDC, also known as terephthalic acid).[1]

Experimental

Atomic/molecular layer deposition

The ALD/MLD depositions were performed in an F-120 Sat-type ALD reactor (ASM Microchemistry Ltd) using $ZrCl_4$ (MERCK Schuchardt OHG >98%) and 2-amino-1,4-benzene dicarboxylic acid (2-amino-1,4-BDC) (Sigma-Aldrich 99%) as precursors. Acetic acid (MERCK KGaA 100%) was also used as a co-reactant in selected experiments. The carrier and purging gas was N_2 (AGA 99.999%). A total flow of *ca.* 250 sccm (standard cubic centimetres per minute) of N_2 was used throughout the experiments, leading to a background pressure of *ca.* 5 mBar. The vaporization temperatures for $ZrCl_4$ and 2-amino-1,4-BDC were set to 165 and 225 °C, respectively, based on previous work[17] and TG results that were collected using a NETZSCH 209 F1 Libra with a Pt/Rh stage and a type S thermocouple with a dry aluminium crucible. Acetic acid was kept at room temperature in an external container. The films were deposited on as-received, pre-cleaned Si(001) substrates of 2×2 cm^2. Their native oxide thickness was measured by spectroscopic ellipsometry (SE) before deposition and taken into account when the film thickness was determined.

In situ quartz crystal microbalance (QCM)

In situ QCM analyses were conducted using two 6 MHz AT cut quartz crystals mounted *ca.* 5 cm apart on a home-made holder in order to monitor the mass increase during the deposition and uncover possible delayed saturations through the reaction chamber. The signals were recorded using a Maxtek TM-400 and processed by averaging over 16 consecutive cycles. The signal from the QCM analysis was converted from $-\Delta$ Hz to ng cm^{-2} by calibrating the sensitivity of each sensor with the thickness and density data obtained by XRR of films deposited separately from the QCM measurements. Variations in sensitivity of the sensors throughout the QCM experiment were also corrected for by using a standard sequence repeatedly throughout the experiment and adjusting all results based on variations in this standard. In order to ensure a reliable response from the QCM-crystals, the temperature was stabilised for 3 hours before any experiments were conducted. This setup was also used for a porosity test where the QCM detectors were used to measure the amount of water that was adsorbed in the porous films.

Post-deposition treatment

Some of the films were exposed to moisture for 24 h in a chamber that was held at a relative humidity of 70–75% by storing a saturated NaCl solution in the chamber to investigate the effect of moisture on the films. The crystallization of the films was performed by heating the samples to 160 °C for 24 h in a sealed autoclave with an internal volume of 35 ml. This was done with dry or moist air and with or without adding approximately 0.1 ml of acetic acid in the autoclave. Crystallization occurred only when acetic acid was added.

Characterisation of the films

The thickness and the refractive index of each film were measured using spectroscopic ellipsometry. SE data were collected using a J. A. Woollam alpha-SE spectroscopic ellipsometer employing a wavelength range of 390–900 nm, and modelled to a Cauchy-function using the CompleteEASE software package in order to determine the thicknesses and refractive indices (at λ = 632.8 nm) of the films. Grazing incidence X-ray diffraction (GIXRD) and X-ray reflectivity (XRR) analyses were performed using a PANalytical Empyrean diffractometer, equipped with a Cu Kα source powered at 45 kV/40 mA (λ = 1.5406 Å), a parallel beam X-ray mirror and a proportional point detector (PW 3011/20). For GIXRD the incident angle was ω = 0.30° while for XRR analysis 2θ was scanned from 0.08° to 6°. The XRR results were analysed using the X'Pert Reflectivity software provided by PANalytical. Fourier transform infrared (FTIR) spectroscopy was for the most part performed using a Bruker VERTEX 70 FTIR spectrometer in the transmission mode. An exemption was the as-deposited samples for which the spectra were collected using a Cary 630

FT-IR in the transmission mode. A spectrum obtained from an uncoated silicon substrate was used as the background. Scanning electron microscopy (SEM) images were obtained using a HITACHI SU8230 scanning electron microscope with a cold cathode field emission type electron gun. The working distance was approximately 2 mm, and the acceleration voltage was typically 1 kV with a beam current of 10 μA.

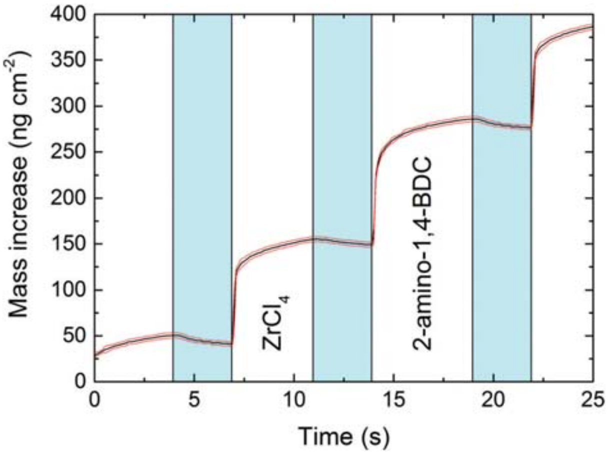

Fig. 1 Quartz crystal microbalance characterization. Mass gain as a function of time measured *in situ* in the molecular layer deposition (MLD) process with quartz crystal microbalance (QCM) while alternating between $ZrCl_4$ and 2-amino-terephthalic acid (2-amino-1,4-BDC) pulses separated by inert gas (N_2) purges (blue). The red lines show the standard deviations for the QCM data (*n* = 16).

Results

Thermogravimetric (TG) analysis was performed on the 2-amino-1,4-BDC precursor to aid in determining a suitable precursor temperature (ESI Fig. 1†). This, combined with the visual inspection of the precursor during heating, showed a suitable precursor temperature of *ca.* 225 °C. The deposition was investigated using an *in situ* quartz crystal microbalance (QCM) for deposition at a reactor temperature of 265 °C using a pulsing sequence of 4 s $ZrCl_4$, 3 s purge, 5 s 2-amino-1,4-BDC, and 3 s purge (hereafter termed 4-3-5-3), Fig. 1. Both precursors show self-limiting growth (Fig. 2).

The growth rate as a function of pulse and purge lengths was investigated by varying one parameter individually while keeping the others constant at 4-3-5-3, Fig. 2. This experiment was performed using two QCM detectors situated 5 cm apart along the flow direction in the deposition chamber, and the experiment was repeated two times for the investigation of the pulse lengths.

The reactions show a self-saturating behaviour with full saturation after 4 s for both precursors. It is possible to observe a delayed response in the QCM signal for the sensor situated in the back of the reaction chamber. This indicates that the

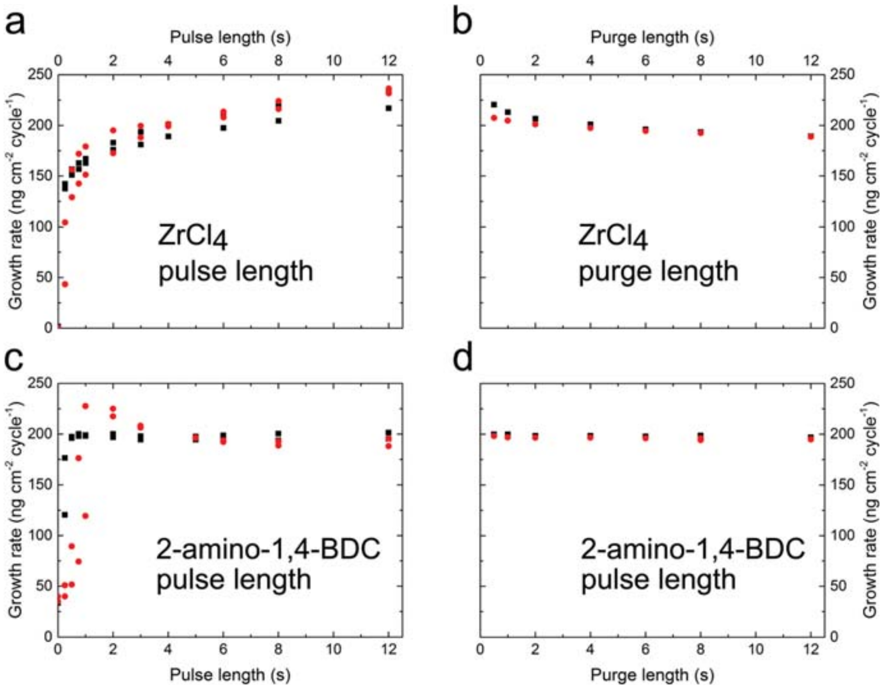

Fig. 2 Test of self-saturating growth. The growth rates for the ALD/MLD system measured using a QCM with a basic pulsing sequence of 4 s $ZrCl_4$, 3 s purge, 5 s 2-amino-1,4-BDC, and 3 s purge (termed in the text as 4-3-5-3) while the parameters were varied individually. The parameters that are varied are (a) the $ZrCl_4$ pulse length, (b) the $ZrCl_4$ purge length, (c) the 2-amino-1,4-BDC pulse length and (d) the 2-amino-1,4-BDC purge length. Two sensors were used, one in the front of the reaction chamber (black squares) and one in the back (red circles). The pulse length experiments were performed two times.

surface reactions are fast and complete so that almost no precursor reaches the back of the reaction chamber until the front of the chamber is fully saturated.

The dependency of the deposition temperature on the growth rate was investigated using 100 cycles as the standard, Fig. 3. The growth rate decreases with increasing deposition temperature from 10 Å per cycle at 240 °C to 7.5 Å per cycle at 390 °C while the refractive index increases slightly in the same range. For comparison, the index of refraction of ZrO_2 is 2.16.

Previously, we have shown that films deposited with 1,4-BDC (without amino-functionalization) in the same manner as above contained an excess of this linker molecule that would crystallize on the surface of the film when exposed to a relative humidity of 70–75% over 24 h. The origin of this excess amount of linker was the monodentate coordination of a selection of linkers with the Zr-atoms. A fully bidentate coordination could be achieved by adding a pulse of acetic acid in the deposition process. The acetic acid functioned as a modulator that released the monodentate 1,4-BDC leaving only the desired linkers with a bidentate coordination. However, when functionalized 2-amino-1,4-BDC is used, the steric hindrance from the amino group ensures that the linkers coordinate in the correct, bidentate manner without a need for further modulation, as illustrated in Fig. 4. This is also seen throughout our results, for instance, after exposure to humid air, we see no evidence of crystallisation of the excess linker from grazing incidence X-ray diffraction (GIXRD) analysis or the development of surface roughness, Fig. 5b. We also see from the QCM experiments that the acetic acid that is pulsed in addition to $ZrCl_4$ and 2-amino-1,4-BDC does not lead to any overall change in the mass during exposure and purge, nor does it alter the mass ratio between $ZrCl_4$ and 2-amino-1,4-BDC, Fig. 5a. Finally, the density of the films as determined by X-ray reflectivity (XRR) is unaffected by the added acetic acid pulse whereas the density increased when modulation was introduced in the system where regular 1,4-BDC was used.

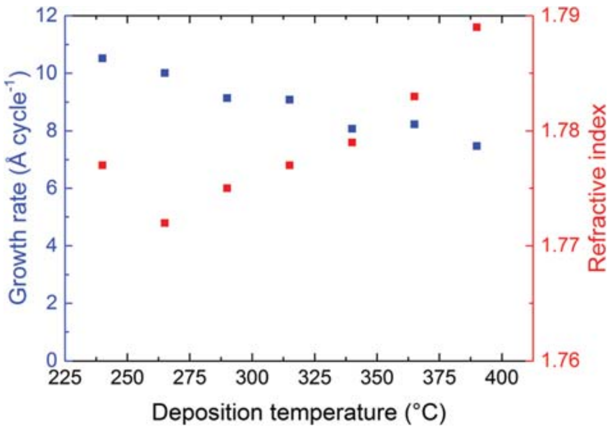

Fig. 3 Varying the deposition temperature. The growth rate of the ALD/MLD system and the refractive index of the films as a function of the deposition temperature.

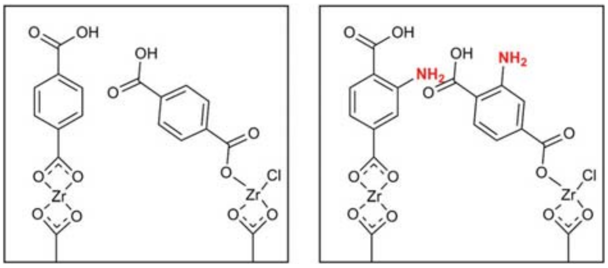

Fig. 4 Steric hindrance. An illustration of monodentate and bidentate coordination of un-functionalized 1,4-BDC (left) compared to the amino-functionalized 2-amino-1,4-BDC (right) that coordinates only in a bidentate due to steric hindrance.

All further samples were deposited without acetic acid modulation. The crystallization of the films was performed in the same manner as described in our previous work, by placing the coated substrates in a sealed autoclave along with approximately 0.1 ml of acetic acid and heating to 160 °C for 24 hours.

There is still a possibility that the moisture in ambient air can affect the crystallisation process. In order to better understand the importance of acetic acid compared to that of humid air in the crystallisation, we treated four samples deposited with 500 cycles at 265 °C in sealed autoclaves with and without acetic acid after exposing the samples to either dry or humid air. It is clear from the GIXRD diffractograms in Fig. 6 that crystallisation occurs only in the presence of acetic acid. The importance of the humidity in air is less clear as it is difficult to completely prevent exposure to humidity when acetic acid is also used. The effect of humidity is therefore not conclusive. The same test was done for four samples deposited with 500 cycles at 315 °C. This resulted in no crystallinity in any of the samples, indicating that a very high deposition temperature prevents crystallization into any MOF structure (ESI Fig. 2†). FTIR analysis (not shown) of these films shows significant changes in the peaks corresponding to the amino group in 2-amino-1,4-BDC. These changes may indicate partial decomposition or polymerisation of the linkers under these deposition conditions.

The crystallisation of the films resulted in numerous crystallites forming on the surface, as can be seen in the scanning electron microscope (SEM) images in Fig. 7. Some of these crystallites are hexagonally shaped, which does not cohere with the regular cubic crystal structure for UiO-66. We therefore assume that the present film rather crystallises in a layered type of UiO-66 similar to the one described by Cliffe *et al.*[27] The hexagonal shape of the crystallites is even more pronounced in the SEM images in Fig. 8.

Fourier transform infrared (FTIR) spectroscopy was used to determine the coordination of the carboxylate group with the Zr atoms as well as to confirm that the amino group is present in the final product. The amount of splitting between the peaks corresponding to the symmetric and asymmetric stretch of the carboxylate group indicates the coordination to the metal atoms. A bidentate coordination has a splitting of 50–150 cm^{-1}, which is seen for the amorphous samples that were autoclave

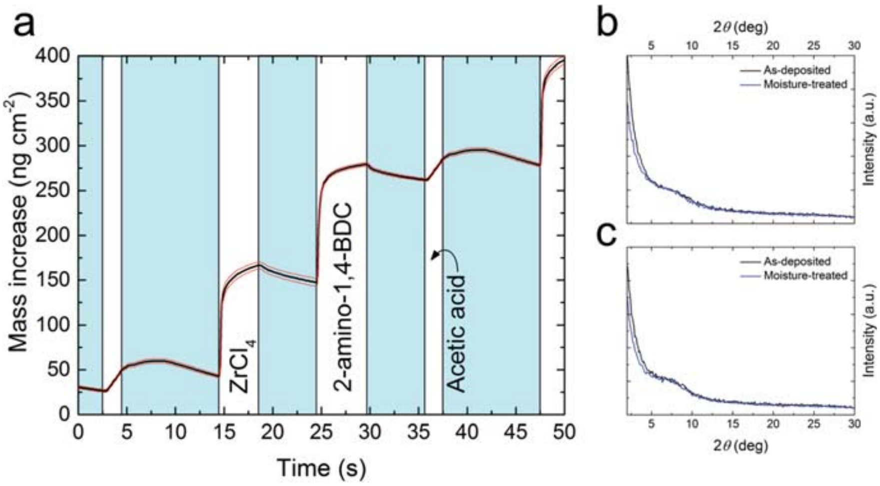

Fig. 5 Effects of acetic acid modulation on the ALD process. (a) QCM measurements of an ALD/MLD process in which a modulation step with acetic acid is included. The blue panels indicate the purge steps. The red lines show the standard deviation (n = 16). (b) and (c) Grazing incidence X-ray diffraction (GIXRD) diffractograms of samples deposited without and with acetic acid modulation, respectively, before (black) and after (blue) exposure to moist air (70–75% relative humidity for 24 h).

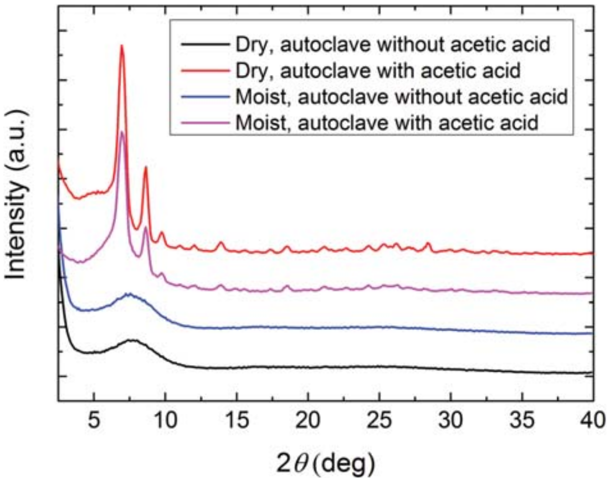

Fig. 6 Post-deposition autoclave treatment. GIXRD diffractograms for four samples that were treated in an autoclave with (magenta, red) or without (black, blue) acetic acid after being exposed to dry (black, red) or moist (blue, magenta) air after the deposition.

treated without acetic acid. A bridging coordination gives a splitting of 130–200 cm^{-1}. This is seen for the crystalline samples that were autoclave treated with acetic acid. A monodentate coordination would give a larger splitting than 200 cm^{-1}. This is not seen in any of the autoclave treated samples (Fig. 9a) or in the as-deposited samples with or without acetic acid modulation (Fig. 9b), again, indicating that the steric hindrance from the amino group prevents an excess amount of 2-amino-1,4-BDC to form a monodentate coordination with Zr.

In all of these spectra we see a peak at approximately 1260 cm^{-1} corresponding to the C–N stretch of the amino group, and a set of twin peaks between 3350 and 3500 cm^{-1} corresponding to the N–H stretches of the amino group. In the crystalline films that have been autoclave treated with acetic acid the peaks corresponding to the N–H-stretch are partly concealed by a broad water-peak, indicating that a lot of water is adsorbed in the pores of these films. Fig. 9c shows a cut-out of the N–H stretch.

In order to determine the porous nature of the films, a porosity test was performed in the same manner as in our prior work for UiO-66,[1] Fig. 10. This was performed by measuring the water uptake during a water pulse in the ALD-reactor at room temperature on two coated QCM crystals where one film was crystallized and the other was left amorphous. The pulse lengths that were used were first 5 seconds and then 2 minutes of exposure, followed by long purge steps where most (but not all) of the water was removed. After the five-second pulse, the film was not fully saturated with water unlike the un-functionalized UiO-66 film. The remaining water after the first pulse and purge was removed by heating to 150 °C for approximately 2 hours followed by a 24-hour-long temperature stabilization, leaving the water content slightly lower than the initial value, indicating that there was a small amount of water in the structure before the five-second pulse. The full experiment is shown in ESI Fig. 3.† This indicates that water adsorbs more strongly to these films than to the regular UiO-66 films without amino-functionalization. We also see that it takes a longer time for these films to be fully saturated with water than that for the films with non-functionalized 1,4-BDC. This could be due to a combination of increased adsorption to the amino group and reduction in the pore size where the amino–water complex slows down the diffusion of subsequent water molecules entering the film. Both the amorphous and the crystalline films are porous and have a much larger water uptake than the uncoated crystals (inset in Fig. 10), and the crystallisation process almost doubles the porosity.

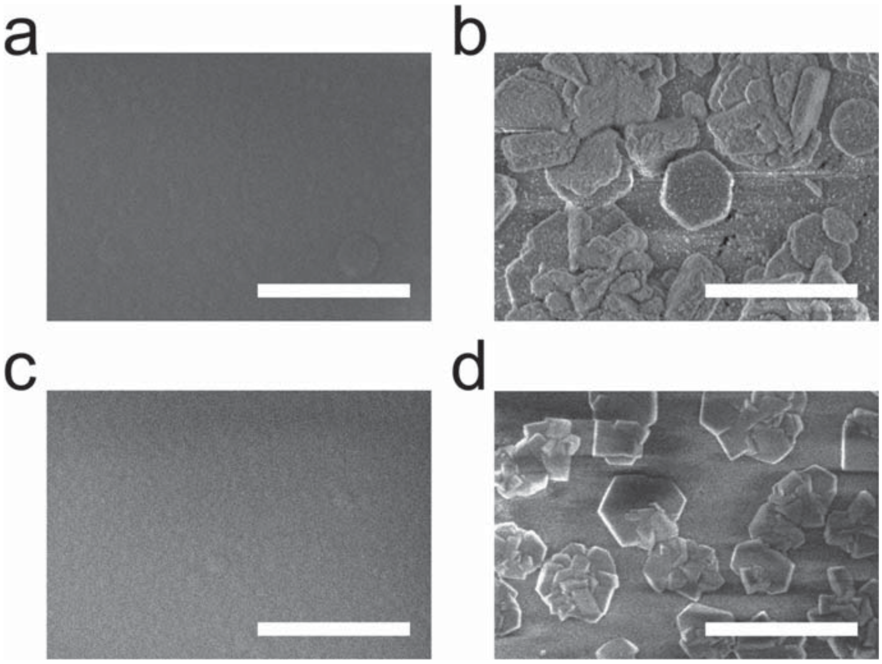

Fig. 7 Scanning electron microscopy. SEM images of four samples that were exposed to either dry or moist air and were treated in an autoclave after deposition: (a) exposed to dry air and autoclave treated without acetic acid, (b) exposed to dry air and autoclave treated with acetic acid, (c) exposed to moist air and autoclave treated without acetic acid, and (d) exposed to moist air and autoclave treated with acetic acid. All the scale bars are 1 μm long.

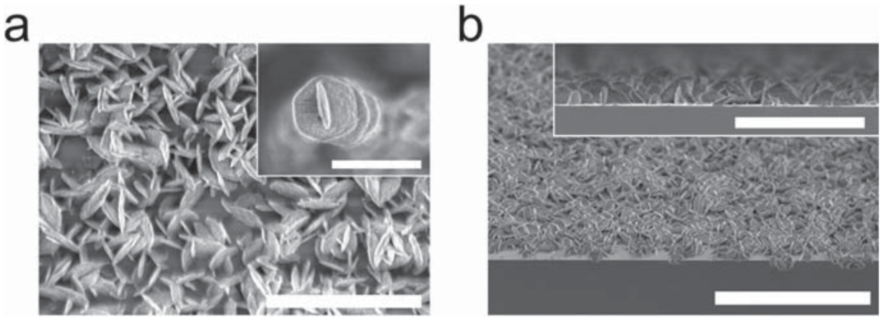

Fig. 8 Scanning electron microscopy. SEM images of a sample that was deposited with 100 cycles and crystallized in an autoclave with acetic acid and ambient air. (a) A top down view with an enlarged image of a hexagonal crystallite in the inset; the scale bars are 2 and 1 μm respectively. (b) A cross section view at a 45° angle with a cross section view at a 90° angle in the inset; the scale bars are 5 and 2 μm respectively.

The amino-functionalization of the linker alters some of the properties of the film. The hydrophilicity is increased as compared to that of un-functionalised UiO-66 films, as measured by its contact angle towards water, Fig. 11. Both of the films are in the amorphous as-deposited state.

Discussion

The MLD system in which $ZrCl_4$ and 2-amino-1,4-BDC were used as precursors shows self-terminating growth of each precursor, as measured by *in situ* QCM (Fig. 1, 2 and 5a). The growth rate is close to 1 nm per cycle for depositions at 265 °C, which is higher than that observed in the un-functionalized UiO-66 films.[1] This is notably higher than those with regular ALD processes, but within reach of many MLD systems (Fig. 3). One possible reason for the high growth rate is that the carboxylate groups in this case always coordinate in a bidentate manner causing the 2-amino-1,4-BDC molecules to be aligned normal to the substrate instead of being at an angle similar to that of the carboxylate groups with a monodentate coordination.

The growth rate decreases with increasing deposition temperatures indicating that the precursors desorb from the surface at higher temperatures, or cause disordered growth due to

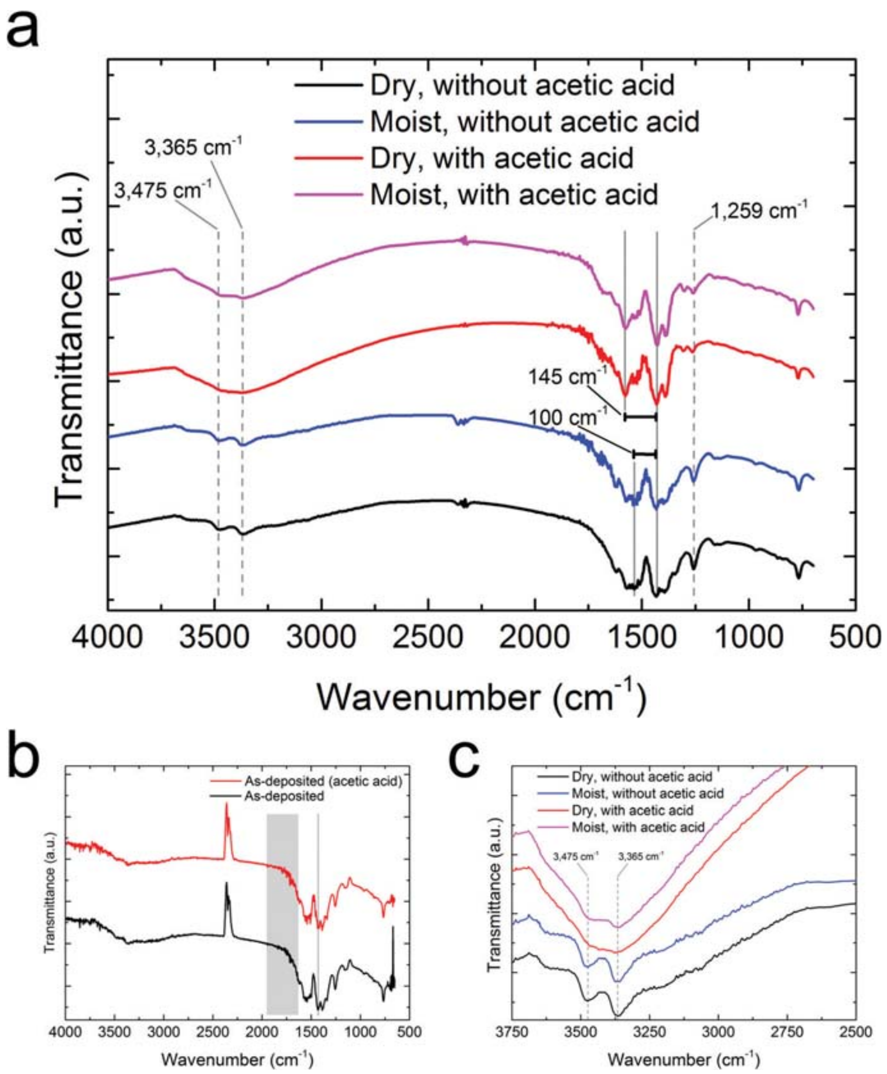

Fig. 9 Fourier transform infrared spectroscopy. (a) The full FTIR spectra for four samples that were treated in an autoclave with (magenta, red) or without (black, blue) acetic acid after being exposed to dry (black, red) or moist (blue, magenta) air after the deposition. (b) The FTIR spectra for two as-deposited samples that were deposited with (red) or without (black) acetic acid modulation. The grey box marks the area with a larger splitting than 200 cm^{-1} from the main peak (grey line), which is where a peak corresponding to monodentate coordination would be. (c) An enlarged view of the N–H stretch peaks from the amino group and the O–H stretch peaks from water for the same samples as in (a). Solid lines indicate carboxylate group peaks and dashed lines indicate amino group peaks.

increased entropy. In addition to this, it is probable that the organic precursor decomposes and/or polymerizes at high temperatures, which prevents the crystallization of films deposited at a very high temperature.

A comparison of the QCM results of Fig. 1 and 5a shows that the mass responses for the $ZrCl_4$ and 2-amino-1,4-BDC are virtually unaffected by the acetic acid pulse, with respect to both relative responses ($\Delta m(ZrCl_4\ \text{pulse}):\Delta m(\text{2-amino-1,4-BDC}) = 0.85$) and their absolute values in ng cm^{-2}.

As with the growth of the unmodified UiO-66 material, it is possible to postulate two overall reaction mechanisms, leading to a Zr : 2-amino-1,4-BDC stoichiometry of 1 : 2 or 1 : 1, where the latter is expected for the UiO-66 structure type.

1 : 2 stoichiometry:

$ZrCl_4$ pulse:

$$|{-}(OH)_x + ZrCl_4(g) = |{-}(O)_xZrCl_{(4-x)} + x\text{HCl}$$

2-Amino-1,4-BDC pulse:

$$\begin{aligned} &|{-}(O)_xZrCl_{(4-x)} + 2 \times \text{2-amino-1,4-BDC(g)} \\ &\quad = |{-}(O)_xZr(\text{2-amino-1,4-BDC})_2 + (4-x)\text{HCl} \end{aligned}$$

where $x = 0.75$ results in the observed relative mass increase of ($\Delta m(ZrCl_4\ \text{pulse}):\Delta m(\text{2-amino-1,4-BDC}) = 0.85$. This is somewhat lower than that practically possible, since it assumes that

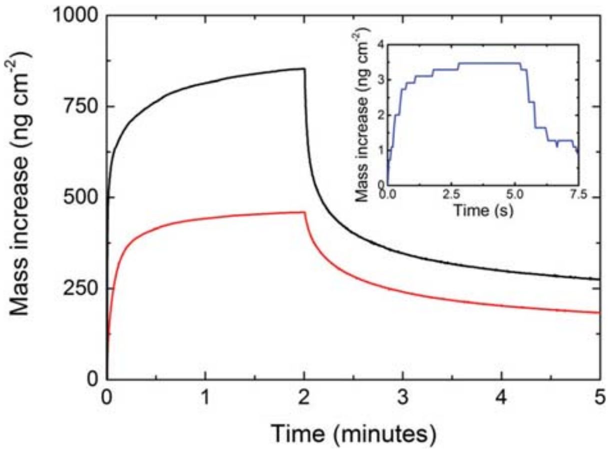

Fig. 10 Porosity test. The water uptake in an as-deposited, amorphous film (black) and a post-deposition treated, crystalline film (red) as a function of time for a 2 minute long water pulse in the ALD reactor at room temperature, as measured by QCM. The inset shows the water uptake on an uncoated QCM-crystal during a 5 second water pulse as a control.

25% of the $ZrCl_4$ molecules are physisorbed rather than chemisorbed so that HCl is not lost from the surface.

1 : 1 stoichiometry:

$ZrCl_4$ pulse:

$$|\text{–}(\mathrm{OH})_x + \mathrm{ZrCl_4(g)} = |\text{–}(\mathrm{O})_x\mathrm{ZrCl}_{(4-x)} + x\mathrm{HCl}$$

2-Amino-1,4-BDC pulse:

$$\begin{aligned} &|\text{–}(\mathrm{O})_x\mathrm{ZrCl}_{(4-x)} + \text{2-amino-1, 4-BDC(g)} \\ &\quad = |-(\mathrm{O})_x\mathrm{Zr}(\text{2-amino-1, 4-BDC}) + (4-x)\mathrm{HCl} \end{aligned}$$

where x = 3.0 results in the observed relative mass increase of (Δm($ZrCl_4$ pulse) : Δm(2-amino-1,4-BDC) = 0.85. This is within the expected range of x = 1–3 for reactions with $ZrCl_4$ as a precursor, and indicate that $ZrCl_4$ is highly reactive during the growth.

In our previous work,[1] an acetic acid modulation was required in order to achieve the correct stoichiometry between the metal atoms (Zr) and the organic linkers (1,4-BDC). This is not necessary when 2-amino-1,4-BDC is used as the linker, as can be seen from several of our results. First, there is no excess of the linker molecules crystallizing on the surface of films that have been exposed to moisture, causing the GIXRD diffractograms for films deposited with and without acetic acid modulation to be more or less identical (Fig. 5b and c). The QCM results also show that the overall reaction scheme is virtually unaffected by acetic acid. This also applies to the density as measured by XRR and FTIR analyses. From the FTIR analysis there is also no sign of monodentate coordination of the carboxylate group with the Zr atoms, which is the coordination mode of the excess linkers in our previous work mentioned above.

One possible explanation for modulation not being required for the amino-functionalized linker is that the steric hindrance of the amino group in a bidentate linker prevents its neighbours to coordinate in an angled monodentate manner, causing all linkers to form a bidentate coordination (Fig. 4).

From the GIXRD diffractograms in Fig. 5b and c (and the FTIR spectra in Fig. 9b) it is clear that the as-deposited films are amorphous both with and without acetic acid modulation. The films can, however, be crystallised through heating in a sealed autoclave with a small amount of acetic acid as seen from the GIXRD diffractograms in Fig. 6 (and the FTIR spectra in Fig. 9a).

In summary, we were able to prepare a crystalline, amino-functionalized MOF thin film through MLD. This amino-functionalization alters the properties of the film such as the heat of adsorption of water in the pores and can make it suitable for different applications than the un-functionalized MOF. The fact that thin films of this functionalized MOF can be made through ALD may enable it to be used in microelectronics such as sensors where normal solvothermal synthesis cannot be used due to the stiction of small components. The amino group also facilitates a more simple deposition process in that the acetic acid modulation is no longer required.

Conclusion

Thin films of crystalline, amino-functionalized UiO-66 (UiO-66-NH_2) were made by depositing a thin film by MLD, using 2-amino-1,4-BDC and $ZrCl_4$ as precursors, followed by post-deposition crystallisation. The amino-functionalization proved to be an advantage in the deposition process by eliminating the need for an acetic acid modulation step. The films

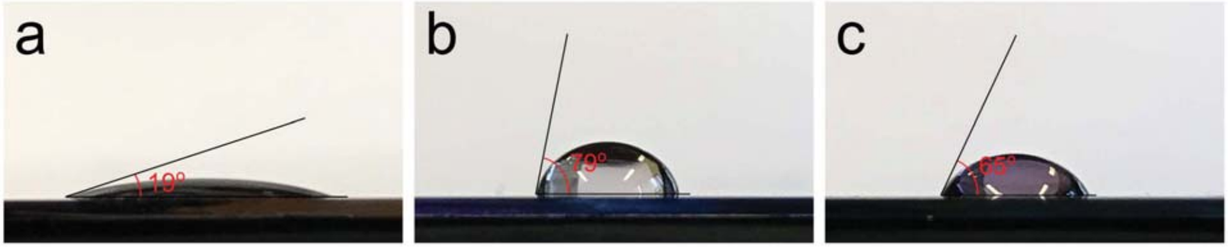

Fig. 11 Contact angle measurements. The contact angle of water on (a) a clean substrate, (b) an as-deposited, amorphous UiO-66 film (not amino-functionalized), and (c) an as-deposited, amorphous, amino-functionalized UiO-66-NH_2 film.

were characterized before and after crystallization using GIXRD, FTIR and SEM, all of which indicate that the crystallization was successful. Contact angle measurements and porosity measurements were also conducted, and they show that UiO-66-NH_2 has some different properties compared with the un-functionalized UiO-66 such as a more hydrophilic character.

Conflicts of interest

There are no conflicts to declare.

Acknowledgements

We thank the strategic research initiative Diatech@UiO at the University of Oslo for funding. K. B. L. is also thankful to the co-supervisors of this project Elsa Lundanes, Carl Henrik Gørbitz and Steven Wilson for their ideas and comments; Sigurd Øien-Ødegaard and Fredrik Lundvall for discussions regarding crystal structures; Leva Momtazi for FTIR measurements and discussions; Asbjørn Slagtern Fjellvåg for TG measurements; and to other colleagues at the University of Oslo for their aid. We also like to thank the Norwegian national infrastructure for X-ray diffraction and scattering (RECX), and the Department of Geosciences at the University of Oslo for use of the X-ray fluorescence equipment.

References

1 K. B. Lausund and O. Nilsen, All-gas-phase synthesis of UiO-66 through modulated atomic layer deposition, *Nat. Commun.*, 2016, **7**, 13578.

2 H. Li, M. Eddaoudi, M. O'Keeffe and O. M. Yaghi, Design and synthesis of an exceptionally stable and highly porous metal-organic framework, *Nature*, 1999, **402**(6759), 276–279.

3 H. R. Abid, H. Tian, H.-M. Ang, M. O. Tade, C. E. Buckley and S. Wang, Nanosize Zr-metal organic framework (UiO-66) for hydrogen and carbon dioxide storage, *Chem. Eng. J.*, 2012, **187**, 415–420.

4 J. Lee, O. K. Farha, J. Roberts, K. A. Scheidt, S. T. Nguyen and J. T. Hupp, Metal-organic framework materials as catalysts, *Chem. Soc. Rev.*, 2009, **38**(5), 1450–1459.

5 X. Liu, N. Keser Demir, Z. Wu and K. Li, Highly Water Stable Zirconium Metal-Organic Framework UiO-66 Membranes Supported on Alumina Hollow Fibers for Desalination, *J. Am. Chem. Soc.*, 2015, **137**(22), 6999–7002.

6 K. M. L. Taylor-Pashow, J. D. Rocca, Z. Xie, S. Tran and W. Lin, Postsynthetic Modifications of Iron-Carboxylate Nanoscale Metal–Organic Frameworks for Imaging and Drug Delivery, *J. Am. Chem. Soc.*, 2009, **131**(40), 14261–14263.

7 S. Jakobsen, D. Gianolio, D. S. Wragg, M. H. Nilsen, H. Emerich, S. Bordiga, C. Lamberti, U. Olsbye, M. Tilset and K. P. Lillerud, Structural determination of a highly stable metal-organic framework with possible application to interim radioactive waste scavenging: Hf-UiO-66, *Phys. Rev. B: Condens. Matter*, 2012, **86**(12), 125429.

8 C. Wang, X. Liu, J. P. Chen and K. Li, Superior removal of arsenic from water with zirconium metal-organic framework UiO-66, *Sci. Rep.*, 2015, **5**, 16613.

9 J. E. Mondloch, M. J. Katz, W. C. Isley Iii, P. Ghosh, P. Liao, W. Bury, G. W. Wagner, M. G. Hall, J. B. DeCoste, G. W. Peterson, R. Q. Snurr, C. J. Cramer, J. T. Hupp and O. K. Farha, Destruction of chemical warfare agents using metal–organic frameworks, *Nat. Mater.*, 2015, **14**(5), 512–516.

10 D. T. Lee, J. Zhao, G. W. Peterson and G. N. Parsons, Catalytic "MOF-Cloth" Formed via Directed Supramolecular Assembly of UiO-66-NH2 Crystals on Atomic Layer Deposition-Coated Textiles for Rapid Degradation of Chemical Warfare Agent Simulants, *Chem. Mater.*, 2017, **29**(11), 4894–4903.

11 M. D. Allendorf, A. Schwartzberg, V. Stavila and A. A. Talin, A Roadmap to Implementing Metal–Organic Frameworks in Electronic Devices: Challenges and Critical Directions, *Chem. – Eur. J.*, 2011, **17**(41), 11372–11388.

12 P. Serra-Crespo, E. V. Ramos-Fernandez, J. Gascon and F. Kapteijn, Synthesis and Characterization of an Amino Functionalized MIL-101(Al): Separation and Catalytic Properties, *Chem. Mater.*, 2011, **23**(10), 2565–2572.

13 G. E. Cmarik, M. Kim, S. M. Cohen and K. S. Walton, Tuning the Adsorption Properties of UiO-66 via Ligand Functionalization, *Langmuir*, 2012, **28**(44), 15606–15613.

14 S.-N. Kim, J. Kim, H.-Y. Kim, H.-Y. Cho and W.-S. Ahn, Adsorption/catalytic properties of MIL-125 and NH2-MIL-125, *Catal. Today*, 2013, **204**, 85–93.

15 W. Kleist, M. Maciejewski and A. Baiker, MOF-5 based mixed-linker metal–organic frameworks: Synthesis, thermal stability and catalytic application, *Thermochim. Acta*, 2010, **499**(1), 71–78.

16 O. Nilsen, K. Klepper, H. Nielsen and H. Fjellvaåg, Deposition of organic-inorganic hybrid materials by atomic layer deposition, *ECS Trans.*, 2008, **16**(4), 3–14.

17 K. B. Klepper, O. Nilsen and H. Fjellvag, Deposition of thin films of organic-inorganic hybrid materials based on aromatic carboxylic acids by atomic layer deposition, *Dalton Trans.*, 2010, **39**(48), 11628–11635.

18 P. Sundberg and M. Karppinen, Organic and inorganic–organic thin film structures by molecular layer deposition: A review, *Beilstein J. Nanotechnol.*, 2014, **5**(1), 1104–1136.

19 V. Miikkulainen, M. Leskelä, M. Ritala and R. L. Puurunen, Crystallinity of inorganic films grown by atomic layer deposition: Overview and general trends, *J. Appl. Phys.*, 2013, **113**(2), 021301.

20 M. Leskelä, M. Ritala and O. Nilsen, Novel materials by atomic layer deposition and molecular layer deposition, *MRS Bull.*, 2011, **36**(11), 877–884.

21 X. Meng, An Overview of Molecular Layer Deposition for Organic and Organic-Inorganic Hybrid Materials: Mechanisms, Growth Characteristics, and Promising Applications, *J. Mater. Chem. A*, 2017, 18326–18378.

22 K. Leus, T. Bogaerts, J. De Decker, H. Depauw, K. Hendrickx, H. Vrielinck, V. Van Speybroeck and P. Van Der Voort, Systematic study of the chemical and hydrothermal stability of selected "stable" Metal Organic Frameworks, *Microporous Mesoporous Mater.*, 2016, **226**, 110–116.

23 J. H. Cavka, S. Jakobsen, U. Olsbye, N. Guillou, C. Lamberti, S. Bordiga and K. P. Lillerud, A new zirconium inorganic building brick forming metal organic frameworks with exceptional stability, *J. Am. Chem. Soc.*, 2008, **130**(42), 13850–13851.

24 O. Shekhah, H. K. Arslan, K. Chen, M. Schmittel, R. Maul, W. Wenzel and C. Wöll, Post-synthetic modification of epitaxially grown, highly oriented functionalized MOF thin films, *Chem. Commun.*, 2011, **47**(40), 11210–11212.

25 Z. Wang, J. Liu, H. K. Arslan, S. Grosjean, T. Hagendorn, H. Gliemann, S. Bräse and C. Wöll, Post-synthetic modification of metal–organic framework thin films using click chemistry: the importance of strained C–C triple bonds, *Langmuir*, 2013, **29**(51), 15958–15964.

26 Y. Yoo and H.-K. Jeong, Heteroepitaxial Growth of Isoreticular Metal– Organic Frameworks and Their Hybrid Films, *Cryst. Growth Des.*, 2010, **10**(3), 1283–1288.

27 M. J. Cliffe, E. Castillo-Martínez, Y. Wu, J. Lee, A. C. Forse, F. C. N. Firth, P. Z. Moghadam, D. Fairen-Jimenez, M. W. Gaultois, J. A. Hill, O. V. Magdysyuk, B. Slater, A. L. Goodwin and C. P. Grey, Metal–Organic Nanosheets Formed via Defect-Mediated Transformation of a Hafnium Metal–Organic Framework, *J. Am. Chem. Soc.*, 2017, **139**(15), 5397–5404.

Electronic Supplementary Material (ESI) for Dalton Transactions.

Supplementary information

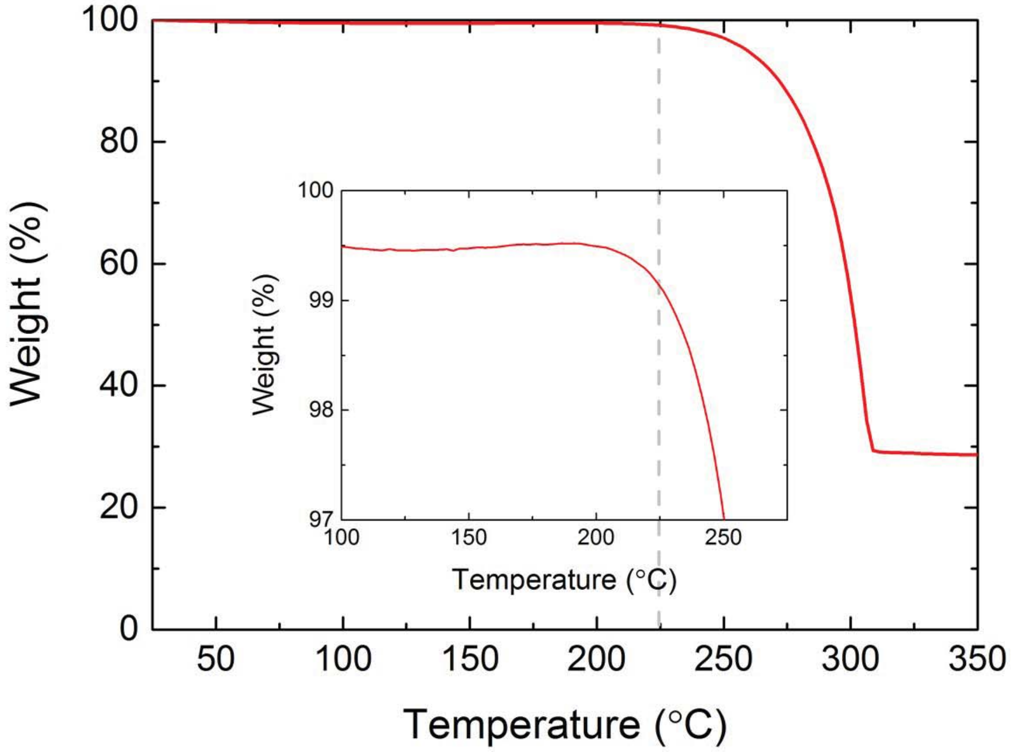

Supplementary figure 1 | Thermogravimetric analysis. Weight loss as a function of the sample temperature for 2-amino-1,4-BDC with a hating rate of 1 °C per minute. The inset shows a portion of the same graph expanded along the y-axis. The dashed grey line shows the chosen precursor temperature (225 °C).

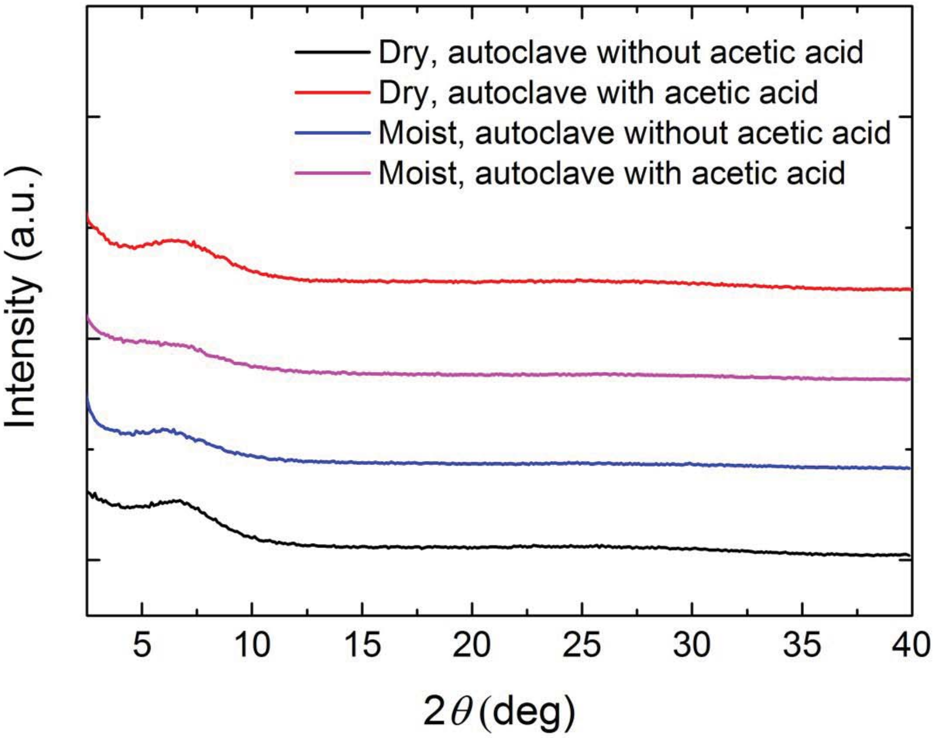

Supplementary figure 2 | Samples deposited at 315 °C. GIXRD diffractograms of four samples that were deposited with a reaction temperature of 315 °C that have been treated in an autoclave with (magenta, red) or without (black, blue) acetic acid after being exposed to dry (black, red) or moist (blue, magenta) air after the deposition.

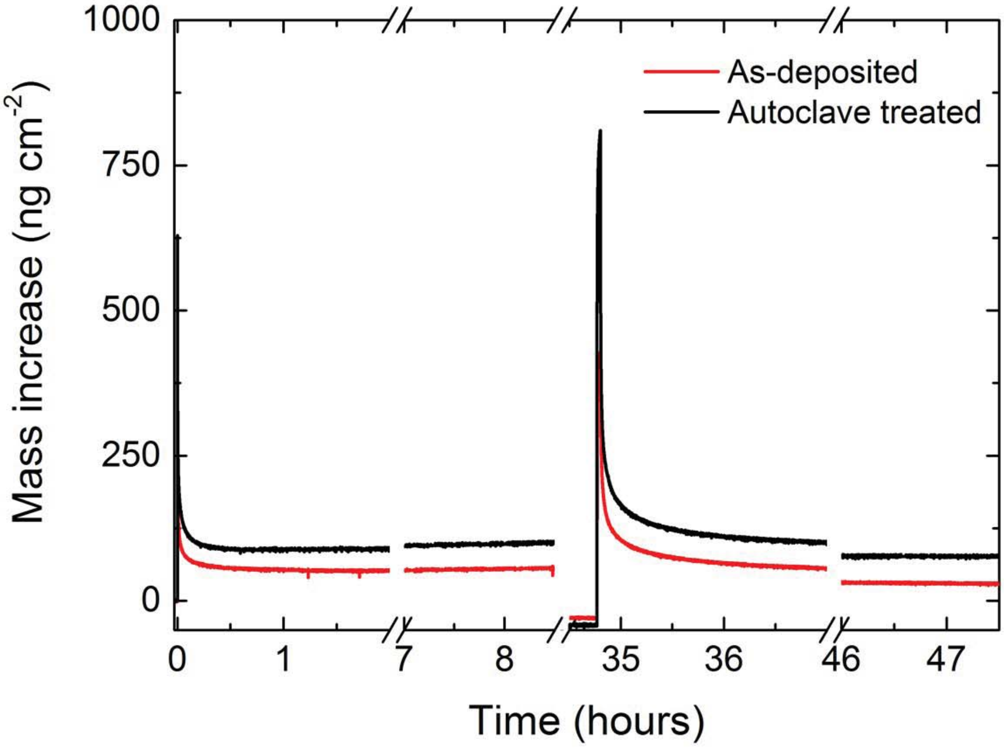

Supplementary figure 3 | Porosity test. A graph showing the mass increase and loss over time for the full porosity test of an As-deposited (black) and autoclave treated (red) sample. The experiment consists of a five-second water pulse followed by a nine-hour purge, a heating step (2 hours at 150 °C and 24-hour temperature stabilization, not shown), and a two-minute water pulse followed by a 12-hour purge.